MEG Source Imaging and Dynamic Characterization.

Sheraz Khan

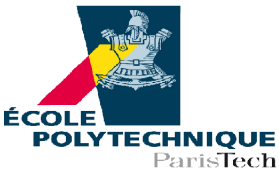

THÈSE

Présentée pour obtenir
LE GRADE DE DOCTEUR EN SCIENCES
DE L'ÉCOLE POLYTECHNIQUE
Spécialité : Mathématiques Appliquées

par

Sheraz KHAN

MEG Source Imaging and Dynamic Characterization

Soutenue le 15 janvier 2010 devant la commission d'examen formée de :

Jury :

Habib AMMARI	-	Ecole Polytechnique
Sylvain BAILLET	-	Medical College of Wisconsin
Ali Mohammad DJAFARI	-	Laboratoire des Signaux & Systèmes (SUPÉLEC)
Josselin GARNIER	-	Université de Paris 7
Francois JOUVE	-	Université de Paris 7
Roman NOVIKOV	-	Ecole Polytechnique
Gabriel PEYRE	-	Université de Paris 9
Julien LEFÉVRE	-	Université de la Méditerranée

Acknowledgements

As I look through the last three years, there are so many people without the help of them this thesis might never be possible, first and foremost my PhD directors Sylvain Baillet and Habib Ammari, whose continuous guidance and support make this thesis realizable. Julien Lefevre for his excellent mentorship during the second and third years of PhD, without him HHD part of the thesis would not have been possible.

My colleagues at Paris and Milwaukee, Manoj, Rey, Benoit, Guillaume, Sophie, Beth and many others, there constant help and motivation, make this thesis through, they are always with me when things are not working and cheer me when things work out.

Lastly I acknowledge my parents, my wife and my daughter, for their continuous support and help, their prayers made this only possible.

Summary

My thesis has addressed two complementary aspects of magnetic source imaging using Magnetoencephalography:

1. Imaging of neural current sources from MEG surface recordings;
2. Dynamic characterization of neural current patterns at the surface of the cortex.

MEG Source Imaging

Accurate estimation of the local spatial extent of neural current activity is very important for the quantitative analysis of neural current sources, as estimated from Magnetoencephalography (MEG) surface recordings. In association with the excellent time resolution offered by MEG, this would represent a major advancement in non invasive, time-resolved functional brain imaging.

We addressed this issue through a new method – called Multipole Cortical Remapping (MCR) – to accurately specify the spatial extent of neural current sources.

In MCR, the zeroth-order Tikhonov regularized image of the current distribution on the cortex is first estimated from MEG surface data for which we sought for a realistic model of neural generators. Then the resulting functional image is thresholded using a simple histogram-based principle. This thresholded image is then decomposed into groups of activation patterns following an automatic labeling algorithm based on the geometrical properties of the cortical surface. The

equivalent multipolar decomposition of each current patch is then obtained. By default, the multipolar moments are not readily related to the actual anatomical support of the actual neural currents detected using MEG. Hence we introduced an image remapping techniques of the multipolar parameters back onto the original cortical manifold, in a Bayesian framework including physiological and anatomical priors.

Characterization of MEG Source Dynamics

For dynamic characterization of neural current patterns at the surface of the cortex, we used a modified Helmholtz-Hodge Decomposition (HHD), which was applied on vector fields describing the flow of neural current sources. This motion field stems from a generalized approach to optical flow estimation, developed earlier in our team.

Optical flow is the apparent motion due to variations in the pattern of brightness and, under specific conditions, may mimic the velocity field of an object. Normally, the optical flow is obtained in a two-dimensional domain, which may prevent access to some essential features of the object's motion with respect to the topology or geometry of the domain onto which it is evolving. A new variational method to represent optical flow on non flat surfaces using Riemannian formulation was previously introduced by our group to overcome this issue.

We broadened this framework and introduced a new formalism to detect features in the resulting optical flow model using a modified and extended framework to the HHD on 2-Riemannian manifolds, which we used to characterize neural current sources.

HHD is a technique used to decompose a two-dimensional (resp. three-dimensional) continuous vector field into the sum of 3 distinct components: (1) a non-rotational element, deriving from the gradient of a scalar potential U; (2) a non-diverging component, deriving from the rotational of a scalar potential A (resp. vectorial potential); (3) a harmonic vectorial part, *i.e.*, whose Laplacian

vanishes.

We showed how HHD enables the decomposition and tracking of time-resolved neural current flows as obtained from MEG source imaging as sources and sinks e.g., by detecting relative maxima of the non-rotational scalar potential. We henceforth suggest to extend the analysis of brain activity in terms of tracking travelling objects onto the cortical manifold by detecting vectors of largest amplitudes in zero Laplacian harmonic vector fields.

We also considered HHD through a series of structural and functional brain imaging applications, with very encouraging preliminary results.

The methods discussed in the HHD section of the thesis were implemented in MATLAB as plug-in to the Brainstorm (MEG/EEG data processing software) and can be downloaded from: **http://neuroimage.usc.edu/brainstorm**. A short tutorial for this plug-in is presented in Appendix 3.

Contents

List of Symbols and Abbreviations

Abbreviation	Description
EEG	Electroencephalography
HFO	High-Frequency Oscillations
HHD	Helmholtz-Hodge Decomposition
MCR	Multipolar Cortical Remapping
MEEG	Magnetoencephalography and Electroencephalography
MEG	Magnetoencephalography
SNR	Signal-to-Noise Ratio

List of Figures

Part 1

Introduction

Background

Techniques for the observation of the Human brain

Exploration of the Human brain is of utmost intellectual interest: deciphering brain using brain is a challenging task. Although a great deal has been learnt about brain anatomy and physiology, the fundamental questions how brain store, retrieve and processes information is still largely unknown and full discovery of these mechanisms is the foundational purpose of neuroscience.

When brain processes information, electrophysiological currents flow within and outside neural cells, thus producing electric and magnetic fields that are accessible to external measurements. Indeed, signs of this electrical neural activity in the brain can be measured with electrodes at the scalp or with very sensitive magnetic detectors placed very near the scalp. The technique of electrical measurements from the scalp is called electroencephalography (EEG) [8]. Historical and recent EEG setups are shown in Figure 1. The technique measuring magnetic signals generated by neural currents is called Magnetoencephalography (MEG) [15].

The magnetic field produced by neural current sources are very weak and are at least 8 orders of magnitude smaller than the earth static magnetic field, as shown Figure 2. These fields are currently picked using series of magnetometers coupled with super-conducting quantum interference devices (SQUID). A SQUID

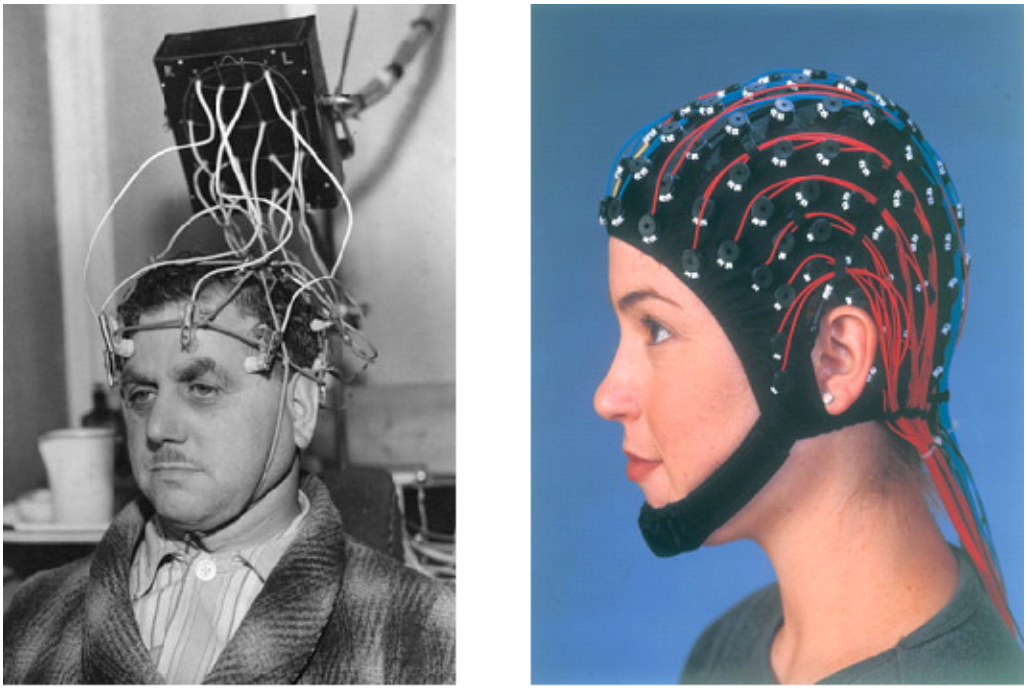

Figure 1: (a) EEG setup in 1970's. (b) Modern EEG setup with quick-fix cap.

is a sensitive detector of magnetic flux, which was developed by James Zimmerman [114] in the late 1960's.

The seminal, original MEG measurements were performed at MIT in May, 1971 by Cohen. Alpha *waves* (electromagnetic brain oscillations in the frequency range of [8,12] Hz) were recorded as shown Figure 3.a. A typical, state-of-the-art MEG setup using 151 channels is shown Figure 3.b.

Brain imaging techniques can be divided into two categories: structural and functional. Anatomical structures can be investigated using computer-aided tomography (CT) scans and better so using more recent magnetic resonance imaging approaches (MRI). For functional imaging beside neural electromagnetic signals, brain metabolism, blood flow and volume (hemodynamics) can be accessed using radioactively-labeled organic probes that are involved in the processes of interest such as glucose metabolism or dopamine synthesis. Images of dynamic changes

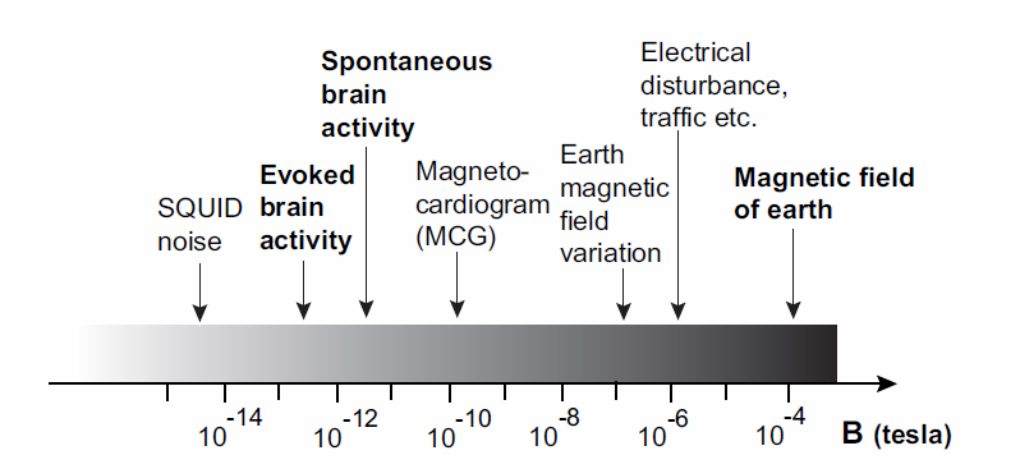

Figure 2: Comparison of brain signals with other sources of electromagnetic waves.

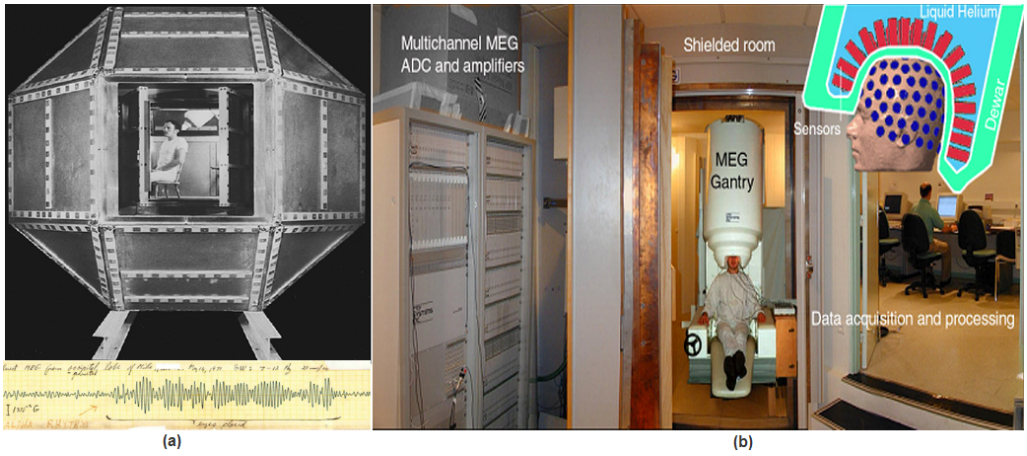

Figure 3: (a)First MEG recording at MIT inside a spaceship like magnetic shielded room using single channel SQUID. (b) MEG Setup at La Pitié-Salpêtrière Hospital, Paris inside modern multilayer shielded room using 151 SQUIDs covering whole brain.

in the spatial distribution of these probes, as they are transported and chemically modified within the brain, can be imaged using positron emission tomography (PET). These images can reach a spatial resolutions as high as 3mm. However, temporal resolution is limited to minutes by the dynamics of the physiological processes generating the signal of interest, and by photon-counting noise. For more direct studies of neural activity, one can investigate local hemodynamic changes.

As neurons become active, they induce very localized changes in blood flow and oxygenation levels that can be imaged as a correlate of neural activity [65].

Hemodynamic changes can be detected using PET, functional Magnetic Resonance Imaging (fMRI), and transcranial optical imaging methods. Of these, fMRI is currently the most widely used and can be readily performed using a standard 1.5T clinical MRI magnet although an increasing fraction of studies are now performed on higher field (3-7T) machines for improved SNR and resolution. Functional MRI studies are capable of producing spatial resolutions as high as 2-4mm; however, temporal resolution is again limited by the relatively slow hemodynamic response, when compared to electrical neural activity, to approximately one second. In addition to limited temporal resolution, interpretation of fMRI data is hampered by the rather complex relationship between the blood oxygenation level dependent (BOLD) changes that are detected by fMRI and the underlying neural activity. Regions of BOLD changes in fMRI images do not necessarily correspond one-to-one with regions of electrical neural activity [62].

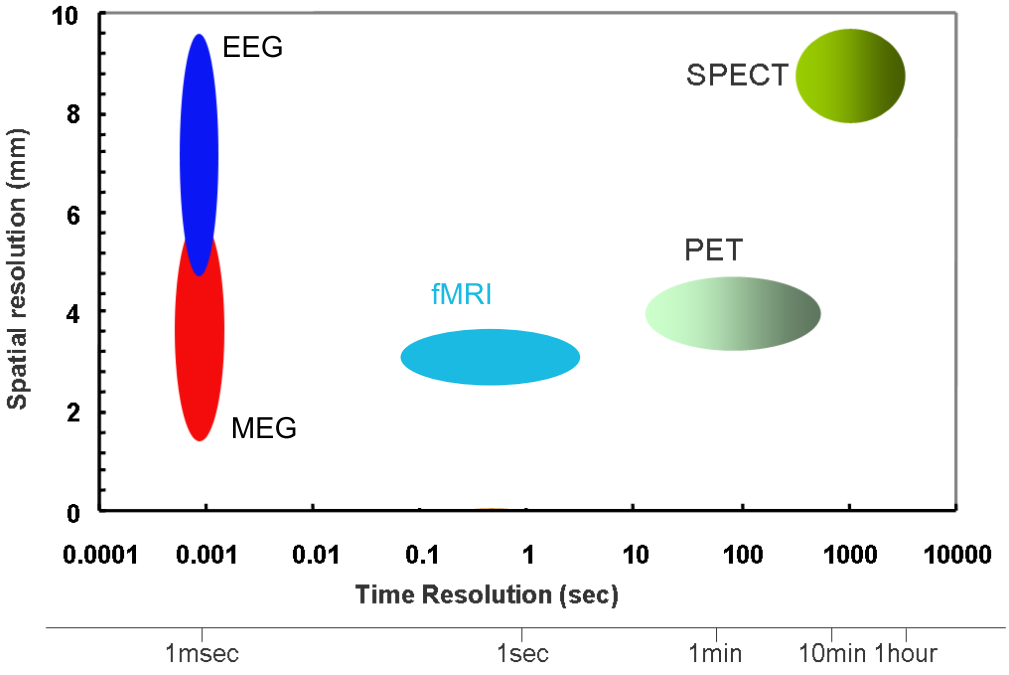

Figure 4: Spatial and temporal resolution of different brain imaging methods.

Introduction to MEG and EEG:

EEG and MEG measure the combined activity of multiple areas of the brain as a mixture of complex signal patterns. A primary objective is to interpret the complex patterns of the measured electric potentials and magnetic fields, in terms of the respective locations and time-courses of their underlying sources. The key to this task is to design a physical and numerical model to account for the origin of the field patterns captured by MEG/EEG surface recordings. Estimation of the electric and magnetic field patterns for a given model of the volume conductor is a *forward problem*, following the nomenclature of modeling data formation as encountered in a large variety of applications (from geophysics to medical imaging) [96].

The estimation of neural currents from measured field patterns is a typical *inverse problem*. In EEG or MEG studies, the simplest way to model the geometry of the head is to use a single sphere approximation or concentric spherical shells each with homogeneous isotropic conductivity [76].

The main reason why considering spherical geometry is the availability of analytical solutions, and therefore fast implementations, to solve the forward modeling problem. However a spherical approximation of the head complex geometry is likely to induce large source localization errors [72].

Using MRI, it is possible to provide more realistic geometrical models of the head. Numerical techniques such as the Boundary Element Method (BEM) and Finite Element Method (FEM) provide the flexibility of utilizing a realistic geometry [51].

EEG and MEG scalp patterns are qualitatively orthogonal to each other (see figure 5), providing distinctive information about the underlying neural current distributions. They therefore might be viewed as complementary rather than as competing modalities [24]. Most state-of-the-art MEG facilities are equipped for simultaneous acquisition of EEG and MEG data. Inverse methods for the two imaging techniques are very closely related and can even be combined and optimized for joint source localization [93, 6].

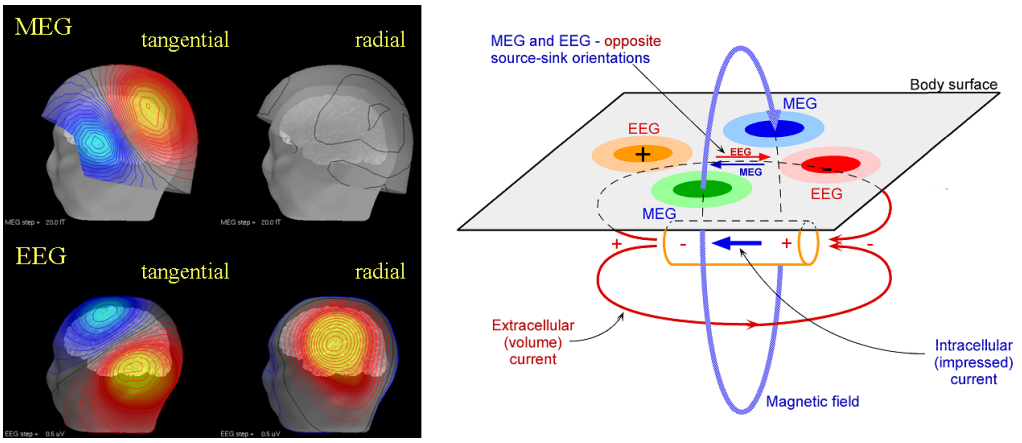

Figure 5: Left hand side figure represent the topographic sensitivity maps of MEG and EEG for radial and tangential dipoles. Figure on right hand side shows the orthogonality of MEG and EEG field patterns. patterns

Neural bases of brain electromagnetic signature

MEG and EEG (MEEG) are two techniques based on what Galvani, at the end of the 18th century, called "animal electricity", today better known as electrophysiology [85]. Despite the apparent simplicity in the structure of the neural cell, the biophysics of neural current flow relies on complex models of ionic current generation and conduction [48]. Roughly, when a neuron is excited by other neurons via an afferent volley of action potentials, postsynaptic potentials (PSPs) are generated at its apical dendritic tree. When the excitatory PSP's become larger than inhibitory PSP's, the apical dendritic membrane becomes transiently depolarized and consequently extracellularly electronegative with respect to the cell soma and the basal dendrites. This potential difference causes a current to flow through the volume conductor from the non-excited membrane of the soma and basal dendrites to the apical dendritic tree sustaining the PSP's. Some of the current takes the shortest route between the source and the sink by travelling within the dendritic trunk (see figure 6). Conservation of electric charges imposes that the current loop be closed with extracellular currents flowing even through the most distant part of the volume conductor. Intracellular currents are commonly called primary current, while extracellular currents are also known as

secondary, return, or volume currents.

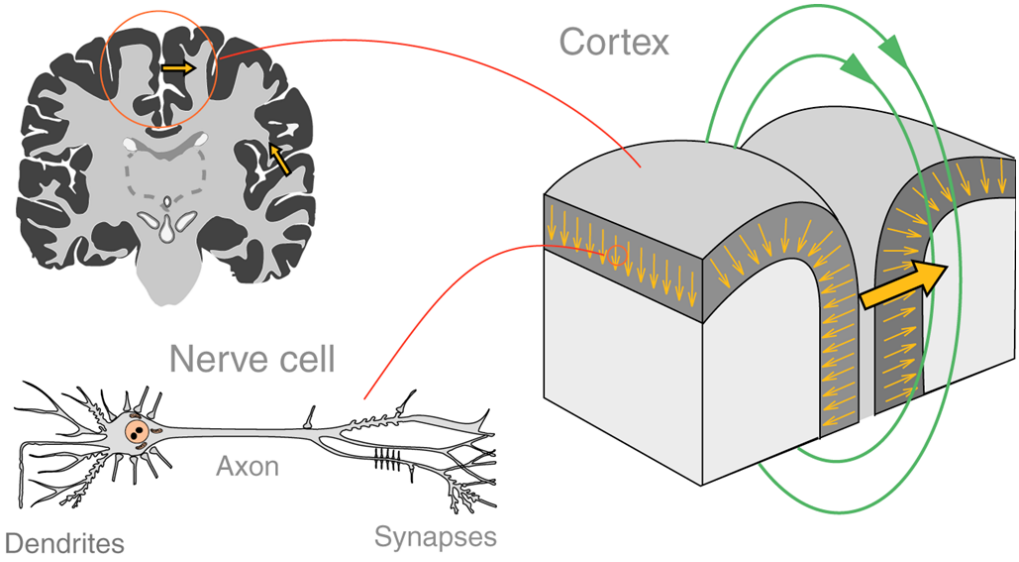

Figure 6: The orientation of pyramidal neurons is normal to the cortex surface. MEG signals preferentially reflect the current flow from pyramidal cells oriented tangential to the skull surface.

Both primary and secondary currents contribute to magnetic fields outside the head and to electric scalp potentials, but spatially structured arrangements of cells are of crucial importance to the superposition of neural currents such that they produce measurable fields. Macro-columns of tens of thousands of synchronously activated large pyramidal cortical neurons are thus believed to be the main MEG and EEG generators because of the coherent distribution of their large dendritic trunks locally oriented in parallel, and pointing perpendicularly to the cortical surface. The PSPs generated among their dendrites are believed to be at the source of most of the signals detected in MEG and EEG because they typically last longer than the rapidly firing action potentials travelling along the axons of excited neurons. Indeed, calculations such as those shown in [44] suggest each synapse along a dendrite may contribute as little as a 20 fA.m current source, probably too small to measure in MEEG. Empirical observations instead suggest we are seeing sources on the order of 10 nA.m, hence the cumulative summation of millions of synaptic junctions in a relatively small region. Nominal calculations

of neuronal density and cortical thickness suggest that the cortex has a macrocellular current density of the order of $100nA.mm^{-2}$ [44]. If we assume that the cortex is about 4 mm thick, then a small patch of size 5 mm x 5 mm would yield a net current of 10 $nA.m$, consistent with empirical observations and invasive studies [44].

In MEEG studies, one is usually concerned with the uppermost layer of the brain; the cerebral cortex, which is a 2 to 6 mm thick sheet of gray tissue where most of the measured neural activity takes place. The section of cortex is illustrated in Figure 6. At least 10 billion neurons reside in the whole cortex tissue. The total surface area of the cortex is about 2500 cm^2 , folded in a complicated way, so that it fits within the innerskull volume. The true spatial extent of realistic current sources associated with brain activation varies according to the cause of the activation. Typically sensory stimuli activate cortical areas starting from a few mm^2 up to a few cm^2, whereas for spontaneous activity and epileptic foci can involve an activation area up to tens of cm^2 [95].

At a larger scale, distributed networks of collaborating and synchronously activated cortical macro-columns are major contributors to MEG and EEG signals [80]. This is compatible with neuro-scientific theories that model basic cognitive processes in terms of dynamically interacting cell assemblies [105].

Most regions of the cortex are mapped functionally. For example, the primary somatosensory cortex receives tactile stimuli from the skin. Areas of the frontal lobe are concerned with the integration of muscular activity. Primary motor cortex is involved in the movement of a specific part of the body. Large areas of cortex are devoted to body parts, which are most sensitive to touch (*e.g.*, lips) or to the parts where accurate control of muscles is needed (*e.g.*, fingers).

Forward problem

In order to analyze the electric and magnetic data obtained from EEG and MEG measurements, we need to mathematically model the relationship between mea-

sured electric/magnetic fields and the current distribution which produce it. This relationship is known as forward modeling which translates as a lead-field matrix or a gain matrix that binds the amplitude of source currents to the sensor data as we shall detail below. If the primary source and the surrounding conductivity profile of tissues are known, the electric potential and magnetic field can be calculated from Maxwell's equations (see [7] for a comprehensive review of MEG forward and inverse modeling).

Maxwell's equations

In 1873, Maxwell showed that electromagnetic fields can be described using only 4 vector differential equations [70]:

$$\nabla \times \mathbf{E} + \frac{\partial \mathbf{B}}{\partial t} = 0, \tag{1}$$

$$\nabla \cdot \mathbf{B} = 0, \tag{2}$$

$$\nabla \cdot \mathbf{E} = \frac{\rho}{\epsilon_0}, \tag{3}$$

$$\nabla \times \mathbf{B} = \mu_0(\mathbf{J} + \epsilon_0 \frac{\partial \mathbf{E}}{\partial t}), \tag{4}$$

where $\mathbf{E}$ is the electric field, $\mathbf{B}$ the magnetic field, ρ the charge density, and ϵ_0 and μ_0 represent the permittivity and the permeability of the empty space with values 8.85 10^{-12} Fm^{-1} and $4\pi 10^{-7}\mathrm{Hm}^{-1}$, respectively (the magnetic permeability μ_0 of brain tissues is considered identical to that of the free space).

Neglecting the effects of the time-dependent terms is the quasi-static approximation of Maxwell's equations. This depends on the typical frequency range of the signals of interest and the properties of the medium. The frequency of the signals obtained from bio-electromagnetic measurements in MEG and EEG are typically below 1 KHz. It has therefore been verified that the physics of MEG and EEG are well described using the quasi-static approximation of Maxwell's equations [44]. Quasi-static Maxwell's equations can be written as:

$$\nabla \times \mathbf{E} = 0, \tag{5}$$

$$\nabla \cdot \mathbf{B} = 0, \tag{6}$$

$$\nabla \cdot \mathbf{E} = \frac{\rho}{\epsilon_0}, \tag{7}$$

$$\nabla \times \mathbf{B} = \mu_0 \mathbf{J}. \tag{8}$$

Equation (5) can further be satisfied by representing the electric field $\mathbf{E}$ as the gradient of a scalar function V:

$$\mathbf{E} = -\nabla V. \tag{9}$$

From (8), we obtain the relation between the current distribution $\mathbf{J}(\mathbf{r}')$ at point $\mathbf{r}'$ and the magnetic field $\mathbf{B}(\mathbf{r})$ measured at $\mathbf{r}$ which reads:

$$\mathbf{B}(\mathbf{r}) = \frac{\mu_0}{4\pi} \int \mathbf{J}(\mathbf{r}') \times \frac{\mathbf{r} - \mathbf{r}'}{||\mathbf{r} - \mathbf{r}'||^3} dv', \tag{10}$$

where $||.||$ represents the Euclidean norm.
This relationship (10) is popularly known as Biot-Savart Law.

The current distribution $\mathbf{J}(\mathbf{r})$ can be divided into two parts:

1. Primary current $\mathbf{J}^p(\mathbf{r})$ produced by the neural current activity;

2. Volume current $\mathbf{J}^v(\mathbf{r})$ produced in all the volume to prevent charge buildup.

Primary and secondary currents are shown in Figure 5.b. The current distribution $\mathbf{J}(\mathbf{r})$ now can be represented as

$$\mathbf{J}(\mathbf{r}') = \mathbf{J}^p(\mathbf{r}') + \mathbf{J}^v(\mathbf{r}') = \mathbf{J}^p(\mathbf{r}') + \sigma(\mathbf{r}')\mathbf{E}(\mathbf{r}') = \mathbf{J}^p(\mathbf{r}') - \sigma(\mathbf{r}')\nabla V(\mathbf{r}'), \tag{11}$$

where $\sigma(\mathbf{r}')$ is the electrical conductivity of the tissue at location $\mathbf{r}'$, which we will consider to be isotropic throughout this thesis. See Figure 7) where the head consists of regions of constant conductivities $\sigma_i, i = 1, 2, \ldots, N+1$.

Now we can rewrite the Biot-Savart equation (10) and use (11) to divide it into two parts: the first part consists of $\mathbf{B}_0(\mathbf{r})$, the magnetic field due to primary currents only while the second term is due to the contribution of volume currents, formed as a sum of surface integrals over the brain-skull, skull-scalp and scalp-air boundaries. In fact, we have

$$\mathbf{B}(\mathbf{r}) = \mathbf{B}_0(\mathbf{r}) + \frac{\mu_0}{4\pi} \sum_{ij} (\sigma_i - \sigma_j) \int_{S_{ij}} V(\mathbf{r}') \frac{\mathbf{r} - \mathbf{r}'}{||\mathbf{r} - \mathbf{r}'||} \times dS'_{ij}. \tag{12}$$

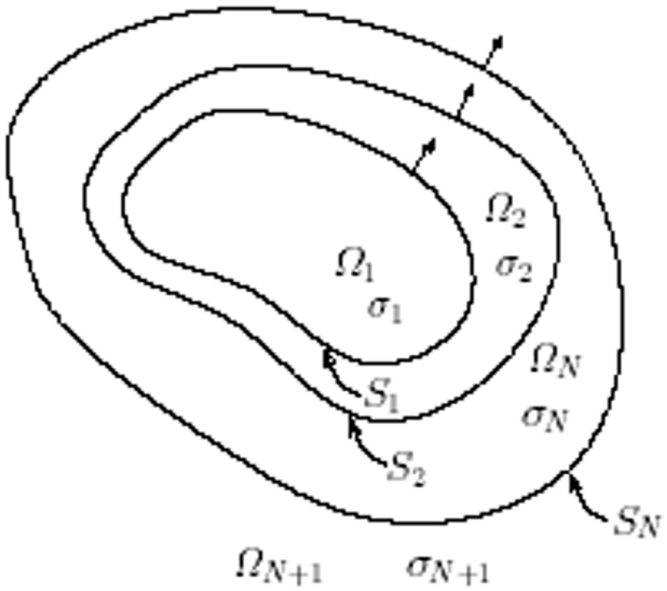

Figure 7: Shell model of the head.

This general equation states that the magnetic field can be calculated if we know the primary current distribution and the potential $V(\mathbf{r}')$ on all the surfaces S_{ij}. We can create a similar equation for the potential itself, yielding

$$(\sigma_i + \sigma_j)V(\mathbf{r}) = 2\sigma_0 V_0(\mathbf{r}) - \frac{1}{2\pi}\sum_{ij}(\sigma_i - \sigma_j)\int_{S_{ij}} V(\mathbf{r}')\frac{\mathbf{r}-\mathbf{r}'}{||\mathbf{r}-\mathbf{r}'||}\times dS'_{ij}, \qquad (13)$$

where $V_0(\mathbf{r})$ is the potential at $\mathbf{r}$ due to the primary current distribution.

If we specify a primary current distribution $\mathbf{J}^p(\mathbf{r}')$, we can calculate a primary potential and a primary magnetic field as follows

$$V_0(\mathbf{r}) = \frac{1}{4\pi\sigma_0}\int \mathbf{J}^p(\mathbf{r}')\cdot\frac{\mathbf{r}-\mathbf{r}'}{||\mathbf{r}-\mathbf{r}'||}\times dS'_{ij}, \qquad (14)$$

$$\mathbf{B}_0(\mathbf{r}) = \frac{\mu_0}{4\pi}\int \mathbf{J}^p(\mathbf{r}')\cdot\frac{\mathbf{r}-\mathbf{r}'}{||\mathbf{r}-\mathbf{r}'||}\times dS'_{ij}. \qquad (15)$$

The primary potential is then used to solve (13) for the potentials on all the surfaces, and therefore completes the resolution of the forward problem. These surface potentials $V(\mathbf{r})$ and the primary magnetic field $\mathbf{B}_0(\mathbf{r})$ are then used to

solve (12) for the external magnetic fields. Unfortunately, the solution to (13) is analytic only in a special shapes and elliptic volume conductor and must otherwise be solved numerically. This thesis will consider using spherical head models only.

In the next two sections, models for neural current distribution will be introduced and subsequently models for volume conductor will be discussed.

Modeling primary currents

Consider a small patch of active cortex $\mathcal{S}(\mathbf{r}')$ centered at $\mathbf{r}'$ and an observation point $\mathbf{r}$ at some distance from this patch. The primary current distribution in this case can be well represented by the multipolar representation $\mathbf{\Omega}^n_{\mathcal{S}((r'))}$ given by

$$\mathbf{\Omega}^n_{\mathcal{S}((r'))} = \frac{1}{n!}\int_{\mathbf{r}'\subset\mathcal{S}((r'))} (\mathbf{r}' - \mathbf{l})^n \mathbf{J}^p(\mathbf{r}')d\mathbf{r}', \tag{16}$$

where $\mathbf{l}$ is the point of expansion for multipoles.

It is important to note that the brain activity does not actually consist of discrete sets of physical current dipoles, but rather that the dipole is a convenient representation for coherent activation of a large number of pyramidal cells, possibly extending over a few square centimeters of gray matter.

If the primary current distribution is very focal then it can be well approximated by an equivalent current dipole (ECD) defined as:

$$\mathbf{\Omega}^0 = \mathbf{q} \equiv \int \mathbf{J}^p(\mathbf{r}')d\mathbf{r}'. \tag{17}$$

The ECD can be represented as a point source

$$\mathbf{J}^p(\mathbf{r}') = \mathbf{q}\delta(\mathbf{r}' - \mathbf{l}), \tag{18}$$

where $\delta(\mathbf{r})$ is the Dirac delta distribution. Note that an ECD is a multipolar expansion of order 0.

If the current distribution is not focal, then multipolar expansions are better suited for the modeling of neural sources. The contributions reported [74, 54, 53] describe this issue in great details.

Multipolar expansions will be explained in detail in Chapter 2 of this thesis.

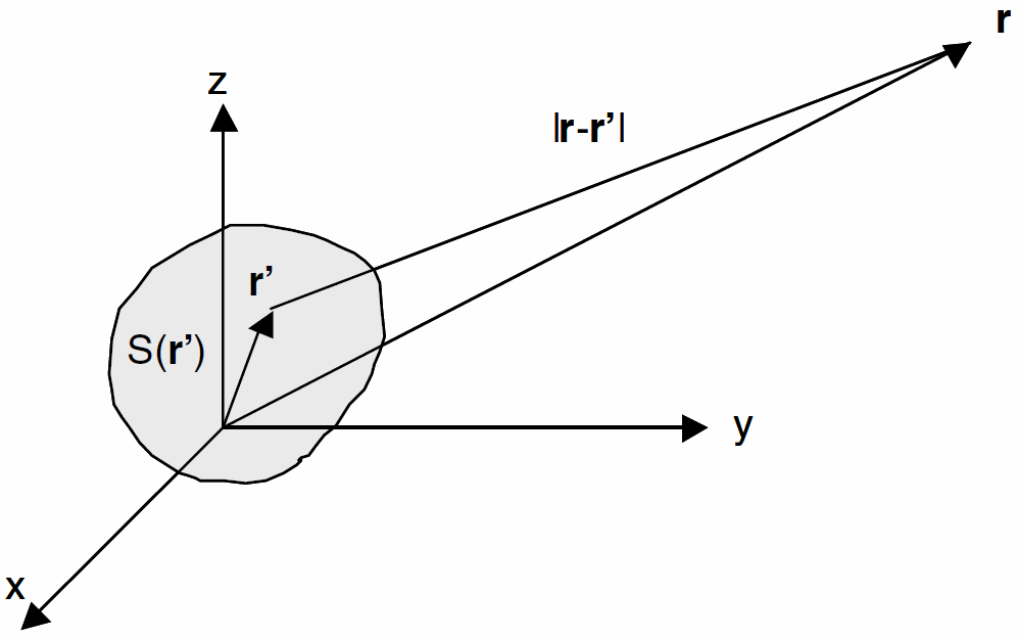

Figure 8: Current Distribution $\mathcal{S}(\mathbf{r}')$ centered at $\mathbf{r}'$ and measured at $\mathbf{r}$. *Adapted from [54].*

Head modeling

Spherical head model

Head modeling using as spherical approximation of its geometry has been widely used in the MEG community, the reason for its popular use is the simplicity it offers with respect to computation requirements. Computing scalp potentials and induced magnetic fields require solving the forward equations (13) and (12) respectively for a particular source model. We have seen above that when the surface integrals are computed over realistic head shapes, these equations must be solved numerically. However, analytic solutions exist for simplified geometries, such as when the head is assumed to consist of a set of nested concentric homogeneous spherical shells representing brain, skull, and scalp respectively. These models are routinely used in most clinical and research applications to E/MEG source localization. Figure 9 describes a spherical head model approximation. Consider the special case of a current dipole, with moment $\mathbf{q}$, located at $\mathbf{r}_q$ in a multi-shell

spherical head, and a MEG system in which we only measure the radial component of the external magnetic field, *i.e.*, the coil surface of the magnetometer is oriented orthogonally to a radial line from the center of the sphere through the center of the coil. It is relatively straightforward to show that the contributions of the volume currents vanish in this case, and we are left with only the primary term. Taking the radial component of this field for the current dipole reduces to the remarkably simple form:

$$B_r(\mathbf{r}) = \frac{\mathbf{r}}{r} \cdot \mathbf{B}(\mathbf{r}) = \frac{\mathbf{r}}{r} \cdot \mathbf{B_0}(\mathbf{r}) + \frac{\mu_0}{4\pi} \cdot \sum_{ij} (\sigma_i - \sigma_j) \int_{S_{ij}} V(\mathbf{r}') \frac{\mathbf{r}}{r} \frac{\mathbf{r} - \mathbf{r}'}{||\mathbf{r} - \mathbf{r}'||} \times dS'_{ij}. \quad (19)$$

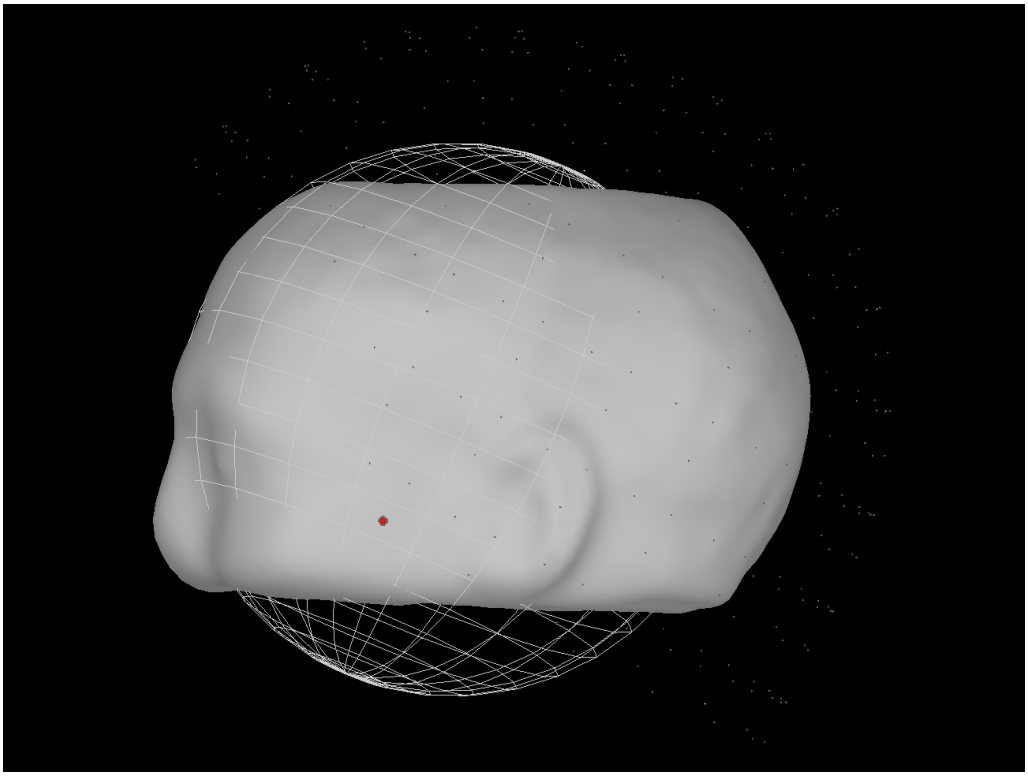

Figure 9: Spherical head model, where a sphere is fitted to the head geometry.

In this same case, it is very simple to show that the contribution of volume currents will also reduce to zero. Hence the second term in 19 vanishes and this equation write the following simpler form:

$$B_r(\mathbf{r}) = \frac{\mathbf{r}}{r} \cdot \mathbf{B_0}(\mathbf{r}) = \frac{\mu_0}{4\pi} \frac{\mathbf{r} \times \mathbf{r}'}{r||\mathbf{r} - \mathbf{r}'||^3} \cdot \mathbf{q}. \quad (20)$$

Notice here that the magnetic field $B_r(\mathbf{r})$ is linear with respect to the dipole moment $\mathbf{q}$ but highly nonlinear with respect to dipole location: $\mathbf{r_q}$.

In nutshell, $B_r(\mathbf{r})$ is zero everywhere outside the head if $\mathbf{q}$ points towards the radial direction $\mathbf{r_q}$. A more general result is that radially-oriented dipoles do not produce any external magnetic field outside a spherically symmetric volume conductor, regardless of the sensor orientation [89].

Importantly, this is not the case for EEG which is sensitive to radial sources, which demonstrates one of the complementary differences between MEG and EEG principles.

Realistic head model

In reality, the head has anisotropic tissue properties, is inhomogeneous and not spherical but surprisingly, the spherical approximation works reasonably well, particularly for MEG, which is less sensitive than EEG to volume currents. These latter are more affected than primary currents by deviations from the idealized model. By using the individual MRI data from the subject, it is possible to construct a more detailed head model by isolating different regions of interest using fully-automatic segmentation techniques [16]. Figure 10 shows typical surface and volume tessellations for use with BEM and FEM (see [33] for a complete review of the head geometries used in MEG).

Two types of approaches are available for realistic head modeling:

1. *Boundary Element Method (BEM)* BEM is a numerical technique of solving linear partial differential equations which have been formulated in a boundary integral form. Normally in MEG, single-shell and three-shell BEM methods are used. BEM methods still assume homogeneity and isotropy within each region of the head. It therefore ignores, for example, the conductivity anisotropy induced by white matter tracts, where conduction is higher along axonal fibers compared to a transverse direction. Similarly, the sinuses and diploic spaces in the skull make it very inhomogeneous, a factor that is typically ignored in BEM calculations.

2. *Finite Element Method (FEM)*) FEM is a numerical technique for finding approximate solutions of partial differential equations (PDE). In FEM, discretization of the PDE is performed in the entire head volume. Anisotropy and heterogeneity in different tissue types can therefore be modeled and therefore represents a very comprehensive approach to solving the MEEG forward problem.

Typically, BEM and FEM calculations are very time consuming and their use may be considered as impractical when incorporated as part of an iterative inverse solver for current sources. In fact, through use of fast numerical methods, pre-calculation, and look-up tables and interpolation of pre-calculated fields, both FEM and BEM can be made quite practical for applications in MEG and EEG [31]. One problem remains: these methods reauire the conductivity properties of head tissues be known. Most of head models used in the bio-electromagnetism community consider typical values for the conductivity of the brain, skull and skin. Skull is typically assumed to be 40 to 90 times more resistive than brain and scalp, which are assumed to have similar conductive properties. These values were measured in vitro from postmortem tissue samples, with conductivity values that may be significantly altered from those in in vivo tissues however. Consequently, some recent research efforts have focused on in vivo measurements of tissue conductivity. Electrical Impedance Tomography (EIT) proceeds by injecting a small current (1-10 microA) between pairs of EEG electrodes and by measuring the resulting potentials at all electrodes. Given a model for the head geometry, EIT solves an inverse problem by minimizing the error between the measured potentials on the rest of the EEG leads and the model-based computed potentials, in terms of parameters of the conductivity profile. Simulation results with three or four-shell spherical head models have demonstrated the feasibility of this approach though the associated inverse problem is also fundamentally ill-posed [32]. These methods are readily extendible to realistic surface models as used in BEM calculations in which each region is assumed homogeneous, but it is unlikely that the EIT approach will be able to produce high-resolution images

of spatially varying anisotropic conductivity. A second approach to imaging conductivity is to use magnetic resonance. One technique uses the shielding effects of induced eddy currents on spin precession and could in principle help determine the conductivity profile at any frequency [113]. The second technique uses diffusion-tensor imaging with MRI (DT-MRI) that probes the microscopic diffusion properties of water molecules within the tissues of the brain. The diffusion values can then be tentatively related to the conductivity of these tissues [100]. None of these MR-based techniques have reached common practise by far . Further, given the poor signal-to-noise ratio (SNR) of the MR in bone regions, which is of critical importance for the forward EEG problem, the potential for fully 3D impedance tomography with MR remains speculative.

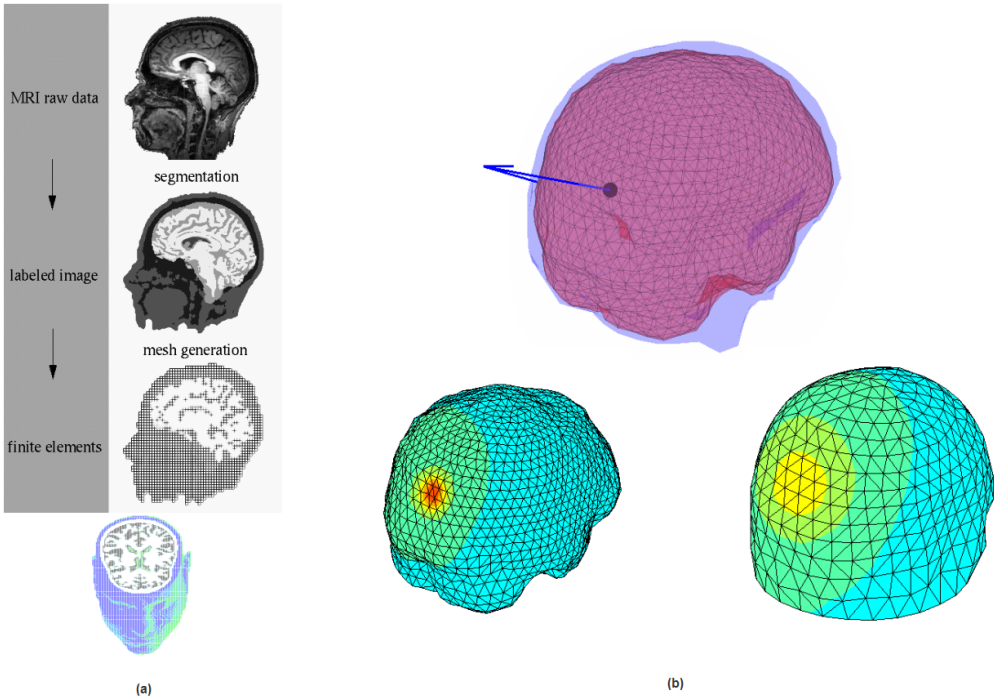

Figure 10: (a) FEM modeling of the forward model; (b) BEM modeling of the forward model.

Linear formulation

The forward problem now can be explained using the models for sources and head geometry discussed above. The magnetic field and scalp potential measurements are linear with respect to the dipole moment $\mathbf{q}$ and nonlinear with respect to its location $\mathbf{r}'$. For clarity, it is convenient to separate the dipole magnitude $q = ||\mathbf{q}||$ from its orientation $\mathbf{u} = \mathbf{q}/||\mathbf{q}||$, which we write in spherical coordinates by $\Theta = [\phi, \rho]$. Let $b(\mathbf{r})$ denote the magnetic field generated by a dipole having fixed orientation Θ:

$$b(\mathbf{r}) = g(\mathbf{r}, \mathbf{r}_q, \mathbf{\Theta})q, \tag{21}$$

where $g(\mathbf{r}, \mathbf{r}_q, \mathbf{\Theta})$ is a lead field solution of the magnetic field for a dipole having unit amplitude and orientation Θ.

For N dipoles located at $\mathbf{r_{q_i}}$, their combined magnetic fields can be expressed using linear superposition of Maxwell's equations as

$$b(\mathbf{r}) = \sum_{i=1}^{N} g(\mathbf{r}, \mathbf{r}_{q_i}, \mathbf{\Theta}_i)q_i. \tag{22}$$

The simultaneous MEG measurements made at m sensors for N dipoles, can be expressed as

$$\mathbf{B} = \begin{bmatrix} B(\mathbf{r}_1) \\ \vdots \\ B(\mathbf{r}_m) \end{bmatrix} = \begin{bmatrix} G(\mathbf{r}_1, \mathbf{r}_{q1}, \Theta_1) & \dots & G(\mathbf{r}_1, \mathbf{r}_{qN}, \Theta_N) \\ \vdots & \ddots & \vdots \\ G(\mathbf{r}_m, \mathbf{r}_{q1}, \Theta_1) & \dots & G(\mathbf{r}_m, \mathbf{r}_{qN}, \Theta_N) \end{bmatrix} \begin{bmatrix} q_1 \\ \vdots \\ q_p \end{bmatrix}. \tag{23}$$

It can be written in a matrix form as

$$\mathbf{B} = \mathbf{G}(\{\mathbf{r}_{qi}, \Theta_i\})\mathbf{J}, \tag{24}$$

where $\mathbf{G}(\{\mathbf{r}_{qi}, \Theta_i\})$ is the $m \times N$ gain matrix relating N dipoles to the m sensors. Each column contains the contribution of one dipole to each sensor in the array. The matrix $\mathbf{J}$ contains the set of instantaneous amplitudes of all the dipoles.

In this model, the orientation of the dipole is not a function of time. This type of model is often referred to as a "fixed" dipole model. Alternative models that allow these dipoles to "rotate" as a function of time are known as "unconstrained" dipole model [75].

Inverse problem

To produce estimates of the neural current sources that generated the observed MEG signals, we must solve the associated quasi-static electromagnetism inverse problem. The inherent ill-posedness of this problem, coupled with the limited number of spatial measurements available with current MEG and EEG systems, (150-300 measurements) and signal-to-noise ratio (SNR) make this estimation very challenging [44].

The solutions to the neuromagnetic inverse problem will depend on which forward model is used. In fact, a given inverse algorithm will yield slightly different results if different forward models are used; hence, the importance of using an accurate realistic forward model. However, these two problems are relatively independent of one another. In the forward problem, we attempt to model the classical physics of MEG and EEG as realistically as possible. In contrast, in the inverse problem, we often deal with purely mathematical concepts and *a priori* assumptions that are incorporated in a source model. The independence of the inverse problem from the model's physics allows one to use the same inverse algorithm for MEG or EEG. On the other hand, many different estimates of activity can be obtained for a particular data set using different inverse algorithms but sharing the same forward model. This brings us to the main issue with neuromagnetic inverse estimation: nonuniqueness. There is no unique solution to the physically and mathematically ill-posed neuromagnetic inverse problem. In fact, an infinite number of current source distributions can in theory generate any particular magnetic field measurement vector due to the existence of magnetic silent sources [47, 44, 89].

In both MEG and EEG, silent sources can be added to any given inverse solution without changing the forward field and/or potential that the combined source generates. Thus, there are indeed an infinite number of solutions that explain any given MEG/EEG data set equally well. Therefore, *a priori* assumptions about the sources are implicitly or explicitly formulated to find solutions with specific properties [5, 19, 23, 25, 79, 83]. It should be emphasized that even

though mathematically unique solutions can be obtained by postulating special source properties, physical non-uniqueness is intrinsic to the neuromagnetic inverse problem.

The two major approaches to the estimation of neural current sources are "imaging" and "parametric/localization" methods.
Imaging methods typically constrain sources to a tessellated surface representation of the cortex, assume an elemental current source in each area element (vertex) normal to the cortex surface, and solve the linear inverse problem that relates these current sources to the measured data. Accurate tessellation of the cortex requires on the order of 10^5 elements. Since the maximum number of MEG sensors is about 300, the problem is highly under-determined. By using regularized linear methods based on minimizing a weighted l^2-norm on the image, we can produce unique stable solutions.

Parametric/localization methods assume a specific parametric form for the sources. By far the most widely used models in MEG are multiple-current-dipole approaches [112, 90]. These assume that the number of neural sources is relatively small and each sufficiently focal that they can be represented by a few equivalent current dipoles with unknown locations and orientations. In both imaging and parametric methods, the MEG/EEG forward problem can be written as

$$\mathbf{B} = \mathbf{G}(\theta)\mathbf{J} + \epsilon, \tag{25}$$

where $\mathbf{B}$ is the $M \times time$ vector representing MEG measurements, $\mathbf{J}$ is the $N \times time$ vector representing the distribution currents. For imaging methods, it is the amplitude of elementary currents at each cortical vertex. In parametric methods, it is the values of amplitude parameters for each current model element. $\mathbf{G}(\theta)$ is the $M \times N$ lead field matrix relating additional parameters of the current distribution to the magnetic field measured by M sensors. θ gathers the parameters which the lead fields depend uppon, *i.e.*, current sources, locations $\mathbf{r}_{q_i}$, orientations Θ_i and their amplitudes q_i. The $M \times time$ noise vector ϵ represents a combination of system noise and far-field electromagnetic perturbations (power lines, elevators,

activity of heart and eyes, etc) on sensors.

Parametric methods

Parametric methods can be broadly classified into "Dipole fitting" and "Beamforming".

Dipole fitting

The first inverse method for equation (25) is based on the assumption that neural activity can be modeled by a few sparse, elementary sources α. The problem reduces to the estimation from the data of the parameters θ for α sources, which are described as their positions $\mathbf{r}_{q_i}$, their orientations Θ_i and their amplitudes q_i (with $i \in [1, \alpha]$). This may be written as an optimization problem of a cost function to be minimized.

The estimate in the least-squares (LS) sense writes:

$$\mathbf{J}(\theta)_{LS} = \arg\min_{\mathbf{J}} ||\mathbf{B} - \mathbf{G}(\theta)\mathbf{J}||_F^2 \tag{26}$$

where $||.||_F$ denotes the Frobenius norm. Let $\mathbf{G}^+(\theta)$ be the pseudo-inverse of $\mathbf{G}(\theta)$:

$$\mathbf{G}^+(\theta) = \mathbf{U}\mathbf{S}^+\mathbf{V}^\mathbf{t}, \tag{27}$$

where $\mathbf{USV}^\mathbf{t}$ is the singular value decomposition (SVD) of $\mathbf{G}(\theta)$ and $\mathbf{S}^+$ is the diagonal matrix containing inverse of singular values of $\mathbf{G}(\theta)$ [39]. Equation (26) can be written in the form:

$$\mathbf{J}(\theta)_{LS} = ||\mathbf{B} - \mathbf{G}(\theta)[\mathbf{G}^+(\theta)\mathbf{B}]||_F^2 = ||(\mathbf{I} - \mathbf{G}(\theta)\mathbf{G}^+(\theta))\mathbf{B}||_F^2, \tag{28}$$

where $\mathbf{I}$ is the identity matrix of rank α. Thus, the LS problem can be optimally solved in the limited set of nonlinear parameters $\mathbf{r}_{q_i}$,Θ_i with an iterative minimization procedure. The linear parameters in q_i are then optimally estimated from 26; see [75]. Minimization methods range from Marquardt-Levenberg and Nelder-Meade downhill simplex searches to global optimization schemes using multistart methods, genetic algorithms and simulated annealing [101].

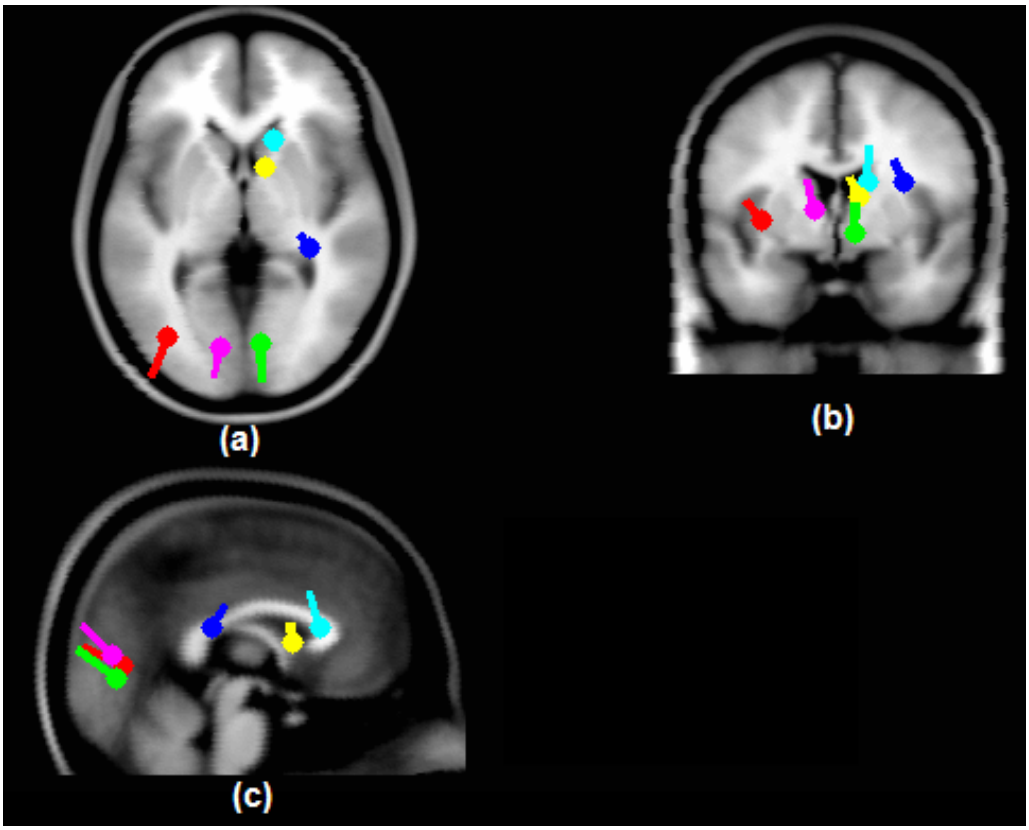

Figure 11: (a) Dipole Fitting in axial view; (b) Dipole Fitting in coronal view (c) Dipole fitting in sagittal view.

This least-squares model can either be estimated from data from a single time snapshot or a time window. When applied sequentially to a set of time samples, this results in a "moving dipole" model, since the location is not constrained [112]. Alternatively, by using a contiguous time block of data in the least-squares fit, the dipole locations can optionally be fixed over the entire interval. The fixed and moving dipole models have both proven useful in both EEG and MEG and remain the most widely used approaches to processing experimental and clinical data. A key problem with the LS method is that the number of sources to be used must be decided *a priori*. Estimates can be obtained by looking at the effective rank of the data using a SVD or through information-theoretic criteria, but in practice expert data analysts often run several model orders and select results based on physiological plausibility. Caution is obviously required since a

sufficiently large number of sources can be made to fit any data set, regardless of its quality. Furthermore, as the number of sources increases, the non-convexity of the cost function results in increased chances of trapping in undesirable local minima. This latter problem can be approached using stochastic or multistart search strategies [50]. The alternatives to LS described below avoid the non-convexity issue by scanning a region of interest that can range from a single location to the whole brain volume for possible sources. An estimator of the contribution of each putative source location to the data can be derived either via spatial filtering techniques or signal classification indices. An attractive feature of these methods is that they do not require a prior estimate of the number of underlying sources.

Beamforming approaches

A beamformer performs spatial filtering on data from a sensor array to discriminate between signals arriving from a location of interest and those originating elsewhere. Beamforming originated in radar and sonar signal processing but has since found applications in diverse fields ranging from astronomy to biomedical signal processing [103].

Match filter

The simplest spatial filter, a matched filter, is obtained by normalizing the columns of the lead field matrix and transposing this normalized dictionary. The spatial filter for location $\mathbf{r}_i$ is given by

$$W_{\mathbf{i}}^{(T)} = \frac{\mathbf{G}_{:\,\mathbf{i}}^{T}}{\|\mathbf{G}_{:\,\mathbf{i}}\|_F}. \tag{29}$$

This approach essentially projects the data onto the column vectors of the dictionary. Although this guarantees that when only one source is active, the absolute maximum of the estimate corresponds to the true maximum, this filter is not recommended since this single-source assumption is usually not valid, and since

the spatial resolution of the filter is so low given the high correlation between dictionary columns. This approach can be extended to fast recursive algorithms, such as matching pursuit and its variants, which sequentially project the data or residual to the non-used dictionary columns to obtain fast suboptimal sparse estimates.

Multiple signal classification (MUSIC)

The MUSIC algorithm was adopted from spectral analysis, Direction of Arrival(DOA) estimation techniques and modified for spatial filtering of MEG data [75, 73]. The MUSIC cost function is given by

$$W_{\mathbf{i}}^{(T)} = \frac{\left\| \left(\mathbf{I} - \mathbf{U}_s \mathbf{U}_s^T \right) \mathbf{G}_{:\,i} \right\|_2^2}{\left\| \mathbf{G}_{:\,i} \right\|_2^2} = \frac{\left\| \mathbf{P}_{\mathbf{U}_s}^{\perp} \mathbf{G}_{:\,i} \right\|_2^2}{\left\| \mathbf{G}_{:\,i} \right\|_2^2}, \tag{30}$$

where $\mathbf{B} = \mathbf{USV}^T$ is the singular value decomposition of the data, $\mathbf{U}_s$ is a matrix with the first d_s right singular vectors that form the signal subspace, and $\mathbf{G}_{:\,i}$ is the gain vector for the dipole located at $\mathbf{r}_i$ and with orientation θ_i (obtained from anatomy or using the generalized eigenvalue decomposition). The operator $\mathbf{P}_{\mathbf{U}_s}^{\perp}$ is an orthogonal projection operator onto the data noise subspace. The MUSIC map is the reciprocal of the cost function at all locations scanned. This map can be used to guide a recursive parametric dipole fitting algorithm. The number d_s is usually set by an expert user.

For more complete explanation of subspace methods like MUSIC see [55].

Linearly constrained minimum-variance (LCMV)

Beamformers, as used in the field of brain imaging, are spatial filtering algorithms that scan each source-point independently to pass source signals at a location of interest while suppressing interference from other regions using only the local gain vectors and the measured covariance matrix. One of the most basic and often used linear beamformers is the linearly constrained minimum variance (LCMV) beamformer, which attempts to minimize the beamformer output power subject

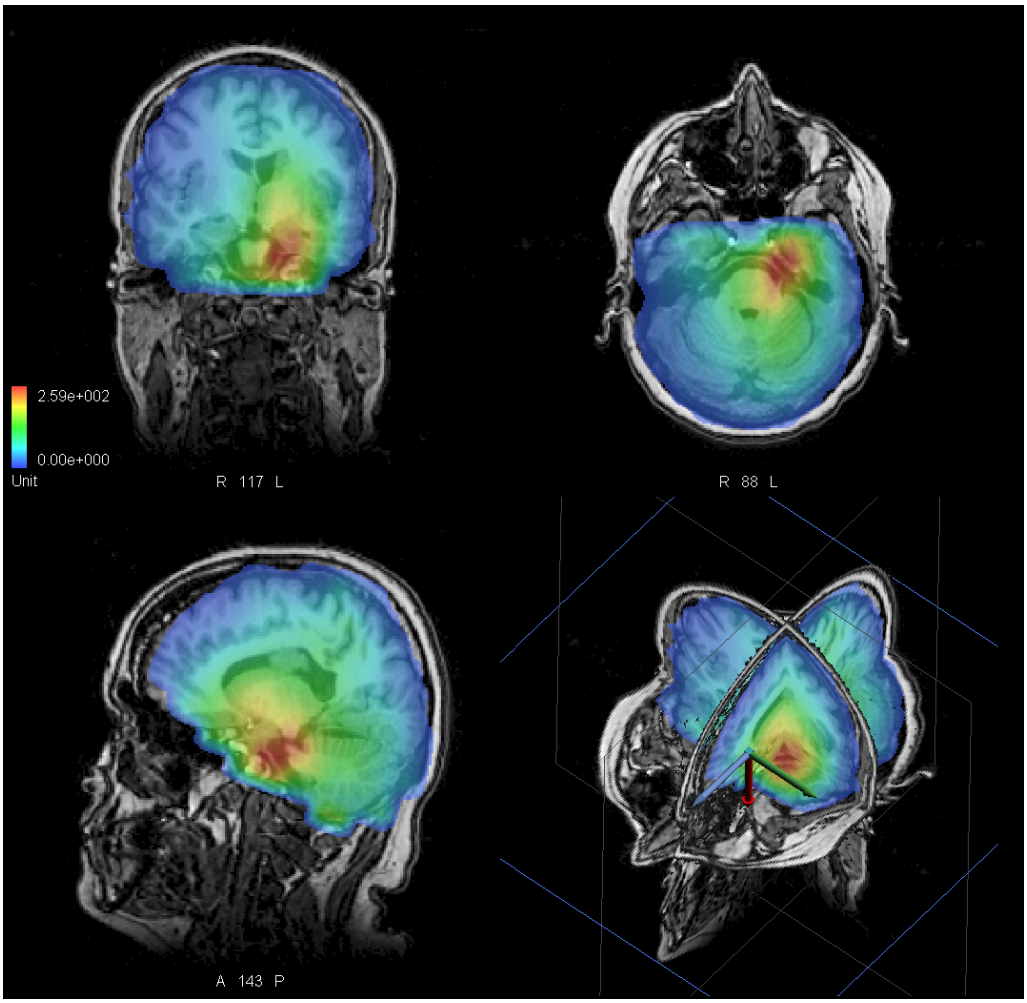

Figure 12: A typical MUSIC scan for epileptic spikes.

to a unity gain constraint:

$$\min_{W_{\mathbf{i}:}} \quad tr\left(W_{\mathbf{i}:}\Sigma_{\mathbf{B}}W_{\mathbf{i}:}^{T}\right) \text{ subject to } W_{\mathbf{i}:}\mathbf{G}_{:\,\mathbf{i}} = \mathbf{I}, \tag{31}$$

where $\Sigma_{\mathbf{B}}$ is the data covariance matrix, $\mathbf{G}_{:\,\mathbf{i}}$ is the d_b by 3 gain matrix of the i^{th} source point, and $W_{\mathbf{i}:}$ is the 3 by d_b spatial filtering matrix [104]. The solution to this problem is given by

$$W_{\mathbf{i}}^{(T)} = \left(\mathbf{G}_{:\,\mathbf{i}}^{T}{\Sigma_{\mathbf{B}}}^{-1}\mathbf{G}_{:\,\mathbf{i}}\right)^{-1}\mathbf{G}_{:\,\mathbf{i}}^{T}{\Sigma_{\mathbf{B}}}^{-1}. \tag{32}$$

The parametric source activity at the i^{th} source point is given by $\mathbf{S}_{\mathbf{i}:} = W_{\mathbf{i}:}\mathbf{B}$. This can be performed at each source-point of interest to yield a score map of

activity. This beamforming approach can be extended to a more general Bayesian graphical model that uses event timing information to model evoked responses, while suppressing interference and noise sources [115]. This approach uses a variational Bayesian EM algorithm to compute the likelihood of a dipole at each grid location.

Imaging methods

Imaging approaches to the MEG inverse problem consist of methods for estimating the amplitudes of a dense set of dipoles distributed at fixed locations and orientation within the head volume. In this case, since the locations and orientation are fixed, only the linear parameters need to be estimated and the inverse problem reduces to a linear one with strong similarities to those encountered in image restoration and reconstruction. By putting locations and orientation constraint the equation (25) becomes

$$\mathbf{B} = \mathbf{GJ} + \epsilon. \tag{33}$$

Here the gain matrix $\mathbf{G}$ is fixed and only dipole amplitudes $\mathbf{J}$ have to be estimated.

The most basic approach consists of distributing dipoles over a predefined volumetric grid similar to the ones used in scanning approaches. However, since primary sources are essentially restricted to cortex, the image can be plausibly constrained to sources lying on the cortical surface, as extracted from an anatomical MR images of the subject [22]. Following segmentation of the MR volume, dipolar sources are placed at each node of a triangular tessellation of the surface of the cortical mantle. Since the pyramidal cells that produce the measured fields are oriented normal to the surface, we can further constrain each of these elemental dipolar sources to be normal to the surface. The highly convoluted nature of the human cortex requires that a high-resolution representation contains of the order of ten to one hundred thousand dipole "pixels". The inverse problem is therefore hugely under-determined and imaging requires the use of either explicit or implicit constraints on the expected current source distributions. Typically,

this has been accomplished through the use of regularization or Bayesian image estimation methods.

Bayesian formulation

Bayesian approach to neuronmagnetic inverse problem was first introduced by Clarke in 1989 [14]. In the Bayesian formalism, the neuromagnetic inverse problem is defined as the problem of estimating the matrix $\mathbf{J}$ of dipole amplitudes at each tessellation element from the spatio-temporal data matrix $\mathbf{B}$, which are related in the noiseless case by $\mathbf{B} = \mathbf{GJ}$. The i-th row of $\mathbf{J}$ contains the amplitude image across the cortex at time i. From Bayes theorem, the posterior probability $p(\mathbf{J}|\mathbf{B})$ for the amplitude matrix $\mathbf{J}$ conditioned on the data $\mathbf{B}$ is given by

$$p(\mathbf{J}|\mathbf{B}) = \frac{p(\mathbf{B}|\mathbf{J})p(\mathbf{J})}{p(\mathbf{B})}, \tag{34}$$

where $p(\mathbf{B}|\mathbf{J})$ gives the forward probability density of getting magnetic field $\mathbf{B}$ conditioned on $\mathbf{J}$. $p(\mathbf{J})$ is a prior distribution reflecting our knowledge of the statistical properties of the unknown image. While Bayesian inference offers the potential for a full statistical characterization of the sources through the posterior probability, images are typically estimated in practice by maximization of the posterior or log-posterior probability.

The estimation of $\mathbf{J}$ in the *maximum a posteriori* (MAP) sense is given by

$$\hat{\mathbf{J}}_{MAP} = \arg\max_{\mathbf{J}} p(\mathbf{B}|\mathbf{J})p(\mathbf{J}). \tag{35}$$

The log-likelihood of (35) is given by

$$\hat{\mathbf{J}}_{MAP} = \arg\max_{\mathbf{J}} (log[p(\mathbf{B}|\mathbf{J})] + log[p(\mathbf{J})]). \tag{36}$$

Typically, MEG and EEG data are assumed to be corrupted with additive Gaussian noise that we assume here to be spatially identically distributed over all sensors (generalization is straightforward). The log-likelihood is then simply given, within a constant, by

$$ln[p(\mathbf{B}|\mathbf{J})] = -\frac{1}{\sqrt{2\sigma^2}}||\mathbf{B} - \mathbf{GJ}||_F^2. \tag{37}$$

The prior is a probabilistic model that describes our expectations concerning the statistical properties of the source for which we will assume an exponential density

$$p(\mathbf{J}) = \frac{1}{z} exp[-\beta f(\mathbf{J})], \tag{38}$$

where z and β and $f(\mathbf{J})$ depends on the image $\mathbf{J}$. This form encompasses both multivariate Gaussian models and the class of Gibbs distributions or Markov random field models [13]. Combining the log-likelihood and log-prior gives the general form of the negative log-posterior whose minimization yields the maximum a posteriori estimate:

$$\hat{\mathbf{J}}_{MAP} = \arg\min_{\mathbf{J}} ||\mathbf{B} - \mathbf{GJ}||_F^2 + \lambda f(\mathbf{J}), \tag{39}$$

where $\lambda = 2\beta\sigma^2$. λ is the regularization parameter. The parameter λ should be considered as a regularization parameter tuning between the prior $f(\mathbf{J})$ and fit to the data. If $\lambda = 0$ estimation of the current distribution becomes simply least squares. This type of solution to the inverse problems was introduced by Tikhonov in [97].

Choice of the regularization parameter λ

There are many approaches to estimate the value of λ. We summarize a few as explained below:

1.**L-Curve**: When plotted on a log-log scale, the parametric curve of optimal values of $||\mathbf{W}||$ and data fit $||\mathbf{B} - \mathbf{GJ}||$ often takes on an L shape. For this reason, the curve is called an L-curve [45]. The value of λ in the L-curve criterion is the value of λ that gives the solution closest to the corner of the L-curve, as shown in Figure 13.

2. **Generalized cross validation (GCV)** is an alternative method for estimating the regularization parameter λ [107], that has a number of desirable statistical properties. Consider

$$f(\lambda) = \frac{||\mathbf{B} - \mathbf{GJ}||}{Trace(\mathbf{I} - \mathbf{GG}^{\dagger})} = \frac{V(\lambda)}{T(\lambda)} \tag{40}$$

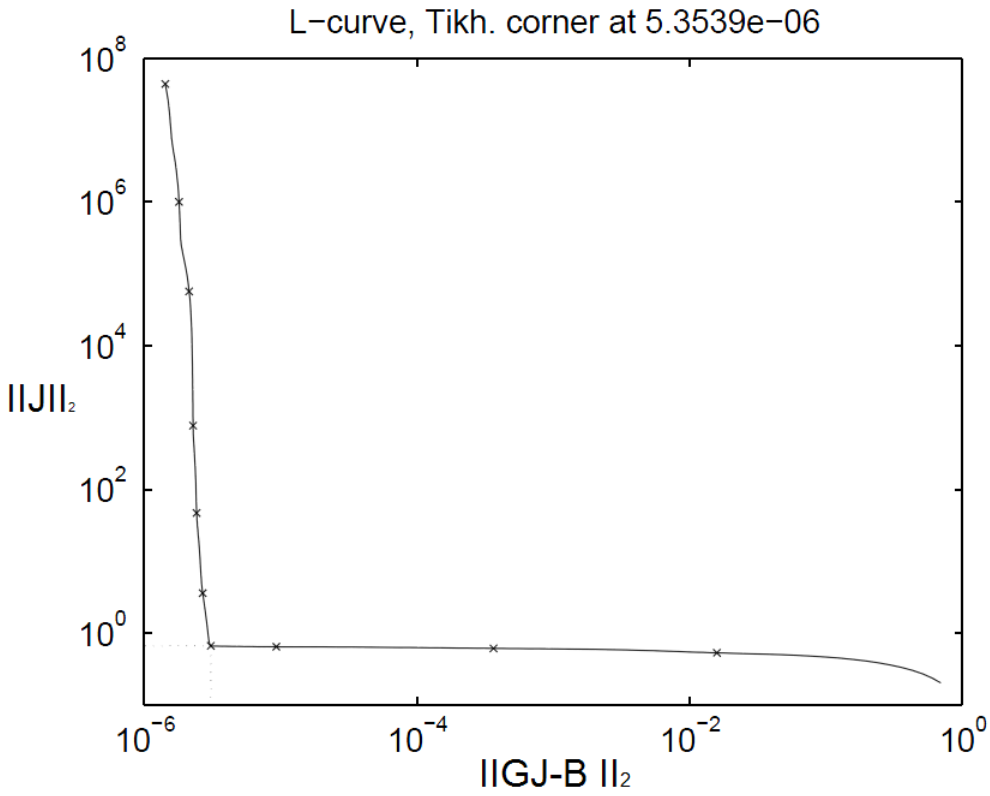

Figure 13: Typical L-curve for classic shaw inverse problem.

The numerator in (14) is the data misfit in the least squares sense and the dominator measures the closeness of the data resolution matrix to the identity matrix. In the GCV method, we pick the value of λ that minimizes (14), as shown in Figure 14.

Linear estimators

The simplest approach to (39) is to consider prior distribution of source ammplitudes $\mathbf{J}$ to be Gaussian with zero mean. Introduce

$$f(\mathbf{J}) = tr[\mathbf{J}\mathbf{C}_J^{-1}\mathbf{J}^t], \tag{41}$$

where $\mathbf{C}_J^{-1}$ is the inverse covariance matrix of sources. If we break this inverse matrix as, $\mathbf{C}_J^{-1} = \mathbf{W}\mathbf{W}^t$, then (39) can be written in the following manner:

$$\hat{\mathbf{J}}_{MAP} = \arg\min_{\mathbf{J}} ||\mathbf{B} - \mathbf{G}\mathbf{J}||_F^2 + \lambda^2 ||\mathbf{W}\mathbf{J}||_F^2. \tag{42}$$

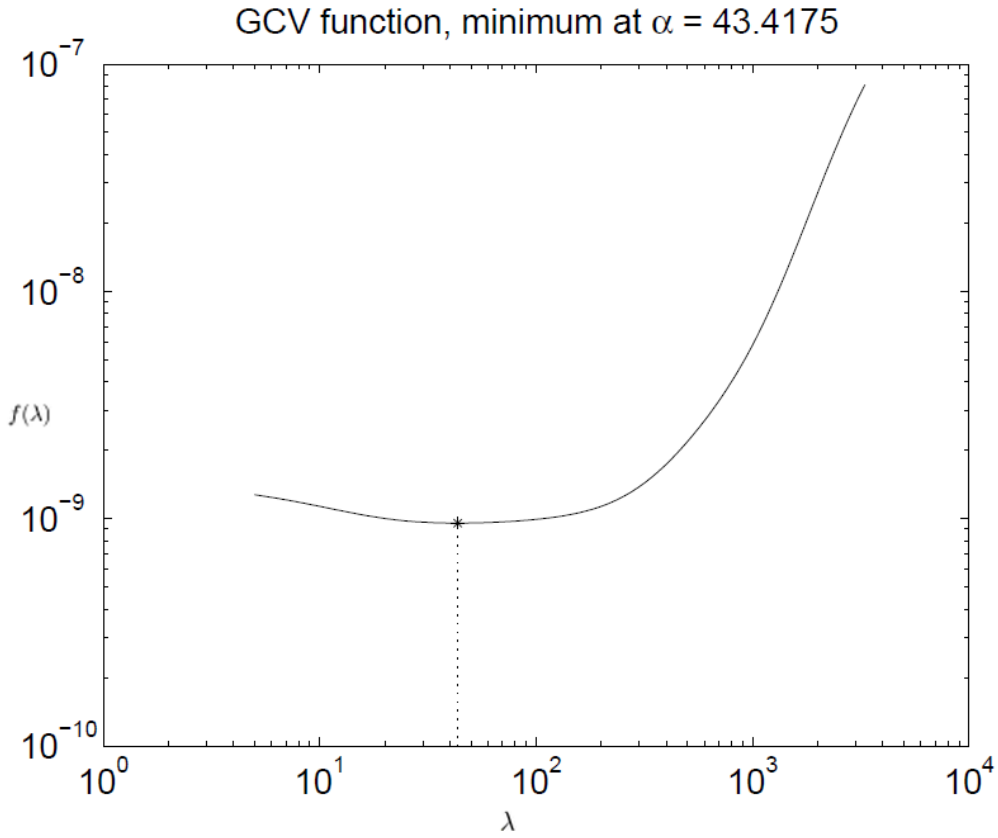

Figure 14: Typical GCV-curve for classic shaw inverse problem.

The MAP estimator now takes the following simple linear form:

$$\hat{\mathbf{J}}^t_{MAP} = \mathbf{W}\mathbf{W}^t\mathbf{G}^t(\mathbf{G}\mathbf{W}\mathbf{W}^t\mathbf{G}^t + \lambda\mathbf{I})^{-1}\mathbf{B}. \tag{43}$$

In this case, $\hat{\mathbf{J}}_{MAP}$ also follows a Gaussian distribution. (39) is normally known as zeroth order Tikhonov regularized solution of $\mathbf{J}$ [97, 26], where the regularization parameter λ can be estimated from any of the techniques explained in the previous section.

Properties of the source covariance matrix

Source covariance is the last parameter of the model which will condition the final form taken by (42). The forms of source covariance matrices that are most commonly used in MEG are:

1. The identity matrix, which yields classical minimum-norm estimators [97]. The major assumption in using the identity matrix is that source amplitudes J are independent and identically distributed.

   In Figure 15, a comparison is shown between LCMV beamformer and the minimum-norm solution to the inverse problem, showing that though the minimum-norm solution is widespread, the peak of maximum intensity is in the right place in this median nerve stimulation experiment, where we expect activity within primary somatosensory areas.

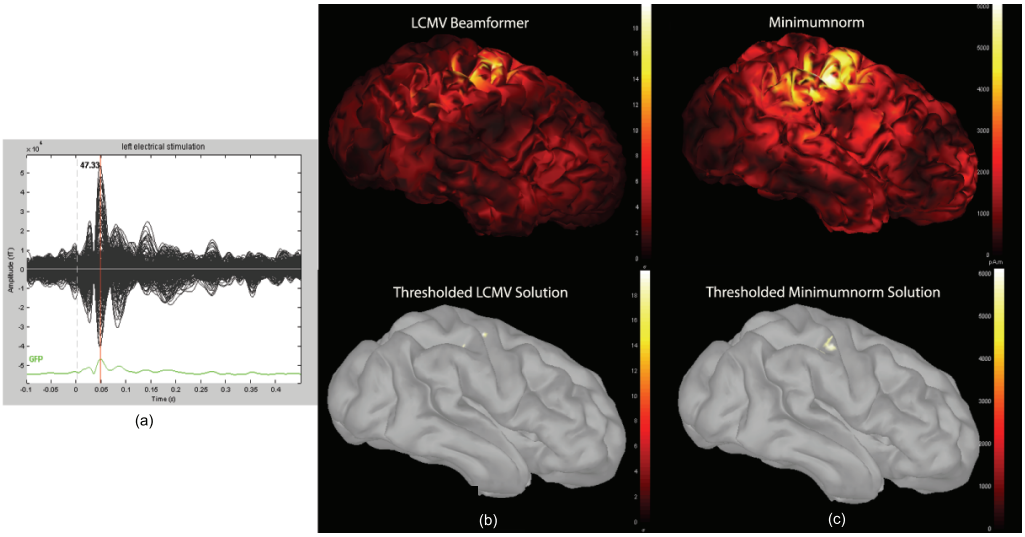

Figure 15: Comparison of LCMV and minimum norm.

2. A diagonal matrix whose elements are given by the norm of the elements of the corresponding column in the lead-field matrix (*i.e.*, $\mathbf{W}_{ii} = ||\mathbf{g}_i||^2$ with $\mathbf{g}_i$ the i^{th} column of $\mathbf{G}$). This solution is a forward-field normalized solution.

3. $\mathbf{W}$ which is based on the relationship between source neighbors [108]. The matrix $\mathbf{W}$ is given by

$$\mathbf{W}_{ij} = \begin{cases} 1 & \text{if } i = j, \\ -\frac{1}{n} & \text{if } j \in \mathcal{N}(i), \\ 0 & \text{otherwise,} \end{cases}$$

where $\mathcal{N}(i)$ defines the first order neighbor of i^{th} source and $n = \mathcal{C}ard[\mathcal{N}(i)]$.

4. **W** is diagonal with elements equal to some estimate of the source power at that location, which may be computed from the output of a beamformer or MUSIC scan evaluated for each dipole pixel [69] or weighted from other functional imaging modalities such as fMRI, PET, or SPECT [64, 21].

These methods have the advantage to be fast and overall robust towards noise [106]. They provide estimates where the center of gravity of the activity is very close to the true source. However, results are often very smooth spatially and do not allow for estimation of the spatial extent of the activity. This problem of spatial extent and its solution will be addressed in details in Chapter 2.

Nonlinear estimators of source amplitudes

It is possible to obtain sparser image estimates of the current distribution by using alternative (non-quadratic) cost functions $f(\mathbf{J})$ in (39). Norms and semi-norms on source amplitude priors with values $p \leq 2$ in (42) have been investigated. Solutions will become increasingly sparse as p is reduced. For the special case of $p = 1$, the problem can be slightly modified to be recast as a linear program. This is achieved by replacing the quadratic log-likelihood term with a set of under-determined linear inequality constraints, where the inequalities reflect expected mismatches in the fit to the data due to noise. The l^1-cost can then be minimized over these constraints using a linear simplex algorithm. Properties of linear programming problems guarantee that there exists an optimal solution for which the number of non-zero pixels does not exceed the number of constraints, or equivalently the number of measurements. Since the number of pixels far outweighs the number of measurements, the solutions are therefore guaranteed to be sparse. This idea can be taken even further by using the quasi-norm for values of $p < 1$. In this case, it is possible to show that there exists a value $0 < p < 1$ for which the resulting solution is maximally sparse [4, 34].

Another approach defined cliquish relationships between neighborhood sources. The whole network of sources may be described as distributed within a Markov Random Field (MRF), this relationship was exploited in [5, 84]. A key property of MRFs is that their joint statistical distribution can be constructed from a set of potential functions defined on a local neighborhood system [83]. Thus, the energy function $f(\mathbf{J})$ for the prior can be expressed as

$$f(\mathbf{J}) = L\sum_{i=1}^{N}[\alpha_i J(i) + \gamma_i[\sum_{j\in\mathcal{N}(i)}(J(i)-J(j))^2]^Q] \tag{44}$$

where L is the number of time samples, α_i and γ_i determines the weighting factors between neighborhood sources. Q is the index of the amplitude of the neighborhood group. $\mathcal{N}(i)$ neighborhood of the source i is defined as the 9 closest neighbors to the source. The first term in equation (44) expresses sparsity while the second one favors focal sources distributions.

The MRF-based image priors lead to non-convex [5] and integer [83] programming problems in computing the MAP estimate. Computational costs can be very high for these methods since although the priors have computationally attractive neighborhood structures, the posteriors become fully coupled through the likelihood term. Furthermore, to deal with non-convexity and integer programming issues, some form of deterministic or stochastic annealing algorithms must be used [35].

Conclusion

The excellent time resolution of MEG provides us a unique window on the dynamics of human brain functions. Though the limited spatial resolution remains the problem for this modality, adequate modeling and modern signal processing methods prove MEG as a dependable functional imaging modality. Potential advances in forward modeling include better characterization of the skull, scalp and brain tissues from MRI and in vivo estimation of the inhomogeneous and anisotropic conductivity properties of the head. Progress in inverse methods include meth-

ods for combining MEG with other functional modalities and exploiting signal analysis methodologies to better localize the brain activity.

Part 2

MEG SOURCE IMAGING

Multipolar Cortical Remapping

Introduction

The equivalent current dipole model is directly interpretable as a current element restricted to the cortical surface representing a point source. However, one of the perceived key limitations of this model is that, distributed sources may not be adequately represented. This problem was one of the prime motivations to the development of imaging approaches. An alternative solution is to remain within the model-based framework but to broaden the model to allow parametric representations of distributed sources. The multipolar expansion provides a natural framework for generating these models [79, 36]. Multipolar expansions are derived from spherical harmonics of the magnetic scalar potential. If the expansion point is chosen near the center of a distributed source, then the contribution of higher-order terms will drop off rapidly as the distance from sources to the sensors increases. Using this framework we expand the set of sources to include current dipoles and first-order current multipoles. These sources are able to represent the field from a distributed source more accurately than by current dipole model, though still benefiting from a compact, low-dimensional form [78]. Multipolar expansions of magnetic scalar potentials originate from general spherical harmonics solution of the Poisson equation.

In this thesis, we proposed an approach for estimating the spatial extent of cortical current sources using a hybrid methodology called Multipole Cortical Remapping (MCR). It takes the best of imaging and parametric approaches as

explained in the previous chapter.

We will first detail the spherical harmonic expansions of scalar potentials, then introduce a general treatment of the spherical harmonic multipole expansion. This will be followed by the multipolar expansion of distributed dipole sources. These treatments are adapted from the classic paper by Wikswo et al. [111]. We will then proceed to the more specific treatment of magnetic scalar potentials in terms of current multipolar moments.

Finally, following this theoretical background, the Multipolar Cortical Remapping (MCR) method will be introduced, followed by results on simulated and experimental MEG data.

Multipolar expansions of a scalar potential

A vector field with zero curl, termed conservative or irrotational, can be described as the negative gradient of a scalar potential $V_m(r)$ which satisfies the Poisson equation:

$$\nabla^2 V_m(r) = -s(r'), \tag{45}$$

where $s(r')$ describes the source distribution producing the scalar field V_m. The solution to (45) is known to have the following form:

$$V_m(r) = \frac{1}{4\pi} \int \frac{s(r')}{r - r'} d^3 r', \tag{46}$$

where the integral must be evaluated over the region where $s(r')$ is non zero. If the source distribution is bounded by a closed surface S, then a scalar potential can be described by Laplace equation:

$$\nabla^2 V_m(r) = 0, r \text{ outside of } S. \tag{47}$$

Spherical multipolar expansions

Spherical multipolar expansion for a harmonic scalar potential, *i.e.*,satisfying (47), can be written in odd and even unit potentials, $V^e_{mn}(r)$ and $V^o_{mn}(r)$, with their

multipole strengths a_{mn} and b_{mn} respectively,

$$V_m(r) = \sum_{n=o}^{\infty}\sum_{m=o}^{\infty}[a_{nm}V_{mn}^e(r)+b_{mn}V_{mn}^o(r)],\ r > a,\ \text{outside the volume of the conductor,} \tag{48}$$

where

$$V_{mn}^e(r) = \frac{1}{4\pi}r(-n-1)Y_{mn}^e(\theta,\phi), \tag{49}$$

$$V_{mn}^o(r) = \frac{1}{4\pi}r(-n-1)Y_{mn}^o(\theta,\phi) \tag{50}$$

are the unit potentials for the even and odd nm-th multipoles respectively, a is the radius of the sphere, and θ and ϕ are azimuth and elevation angles, respectively. The even and odd spherical harmonics with $P_n^m(cos\theta)$ being the associated Legendre function of the first kind are given by

$$Y_{mn}^e(\theta,\phi) = \cos(m\phi)P_n^m(cos\theta), \tag{51}$$

$$Y_{mn}^o(\theta,\phi) = \sin(m\phi)P_n^m(cos\theta)\, m \neq 0\,,\ m \leq n. \tag{52}$$

The first term V_{00}^e corresponds to the monopole ($n = 0$), There are three dipole ($n = 1$) components, V_{10}^e, V_{11}^e, V_{10}^o and five quadruple ($n = 2$) components, V_{20}^e, V_{21}^e, V_{21}^o, V_{22}^e, V_{22}^o and the n-th order multipole has $2n+1$ components. The multipole strengths are given by

$$a_{mn} = \epsilon_m\frac{(n-m)!}{(n+m)!}\int_0^{2\pi} cos(m\phi')d\phi' \int_0^{\pi} P_n^m(cos\theta')sin(\theta')d\theta' \int_0^a s(r')r'^{(n+2)}dr' \tag{53}$$

$$b_{mn} = \epsilon_m\frac{(n-m)!}{(n+m)!}\int_0^{2\pi} sin(m\phi')d\phi' \int_0^{\pi} P_n^m(cos\theta')sin(\theta')d\theta' \int_0^a s(r')r'^{(n+2)}dr', \tag{54}$$

where ϵ_m is the Neumann factor

$$\epsilon_m = 1\ for\ m = 0,$$

$$\epsilon_m = 2\ for\ m \neq 0. \tag{55}$$

The illustration of spherical harmonic multipole components are shown in Figure 16.

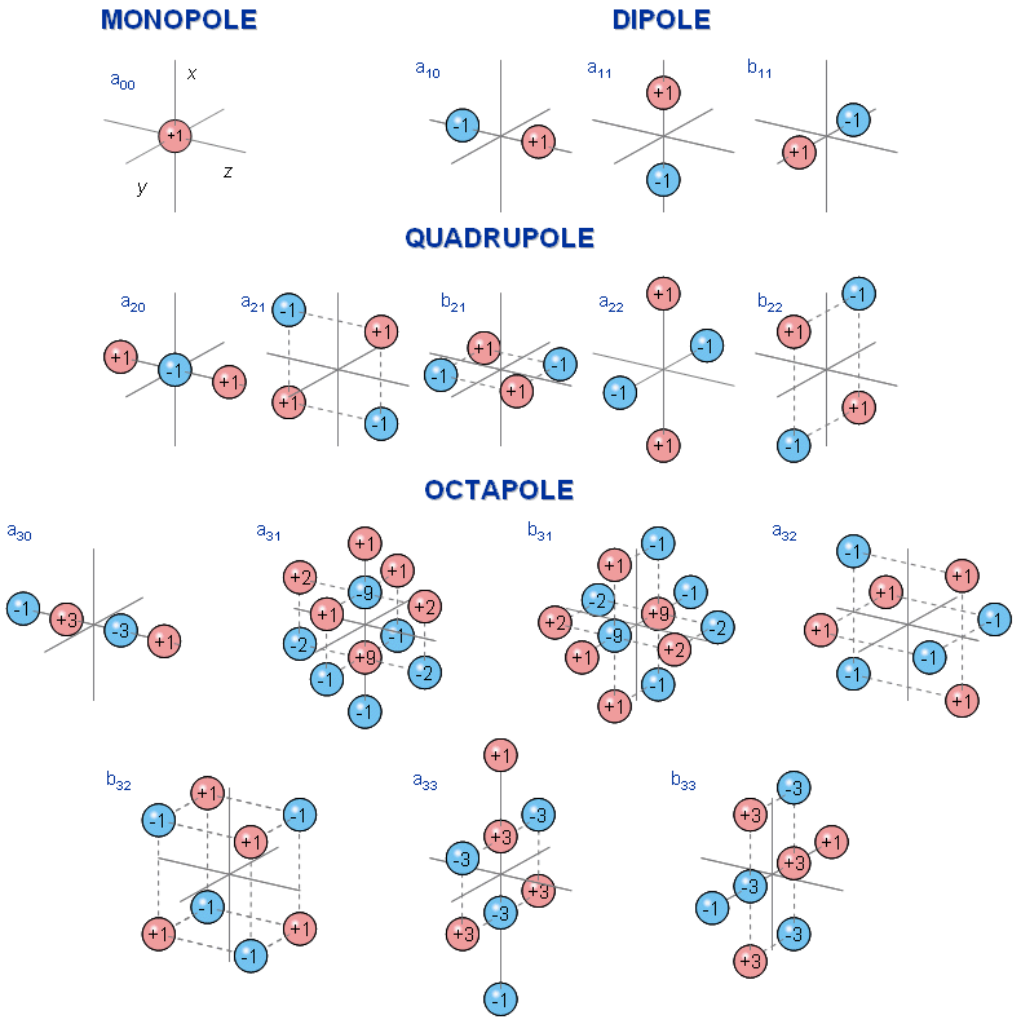

Figure 16: Source-sink illustration of spherical harmonic multipole components, adapted from [110, 67]. The figure shows the physical source-sink configurations corresponding to the multipole components of the dipole (three components), quadrupole (five components), and octupole (seven components).

Multipole expansions of a distributed dipole source

If the current distribution consists of a set $\mathcal{D}$ of n elementary current dipoles $\mathcal{D} = \{\mathbf{d}_i, i \leq n\}$, then it is straightforward to relate it its multipolar expansion [111]. The equations below provide the dipole to quadrupole moments for a single dipole $q\,(q_x, q_y, q_z)$ at the point (x_o, y_o, z_o).

Dipole

$$a_{10} = q_z \tag{56}$$

$$a_{11} = q_x \tag{57}$$

$$b_{11} = q_y \tag{58}$$

quadrupole

$$a_{20} = 2z_o q_z - x_o q_x - y_o q_y \tag{59}$$

$$a_{21} = z_o q_x + x_o q_z \tag{60}$$

$$b_{21} = z_o q_y + y_o q_z \tag{61}$$

$$a_{22} = \frac{1}{2}(x_o q_x - y_o q_y) \tag{62}$$

$$b_{22} = \frac{1}{2}(x_o q_y - y_o q_x) \tag{63}$$

For example consider a simple current distribution consisting of two dipole, as shown in Figure 17, such that

$$\mathbf{q_a} = (q_x, q_y, q_z) \; at \; \mathbf{r_a} = (x_o, y_o, z_o) \tag{64}$$

$$\mathbf{q_b} = (q_x, q_y, q_z) \; at \; \mathbf{r_b} = (x_o, y_o, z_o) \tag{65}$$

The spherical harmonic multipole expansion for each dipole can be determined using equations (56) to (63). The multipole expansion for this current distribution is the sum of these two expansions and given:

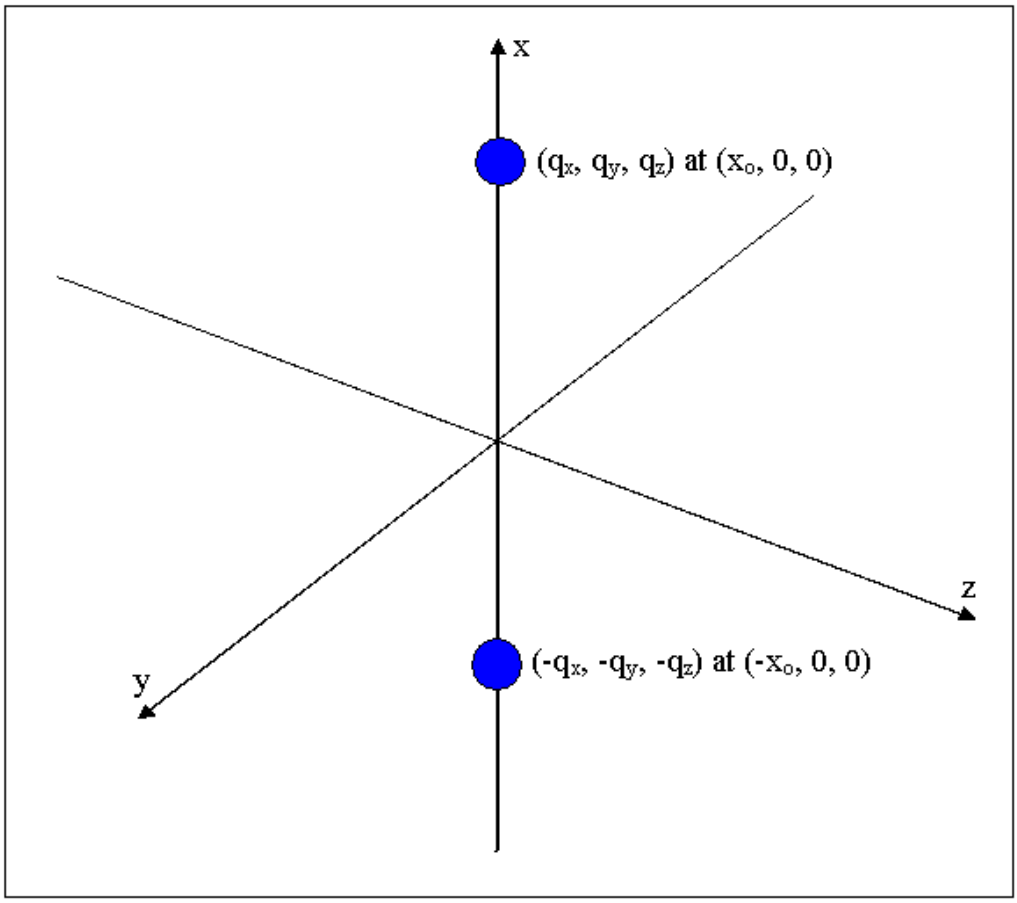

Figure 17: Distributed dipole model.

$$
\begin{aligned}
a_{10} = a_{11} = b_{11} &= 0 \\
a_{20} &= -2x_o q_x \\
a_{21} &= -2x_o q_z \\
b_{21} &= 0 \\
a_{22} &= x_o q_x \\
b_{22} &= x_o q_y
\end{aligned}
\tag{66}
$$

Equation (66) has an important implication. Two opposed dipoles on opposite sides of the origin produce a field that has no dipole moments. This kind of current distribution can only be captured using a quadrupole model.

Multipole moments of current distributions

The neural current distribution is zero outside the head. Thus the magnetic field $\mathbf{B}$ can be represented as the negative gradient of a magnetic scalar potential V_m [43, 37, 52]:

$$\mathbf{B}(\mathbf{r}) = -\mu_o \nabla V_m(r), r \text{ outside the head.} \tag{67}$$

By taking the divergence of (67), V_m satisfies the following Laplace equation:

$$\nabla^2 V_m(r) = 0. \tag{68}$$

The solution of (68), *i.e.*, the magnetic scalar potential caused by a localized current distribution, was stated by Bronzan in [11] as follows:

$$V_m(r) = \frac{1}{4\pi} \int \frac{\mathbf{J}(\mathbf{r}') \cdot \mathbf{r} \times \mathbf{r}'}{|\mathbf{r} - \mathbf{r}'|(\mathbf{r}|\mathbf{r} - \mathbf{r}'| + \mathbf{r^2} - \mathbf{r} \cdot \mathbf{r}')} d^3 r', \tag{69}$$

where $\mathbf{r}'$ is the local point at which current distribution is present and $\mathbf{r}$ is a field point at which the magnetic field is measured. As noted by Bronzan, (69) is valid for any arbitrary coordinate system and localized source, where the observation point r is outside the source and does not lie on a line between the origin and the source (see Figure 18). Therefore, if we place the origin inside the source body, these equations hold for all points outside of the body.

As in previous chapter, a convenient substitution in MEG is to divide the current density into primary current density $\mathbf{J^p}(\mathbf{r}')$ and a volume current $\mathbf{J^v}(\mathbf{r}')$ as follows:

$$\mathbf{J}(\mathbf{r}') = \mathbf{J^p}(\mathbf{r}') + \mathbf{J^v}(\mathbf{r}'). \tag{70}$$

Suppose that the head consists of spherically symmetric regions of homogeneous conductivity, which means that all surfaces are radial and therefore the contribution from volume current vanishes. The magnetic scalar potential outside a spherical symmetric volume conductor is given by

$$V_m(r) = \frac{1}{4\pi} \int \frac{\mathbf{r} \times \mathbf{r}'}{F(r, r')} \cdot \mathbf{J^p}(\mathbf{r}') d^3 r'. \tag{71}$$

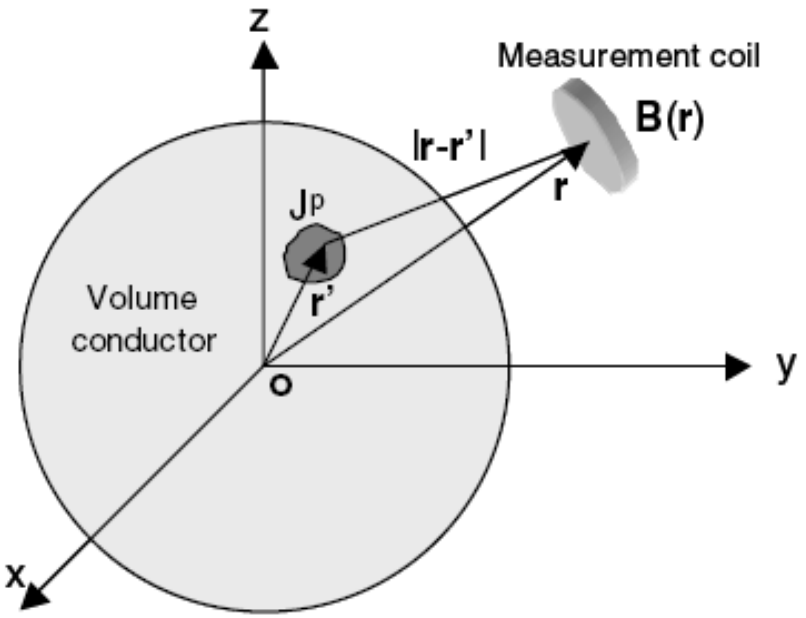

Figure 18: MEG sensor measure the magnetic field caused by local current distribution $J(r')$ (adapted from [53]).

Equation (71) can also be represented using a multipole expansion [54]. A multipole expansion is the series expansion of the field produced by the source in which successive terms decrease in amplitude. An important factor to consider is the expansion point for this multipole series. In most of the available literature, multipole expansions are presented as expansions about the origin of the coordinate system. Since it is advantageous to expand the field about the centroid of the source, which is not necessarily at the origin of a fixed coordinate system, some authors (*e.g.*, [79]) use a coordinate system with a variable origin. Here, we will explicitly give the equations for the general case of a multipole expansion about an arbitrary location $\mathbf{l}$ for a fixed coordinate system.

The magnetic scalar potential for a spherical head model (extension to a realistic head model is straightforward [76]) in terms of multipole moments (with respect to an arbitrary expansion point $\mathbf{l}$) can be expressed as follows (for more details see [54]):

$$V_m(r) = \frac{1}{4\pi}\sum_{n=0}^{\infty}\nabla_l^n\left(\frac{\mathbf{r}\times\mathbf{l}}{F(r,l)}\right)\|\mathbf{\Omega^n}, \tag{72}$$

where $F(r,l) = |r-l|(r|r-l| + r^2 - \mathbf{l}\cdot\mathbf{r})$ is a scalar function. Here, $\mathbf{r}'$ is the local point at which the current distribution is present and $\mathbf{r}$ is the field point at which the magnetic field is measured.

The double vertical in (72) represents an n-fold contraction between the two polyads ∇_l^n(the nth consecutive derivative w.r.t $\mathbf{l}$) and $\mathbf{\Omega^n}$ the nth order multipole moment of the neural current distribution [54]. $\mathbf{\Omega^n}$ completely describes the spatial characteristics of the current distribution and is defined by

$$\mathbf{\Omega^n} = \frac{1}{n!}\int (r'-l)^n\mathbf{J}(\mathbf{r}')dr', \tag{73}$$

where $\mathbf{J}(\mathbf{r}')$ represents the primary current producing a magnetic field outside the volume conductor.

The magnitude of the successive terms of the multipole expansion decreases, hence our study will be limited to orders 0 (dipoles) and 1 (quadrupoles), for practical SNR considerations. The first-order approximation of the magnetic scalar potential defined by (72) is stated as

$$V_m(r) = \frac{1}{4\pi}\left[\left(\frac{\mathbf{r}\times\mathbf{l}}{F(r,l)}\right)\cdot\mathbf{D} + \nabla_l\left(\frac{\mathbf{r}\times\mathbf{l}}{F(r,l)}\right):\mathbf{Q}\right], \tag{74}$$

where $\mathbf{D} = \int\mathbf{J}(\mathbf{r}')dr'$ is the current dipole moment and $\mathbf{Q} = \int(r'-l)\mathbf{J}(\mathbf{r}')dr'$ is the current quadruple moment.

Dipole and quadrupole moments depend on the spatial distribution of currents [111]. First-order approximation of the magnetic field produced by the neural current distribution is given by

$$B(r) = -\frac{\mu_o}{4\pi}\left(\nabla\left(\frac{\mathbf{r}\times\mathbf{l}}{F(r,l)}\right)\cdot\mathbf{D} + \nabla_l\left[\nabla\left(\frac{\mathbf{r}\times\mathbf{l}}{F(r,l)}\right)\right]:\mathbf{Q}\right). \tag{75}$$

Multipolar cortical remapping

Multipole Cortical Remapping (MCR) is an hybrid method that takes the best of imaging and parametric approaches to the MEG inverse problem. Preliminary results for this technique were presented in [56, 57].

In MCR we first use an imaging approach and estimate the zero-order Tikhonov regularized image of the current distribution on the cortex. We then threshold this image using histogram-based thresholding principles. This thresholded image is then converted into groups of activity using a labeling algorithm, [46] depending upon their spatial connectivity. We then estimate multipole moments at the gravity center for each group. The multipole moments are not directly related to the actual physiological processes that produce the MEG signals, so we describe a remapping technique to map these moments back onto the cortex using a Bayesian formalism.

One of the main advantages of MCR is the use of a Tikhonov regularization for the estimation of multipole moments and cortical remapping by matching the multipole moments (only eight moments) of the original parametric source and the equivalent cortical patch, rather than their forward fields. Hence we achieve a significant reduction in the computational complexity of the inverse problem. Most importantly, we introduce physiological priors in the moment matching criterion.

We will present the performance of MCR by its application on simulated single and two source scenarios. The robustness of the method against thresholding value will also be presented. We will also present the results of the application of MCR on somatosensory data using stimulation of four fingers from the right hand.

MCR takes advantage of both the compact parametric modeling of distributed currents using equivalent current multipoles (ECM) and sparse-focal image models on restricted spatial supports. It yields a workable estimation of the surface extent of regional brain activations. The MCR proceeds as follows: first, parametric modeling of cortical currents is obtained by fitting a series of compact equivalent current multipole (ECM) model elements to a low-resolution regularized image of the cortically-constrained current distribution. The second step consists in efficiently adjusting a sparse-focal image model to each ECM element using a maximum a posteriori (MAP) Bayesian estimation framework. Hence the ECM decomposition acts as an intermediary between two image models of

cortical currents, for the sake of considerable reduction in the dimensions of the parameter subspaces.

Compact parametric decomposition of cortical currents

The motivation is to reduce the dimension of the subspace in which a sparse focal image model may be fitted to the data. One approach could consist in directly adjusting equivalent current dipole (ECD) or ECM models to the data. The nonlinear search for their optimal locations though has proven to be hardly tractable in practice without strong priors on the number and the expected loci of activations when multiple regions are simultaneously active.

Here the decomposition of cortical currents in a compact form using ECM model elements relays a smooth, low-resolution image model of neural currents to their final higher-resolution sparse-focal estimate in a two-step procedure.

The basic image support consists of a set $\mathcal{D}$ of n elementary current dipoles $\mathcal{D} = \{\mathbf{d}_i, i \leq n\}$, densely distributed over the MRI-extracted cortex of the subject that forms a surface manifold Γ of $\mathbf{R}^3$. The orientations $\mathbf{o}_i$ of all the dipoles follow the circumvolutions of the cortical mantle. Hence the estimation of cortical currents reduces to that of their amplitude distribution $\mathbf{y} = \{y_i, i \leq n\}$.

The low-resolution image model was obtained from the Tikhonov-regularized weighted minimum-norm estimator (WMNE) [2]:

$$\overline{\mathbf{y}} = \arg\min_{\mathbf{y}}\{\|\mathbf{b} - \mathbf{G}\mathbf{y}\|^2 + \lambda \mathbf{y}^{\mathbf{t}}\mathbf{C}^{-\mathbf{1}}\mathbf{y}\}, \tag{76}$$

where $\mathbf{b}$ is a vector of m instantaneous measurements on the MEG sensor array; $\mathbf{G}$ is the corresponding forward gain matrix and $\mathbf{C}$ is the expected covariance matrix of the elementary sources; λ is a scalar regularization parameter.

The solution to (76) is unique and takes the following form:

$$\overline{\mathbf{y}} = \mathbf{G}^{\mathbf{t}}(\mathbf{G}\mathbf{G}^{\mathbf{t}} + \lambda \mathbf{I})^{-\mathbf{1}}\mathbf{b}, \tag{77}$$

where $\mathbf{G^t}$ denotes the transposed $\mathbf{G}$ matrix and we have assumed that $\mathbf{C} = \mathbf{I}$, without loss of generality. Note that $\overline{\mathbf{y}}$ may either be estimated at a single time instant or over a larger time frame with no difference in the approach.

The low-resolution image model $\overline{\mathbf{y}}$ was thresholded using for instance an absolute amplitude criterion based on the analysis of the histogram of the $|y_i|$'s. Dipole elements in $\mathcal{D}$ with absolute amplitude under the 85^{th} percentile of the histogram were set to zero. The remaining set of *active* elementary dipoles was arranged in a set of n_C spatially-contiguous dipole clusters $\{\mathcal{C}_j, j \leq n_C\}$ [46].

Let $\mathbf{x_i}$ be the coordinates of dipole $\mathbf{d}_i$ in $\mathbf{R}^3$. We define as $\mathbf{X}_j$, the current-weighted centroid of cluster $\mathcal{C}_j$, that is,

$$\mathbf{X}_j = \sum_{i, \mathbf{d}_i \subset \mathcal{C}_j} |y_i| \mathbf{x}_i.$$

$\mathbf{X}_j$ serves as the expansion point of the ECM model $\mathbf{m}_{\mathcal{C}_j}$ – up to the quadrupole – of the currents sustained by cluster $\mathcal{C}_j$. All the ECM moments from all clusters are gathered in $\mathbf{m}_{\mathcal{C}}$ and are adjusted in the least-squares sense:

$$\mathbf{m}_{\mathcal{C}} = \mathbf{G}_{\mathbf{m}}^{\mathbf{t}} (\mathbf{G}_{\mathbf{m}} \mathbf{G}_{\mathbf{m}}^{\mathbf{t}})^{-\mathbf{1}} \mathbf{b}, \tag{78}$$

where $\mathbf{G_m}$ is the ECM gain matrix of all the $\mathcal{C}_j$ $(j \leq n_c)$ clusters, which computation is detailed in [54].

Sparse-focal imaging model

The second step in the MCR procedure consists of estimating an equivalent cortical current distribution to each of the ECM elements $\mathbf{m}_{\mathcal{C}_j}$ using explicit sparse-focal priors.

The quadrupolar ECM expansion $\mathbf{m_i} \in \mathbf{R}^8$ of any dipole $\mathbf{d}_i \subset \mathcal{C}_j$ about

$\mathbf{X}_i = [X_{i,1}, X_{i,2}, X_{i,3}] \in \mathbf{R}^3$, as introduced in Section writes [111]:

$$\mathbf{m_i} = \begin{bmatrix} 1 & 0 & 0 \\ 0 & 1 & 0 \\ 0 & 0 & 1 \\ -X_{i,1} & -X_{i,2} & 2X_{i,3} \\ X_{i,3} & 1 & X_{i,1} \\ 0 & X_{i,3} & X_{i,2} \\ .5X_{i,1} & -.5X_{i,2} & 0 \\ .5X_{i,2} & .5X_{i,1} & 0 \end{bmatrix} \mathbf{o_i} \cdot y_i = \mathbf{g_i^m} y_i. \tag{79}$$

The equivalent sparse-focal image model of each $\mathbf{m}_{\mathcal{C}_j}$ defined in Section consists of a subset of cortical dipoles $\zeta_j \subset \mathcal{D}$ which amplitudes $\overline{\overline{\mathbf{y}}}_j$ verify

$$\mathbf{m}_{\mathcal{C}_j} = \sum_{i, \mathbf{d}_i \in \zeta_j} \mathbf{g_i^m} \overline{\overline{y}}_i + \mathbf{n} = \mathbf{G}_j^m \overline{\overline{\mathbf{y}}}_j + \mathbf{n}, \tag{80}$$

where $\mathbf{M}_j^\zeta$ is the equivalent cortical ECM moments and $\mathbf{n}$ is the residuals between the ECM element $\mathbf{m}_{\mathcal{C}_j}$ and its cortically-distributed counterpart.

We are able to estimate $\mathbf{y}$ as follows

$$\hat{\mathbf{y}} = \arg\min_{\mathbf{y}} \{ \|\mathbf{J_o} - \mathbf{J}_\zeta \mathbf{y}\| + \lambda \|\mathbf{y}\| \}. \tag{81}$$

Studies of functional activation, such as somatosensory mapping using PET and fMRI, reveal the sparse and focalized nature of the activation of neural currents. Our prior is therefore specifically designed to reflect the expectation that the current sources tend to a sparse and focal representation. $\overline{\overline{\mathbf{y}}}$ is estimated using explicit sparse-focal priors, which can readily be inscribed in a Bayesian MAP estimator of cortical current amplitudes exemplified in [84]. This has been demonstrated for instance in the context of Markovian Random Field (MRF) models of the cortical current distribution. Here, we revisit this approach and make it tractable by running MAP estimates restricted to the local current distributions about each ECM element and by matching their respective multipolar moments. This latter point further reduces the dimension of the quantities under consideration as we are interested in adjusting moments in a subspace of dimension 8

rather than in the subspace of MEG sensors which is $m \sim 100$. The cortical current density is modeled as a random process using extensions of the models described in [84]. We characterize the current density $\overline{\overline{y}}_i$ at every vertex through the association of a continuous, normally-distributed, random variable of dipole amplitude z_i and a binary indicator process x_i of whether source i is on or off.

Thus $\overline{\overline{y}}_i = x_i z_i$, and globally $\overline{\overline{\mathbf{y}}} = \mathbf{x} * \mathbf{z}$, with $\mathbf{x}$ and $\mathbf{z}$ assumed to be two independent processes.

The conditional posterior probability of neural current distribution knowing current multipole moments $\mathbf{m}_{\mathcal{C}_j}$ is given by

$$p(\mathbf{x}, \mathbf{z} | \mathbf{m}_{\mathcal{C}_\mathbf{j}}) = \frac{p(\mathbf{m}_{\mathcal{C}_\mathbf{j}} | \mathbf{x}, \mathbf{z}) p(\mathbf{x}) p(\mathbf{z})}{p(\mathbf{m}_{\mathcal{C}_\mathbf{j}})}. \tag{82}$$

The MAP estimate of the set of dipole amplitudes that will match the ECM moments of $\mathbf{m}_{\mathcal{C}_j}$ writes:

$$\overline{\overline{\mathbf{y}}}_j = \{x_i z_i, \mathbf{d}_i \in \zeta_j\} = \arg\max_{\mathbf{x}, \mathbf{z}} \; p(\mathbf{x}, \mathbf{z} | \mathbf{m}_{\mathcal{C}_\mathbf{j}}). \tag{83}$$

The underlying MRF of the indicator process $\mathbf{x}$ follows a Gibbs distribution which energy function $V(x)$ writes:

$$V(\mathbf{x}) = \sum_{i, \mathbf{d}_i \in \zeta_j} (\alpha_i x_i \quad + \beta_i \sum_{k \in \nu^i} \frac{(x_i - x_k)^2}{\gamma_{ik}}), \tag{84}$$

where $\alpha_i > 0$ and $\beta_i > 0$ determine the sparseness and clustering relative weights; ν^i is the set of nearest neighbors of vertex i, and γ_{ik} is proportional to the geodesic distance between $\mathbf{d}_i$ and $\mathbf{d}_k$ and to the discrepancy between their orientations.

Source amplitudes $\mathbf{z}$ are assumed to be centered and normally-distributed with covariance $\mathbf{C}_\mathbf{z}$. Assuming the perturbation process in (80) to be zero-mean Gaussian with covariance matrix $\mathbf{C}_\mathbf{n}$, we can write

$$p(\mathbf{x}, \mathbf{z} | \mathbf{m}_{\mathcal{C}_\mathbf{j}}) = \frac{1}{D} exp\{-U(\mathbf{x}, \mathbf{z} | \mathbf{m}_{\mathcal{C}_\mathbf{j}})\}, \tag{85}$$

where D is the posterior partition function.

The MAP estimation from (83) reduces to the minimization of the energy functional associated to the posterior distribution of $\overline{\overline{\mathbf{y}}}_j$:

$$U(\mathbf{x},\mathbf{z}|\mathbf{m}_{\mathcal{C}_j}) = \frac{1}{2}[\mathbf{m}_{\mathcal{C}_j} - \mathbf{G}_j^m\mathbf{x}*\mathbf{z}]^t\mathbf{C}_n^{-1}[\mathbf{m}_{\mathcal{C}_j} - \mathbf{G}_j^m\mathbf{x}*\mathbf{z}] + \frac{1}{2}\mathbf{z}^{\mathbf{T}}\mathbf{C}_{\mathbf{z}}^{-\mathbf{1}}\mathbf{z} + V(x). \quad (86)$$

Minimization of $U(\mathbf{x},\mathbf{z}|\mathbf{m}_{\mathcal{C}_\mathbf{j}})$ is difficult since the optimization procedure must be performed over a mixture of discrete and continuous variables. We will use a modified version of the optimization procedure given in [84] based on Mean Field Annealing.

This method works as follows. Since the function is quadratic in continuous variable $\mathbf{z}$, we can derive closed form of expression for the optimal $\mathbf{z}^*$ as a function of particular indicator process $\mathbf{x}$:

$$\mathbf{z}^*(\mathbf{x}) = \mathbf{C}_\mathbf{z}\mathbf{x}(\mathbf{G}_\mathbf{j}^\mathbf{m})^\mathbf{T}(\mathbf{G}_\mathbf{j}^\mathbf{m}\mathbf{x}\mathbf{C}_\mathbf{z}\mathbf{x}(\mathbf{G}_\mathbf{j}^\mathbf{m})^\mathbf{T} + \mathbf{C}_\mathbf{n})^{-\mathbf{1}}\mathbf{m}_{\mathcal{C}_\mathbf{j}}. \quad (87)$$

Substituting $\mathbf{z}^*(\mathbf{x})$ into $U(\mathbf{x},\mathbf{z}|\mathbf{m}_{\mathcal{C}_\mathbf{j}})$ result in

$$\tilde{U}(\mathbf{x}|\mathbf{m}_{\mathcal{C}_\mathbf{j}}) = U(\mathbf{x},\mathbf{z}|\mathbf{m}_{\mathcal{C}_\mathbf{j}})|_{\mathbf{z}=\mathbf{z}^*(\mathbf{x})}, \quad (88)$$

which is a Gibbs energy function for the binary density

$$\tilde{p}(\mathbf{x}|\mathbf{m}_{\mathcal{C}_\mathbf{j}}) = \frac{1}{\tilde{K}}\{-\tilde{U}(\mathbf{x}|\mathbf{m}_{\mathcal{C}_\mathbf{j}})\}. \quad (89)$$

We can therefore first find the optimal indicator process $\mathbf{x}$ by minimizing $\tilde{U}(|\mathbf{m}_{\mathcal{C}_\mathbf{j}})$, and then substituting this result in (87) to get the optimal amplitude process.

Identifying the elements of ζ_j is achieved through a recursive and iterative surface region-growing process. The process is recursive and considers each dipolar source in $\mathcal{C}_j$ as a seed to a patch growing process. This latter consists of a recursive estimation of the local current density on a growing number of source candidates in the vicinity of every seed until $U(\mathbf{x},\mathbf{z}|\mathbf{m}_{\mathcal{C}_\mathbf{j}})$ is minimized. At each iteration, this latter is minimized with the iterated conditional mode (ICM) optimization of the binary indicator process.

For every seed $\mathbf{d}_i \in \mathcal{C}_j$:

1. Initialization: set $k = 1$, the patch around the source i to $\nu_k^i = \{i\}$ and $U_0^i = 0$;
2. Estimate $\overline{\overline{\mathbf{y}}}_j$ and compute U_k^i from (86);
3. If $|U_k^i - U_{k-1}^i| > \epsilon U_{k-1}^i$
   a) Grow the patch by including the vertices connected to the source(s) in $\nu_k^i = \{i\}$;
   b) Set $k = k + 1$ and move to next seed in $\mathcal{C}_j$.
4. else:
   a) Define $U^i = U_{k-1}^i$;
   b) Define the best patch obtained from seed i, $\Pi^i = \nu_i^{k-1}$;
   c) Proceed to next seed.

We define the optimal sparse focal equivalent image support to $\mathbf{m}_{\mathcal{C}_j}$ as follows

$$\zeta_j = \cup_{i \in I} \Pi^i, \tag{90}$$

with

$$I = \{i, U^i \leq \overline{U}^i - 3\sigma_{U^i}\}, \tag{91}$$

where $\overline{U}^i$ (resp. σ_{U^i}) is the sample mean (resp. standard deviation) of the U^i's obtained for each seed at step 4a.

This process is repeated for the n_c clusters.

Results

We will present MCR first through simulated datasets in two scenarios. Then we will present performances of MCR on real somaesthetic data of four right hand fingers.

Data processing, forward modeling and visualization is achieved through Brainstorm Matlab ToolBox. Experimental data was acquired by Sabine Meunier using a 151-channel axial gradiometer CTF system.

Simulated data

We tested the method on simulated data in single source and two source scenarios, to obtain a quantitative analysis of MCR.

A high resolution tessellation of the grey/white matter boundary was obtained from the segmentation of the MRI data set with the BrainSuite software. To ensure high spatial resolution we used a tessellation of 37,723 vertices and 76,952 faces, with an average triangle area of $2.59mm^2$.

At every MC trial, an equivalent patch was estimated. $\mathbf{C_n}$ was chosen as $\alpha^2 I$ with $\alpha^2 = 10^{-2}$ (SNR), and $\mathbf{C_z}$ as $\alpha_z^2 I$ with $\alpha_z^2 = 100[nA.m]^2$ (to approximate actual current distribution of cortex and real SNR conditions in a typical MEG experiment). α_i and β_j were set to 10^{-5} for every source, and no priors besides connectivity were taken into account and hence $\gamma_{i,j} = 1$ for all pairs of neighbors. ϵ was set to 10^{-6}. Values of parameters were chosen following [84].

An active area of cortex was modeled by first randomly selecting a vertex and then adding its nearby vertices until the desired patch size achieved.

Accuracy criteria

Performance evaluation criteria consisted of uniformly weighted sums of (i) distance between the original and remapped patch centroid; (ii) difference between the area of the original and remapped patch; (iii) the subspace correlation between original and remapped patch (subspace correlation is explained in the next section).

These criteria take their values between 0% (no match) and 100% (perfect match).

Single source case

Monte-Carlo (MC) simulations were performed by growing about 2500 cortical patches at randomly selected locations on the cortical surface with areas ranging

from $5cm^2$ to $30cm^2$ (mean $17.27cm^2$). Uniform illumination was assigned to the cortical dipoles within a patch using a 100-time-sample waveform for active dipoles. MEG signals were simulated on 151 axial gradiometers ($5cm$ baseline) uniformly distributed about the upper hemisphere of a spherical head. Gaussian white noise was added to the signals with a uniform level across all the channels of 10% of the peak of maximum amplitude. To account for the performance, the patches generated in the MC simulations were gathered in 5 classes according to their areas. Each class was labeled by the average value of the patch areas within that class: Class1= $6.31Cm^2$; Class2= $12.00Cm^2$; Class3= $17.46Cm^2$; Class4= $22.75Cm^2$; Class5=$27.84Cm^2$.

Figure 22 in blue legend shows that there is no significant degradation of the method with increasing area (average accuracy 89% with vertical bar showing standard errors). MCR performs well with patches belonging to all area classes.

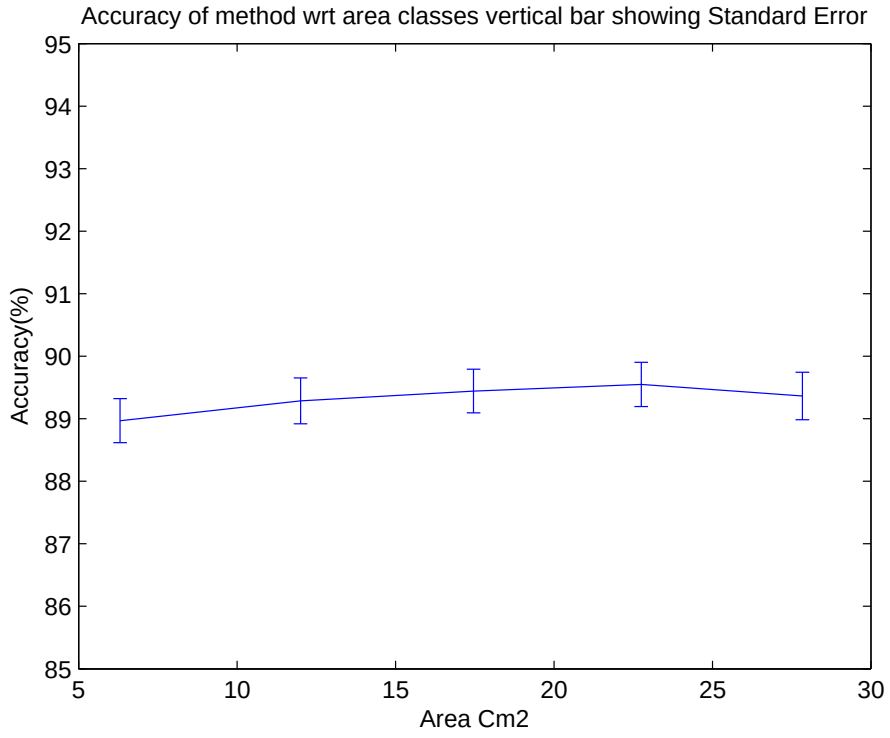

Figure 19: Accuracy of classes with vertical bar showing standard errors.

The subspace correlation between original and remapped patches is shown in

Figure 20. The subspace correlation is obtained from the ordered set of cosines of the principles angle defined in [38]. The subspace correlation is the cosine of the smallest principal angle and will be unity if the two matrices have at least one dimensional subspace in common. In fact,

$$cos(\theta) = \mathbf{U^t V}, \tag{92}$$

where $\mathbf{U}$ and $\mathbf{V}$ are subspaces spanned by original and remapped patches, respectively.

Results show high degree of subspace correlation between original and remapped patches.

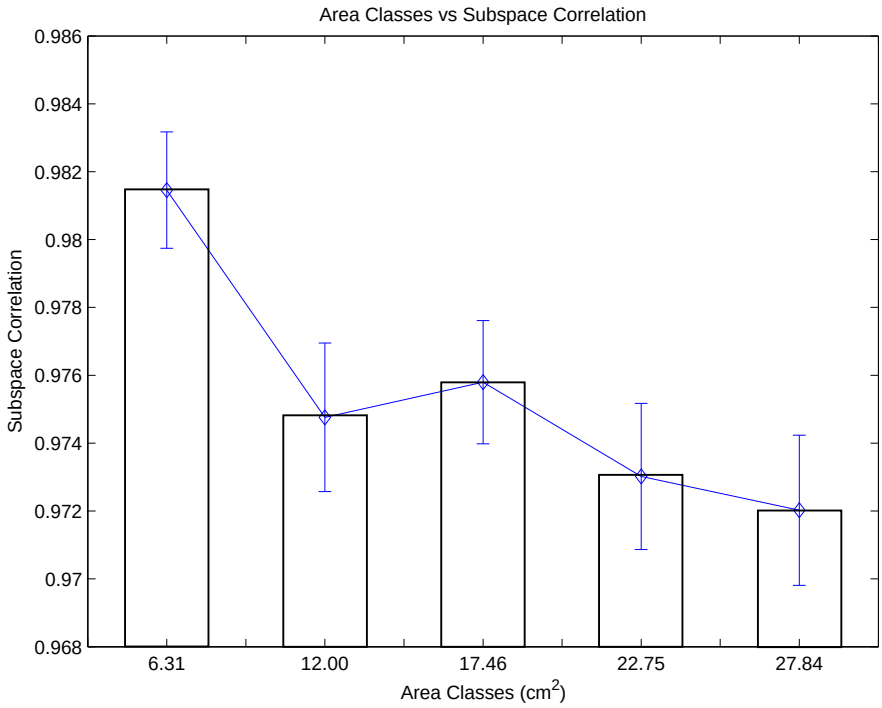

Figure 20: Subspace correlation of Classes with vertical bar showing standard errors.

The performance of the method in determining area of the patch is shown in Figure 21. Results are presented in the form of linear regression between original and estimated area and the best linear line through scatter plot is estimated through quadratic minimization. It is very clear from the figure that the method performs with good accuracy and the original surface area is restored with a high precision. The estimator recovers quantitatively the area of the original surface with a correlation of 0.98 for 2500 patches at an average error of $0.2cm^2$.

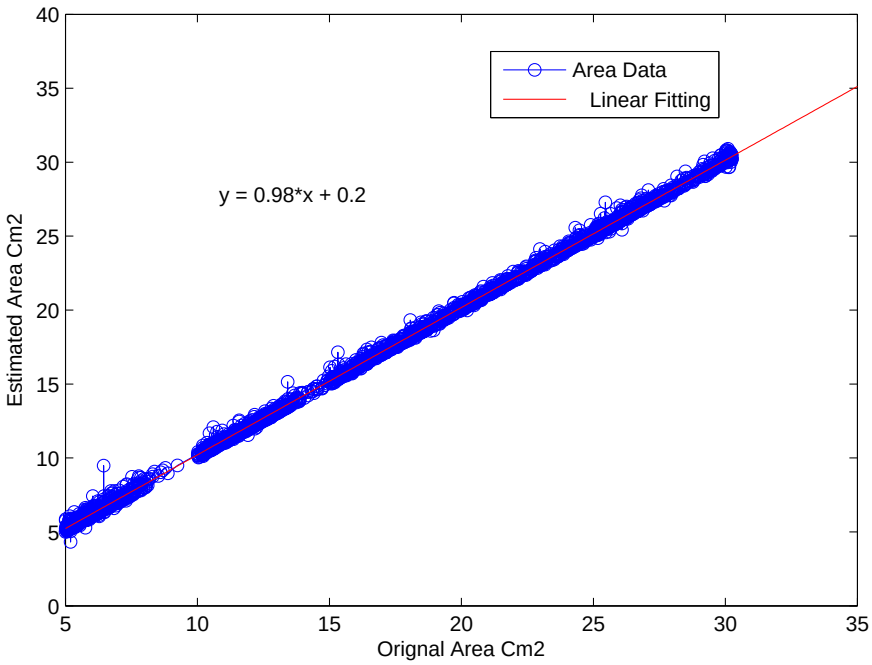

Figure 21: Scatter plot showing original area vs estimated area with straight line representing linear fit.

Robustness of MCR against changes in the threshold

Robustness of MCR against threshold value is presented by decreasing threshold value 4 fold and performing 2500 Monte Carlo simulations, as stated in the

previous sections.

It is clear in Figure 22 (red legend) that the average accuracy increases for almost all classes (average accuracy is more than 90%). However by decreasing 4 fold the threshold the computation time increases manyfold, as now more seeds need to be evaluated to find the best equivalent patch.

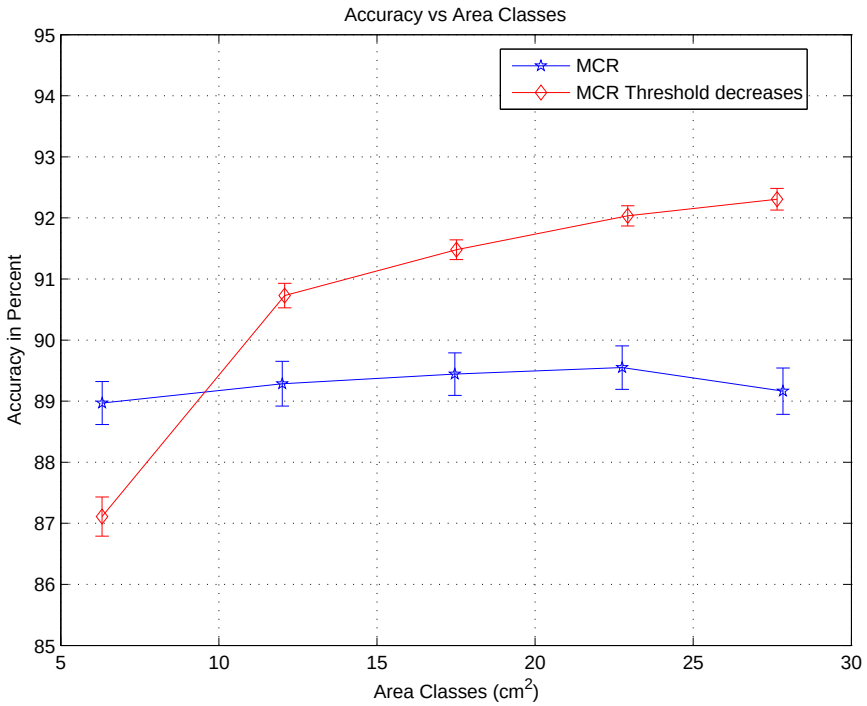

Figure 22: Accuracy of classes with vertical bar showing standard errors under normal MCR parameters (in blue) and smaller threshold parameters (in red).

Two-source case

For the two source scenario we performed simulations by generating two random patches of about $5cm^2$ and $10cm^2$ on the cortex. This time we evaluated repeatability of the performance of MCR by repeating the process of estimation 200 times for these two patches.

The difference in area between original and remapped patches, and accuracy of MCR as described in Section for the patch of $10cm^2$ were calculated. A bootstrap based confidence interval for the repeatability of these two statistics was also computed [27]. This bootstrapping was performed as shown in Figure 23 in which $n = 200$ and $B = 5000$.

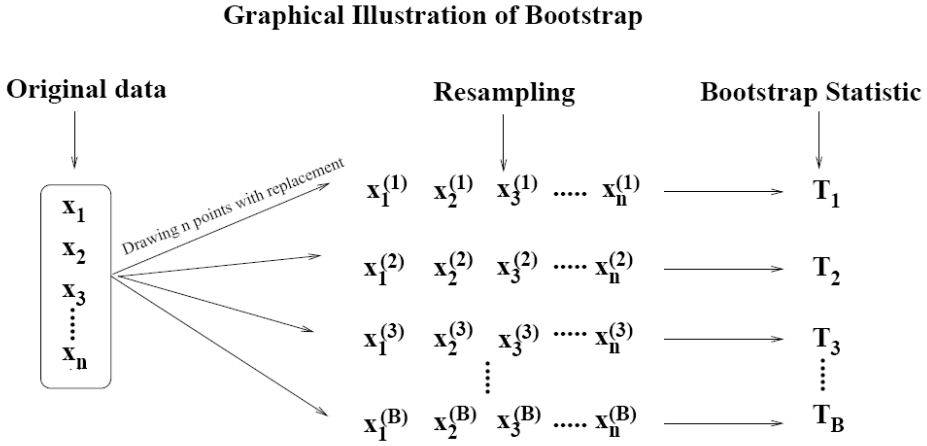

Figure 23: Illustration of the bootstrap estimate of confidence intervals.

To obtain the 95% confidence interval of repeatability, we took 2.5 % and 97.5% quantities of the B replication $T_1, T_2, \ldots, T_B$ as the lower and upper bounds, respectively.

Table 1 presents the repeatability of MCR at 95% confidence interval in a two source configuration for a patch of size $10cm^2$. It is clearly visible from the table that repeatability of MCR is very good and remains within a very narrow limit.

	Confidence interval 95%	
	Lower bound	Upper bound
Average accuracy	81.1%	90.8%
Difference area	$0.14cm^2$	$0.93cm^2$

Table 1: Confidence interval for repeatability of MCR.

The reconstruction of these two patches by MCR is presented in Figure 24, which shows that MCR works accurately in determining the spatial extent of the patches.

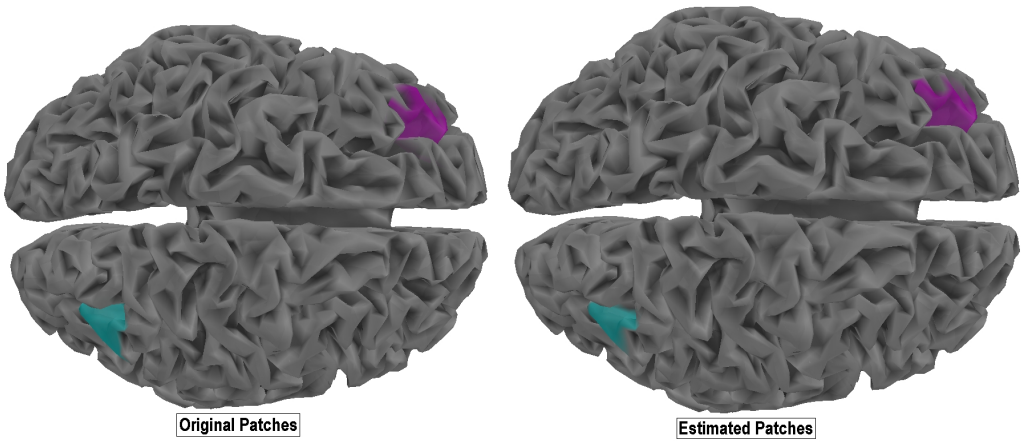

Figure 24: Reconstruction by MCR in two source scenario.

Experimental data

The functional mapping of limbs and fingers is a matter of great interest in MEG community and it is widely known as somaesthetic mapping. The early neural responses at about $40ms$ following stimulation of hand fingers, follows a somaesthetic organization along the post-central sulcus. Somatosensory source models are mostly considered as ECD models for these early responses. However, data from animal models indicates that even though there is some somaesthetic organization of finger areas, these latter might be larger than expected and overlap considerably. These findings indicate that ECD based model are not very useful for somaesthetic mapping as they cannot describe the spatial extent of the somaesthetic sources.

The data for somaesthetic mapping were gathered for one healthy right-handed male [71]. The somatosensory stimulation was an electrical square-wave pulse delivered separately to four fingers of each hand: thumb, index, middle, and pinky finger. The stimulation was applied between the middle and distal phalanxes of each finger. The stimulation order was randomized. The pulse duration was 0.2 ms and the amplitude was set to twice the perceptual threshold. The interstimulus interval (ISI) was varied randomly from 350 to 550 ms to minimize habituation and anticipation effects. The magnetic fields were recorded with a CTF Systems Inc. Omega 151 system with 151 channels. For each finger, a 300-ms interval, including a 50-ms prestimulus interval, was recorded at a sampling rate of 1250Hz. The number of single trials per finger after removal of those corrupted by artifacts ranged from 386 to 415. The DC offset of the gradiometers was removed from all single trials based on the prestimulus interval. Data for each finger were averaged and bandpassed between 3Hz-90Hz.

We applied MCR on this data at $40ms$ latency. Results revealed the expected somaesthetic organization of the finger primary cortical projections, with a large degree of overlap between fingers, the thumb having the largest area (see Figure .)

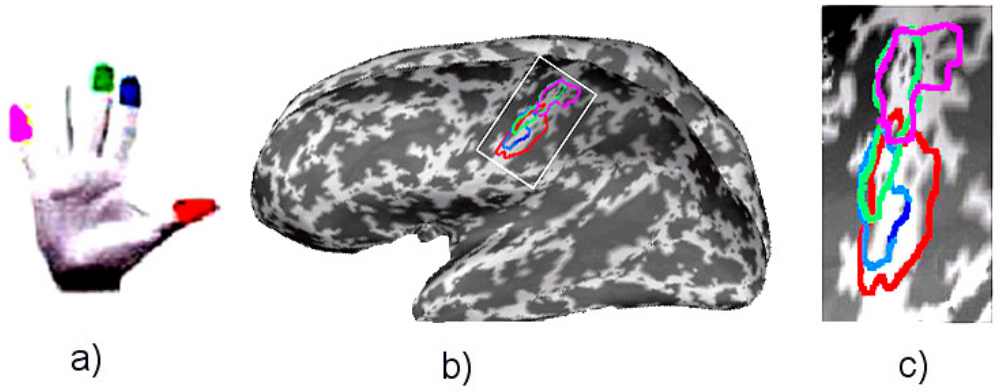

Figure 25: (a) Color-encoding of the four fingers stimulated in the study, as used in subsequent figures; (b) Estimation of the respective spatial extent of the cortical responses; (c) Zoom view of the cortical responses.

Table 2 presents the area of active cortex in response to stimulus for right hand four fingers.

	Right hand fingers
Thumb	$9.29cm^2$
Index	$3.58cm^2$
Middle	$5.23cm^2$
Pinky	$4.71cm^2$

Table 2: Estimated activated cortical surface areas in response to stimulation of each of the right hand fingers.

We also used MCR to evaluate the area of the active cortex in the primary and secondary sensory areas. The results presented in Figure 26 are for the right hand index finger.

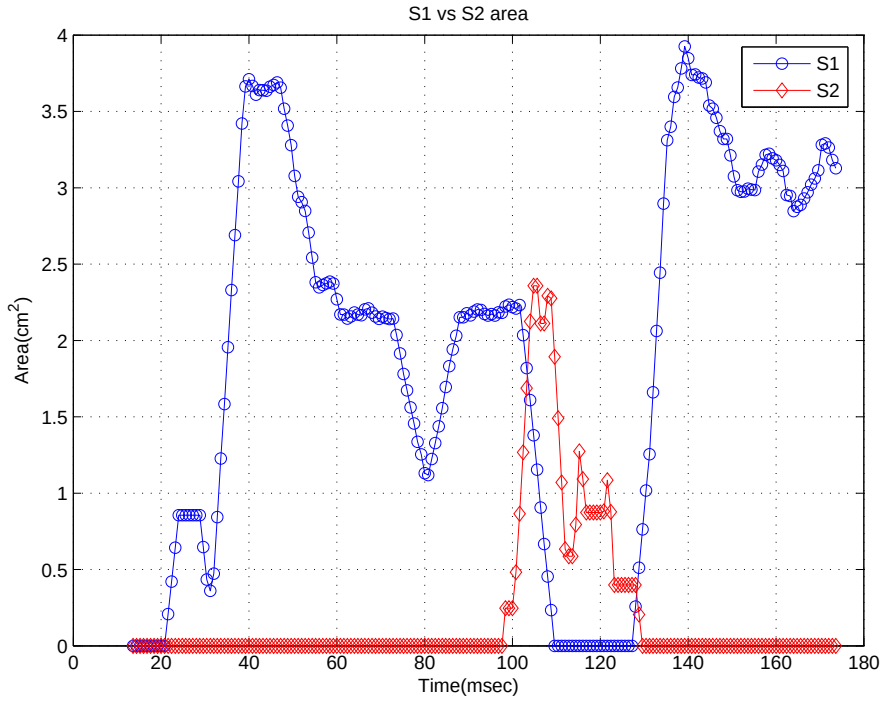

Figure 26: Active surface areas in S_1 and S_2 regions.

These results are in accordance with the existing neurological data for this experiment [18] and demonstrate effectiveness of MCR on real data.

Conclusion

We have presented a fast and robust method for estimating the spatial extent of cortical currents from MEG data. Results from extensive Monte-Carlo simulations show excellent performances in terms of spatial characterization even for very large patches of $30cm^2$. The estimation of the surface area of active regions is very accurate. Average error is only $0.2cm^2$ for 2500 patches. The results for two sources show that the method reveals the repeatability of MCR. Good results for somaesthetic data prove that the method works adequately with real data.

Part 3

MEG SOURCE CHARACTERIZATION

Helmholtz-Hodge Decomposition

Introduction

The Helmholtz-Hodge Decomposition (HHD) is a technique used to decompose a 2D (resp. 3D) continuous vector field into a sum of three parts:

- a non-rotational part deriving from the gradient of a scalar potential U;
- a non-diverging part deriving from the rotational of a scalar potential A (resp. vectorial potential);
- a harmonic part, *i.e.*, whose Laplacian vanishes.

The non-rotational component corresponds to the diverging components such as sources and sink in the vector field. The non-diverging part contains information about rotating components of motion fields such as vortices. The harmonic vectorial component is both divergence- and curl-free revealing travelling objects in the vector field. So by identifying these components, different features in the vector field may be extracted.

Features of a vector field are described as patterns or structures of interest like sources, sinks and vortices. All these features must be detected and analyzed in order to understand the physical behavior of a flow. Although feature analysis

is an important area, only a few technical tools are available for their detection and visualization in the context of vector fields [91].

HHD is used to detect features in vector fields, but in most of the current literature it is described on flat 2D surfaces [41] or on 3D space [98]. Even if some authors describe it on polyhedral surfaces [86] computation are performed locally on the Euclidean space. As shown in [59], the surface curvature has to be taken into account for a proper estimation of vector fields on the tangent spaces. Moreover, results on convergence are sensitively modified by non-flatness properties. In this chapter, we redefine HHD on Riemannian space which enables to detect features in motion fields even on highly curved surfaces such as the cortex.

The detection of features in motion field is important in a wide variety of fields: [82, 42]. In airplane wind tunnel testing, identification of vortices on wings are crucial for identifying lift of the plane [1] (Figure 27 (a)). This problem has applications in meteorology also, for instance, to identify hurricanes on the surface of the earth [17] (Figure 27 (a)). In cardiac motion analysis heart beats are represented as sources and sinks [42]. The identification of all these points is thus precious to understand and predict the phenomena of interest. Moreover, feature identification also allow a compact representation of the vector field [91].

This feature detection takes place in three steps. First we estimate optical flow on 2-Riemannian Manifold. We then apply Helmholtz-Hodge decomposition to decompose optical flow in non-rotational scalar potential, rotational (solenoid) scalar potential and harmonic vector field. Now the task of identifying features simplifies to identifying critical points of two scalar potentials, and moving object can be identified by locating highest norm vectors of the harmonic component.

The aim of this chapter is twofold: first redefinition of HHD on 2-Riemannian manifold and secondly its application to feature detection in optical flow on general surfaces.

In subsequent sections we will first explain the Riemannian framework for Vectorial PDE; this framework is adapted from [59]. We then revisit the optical

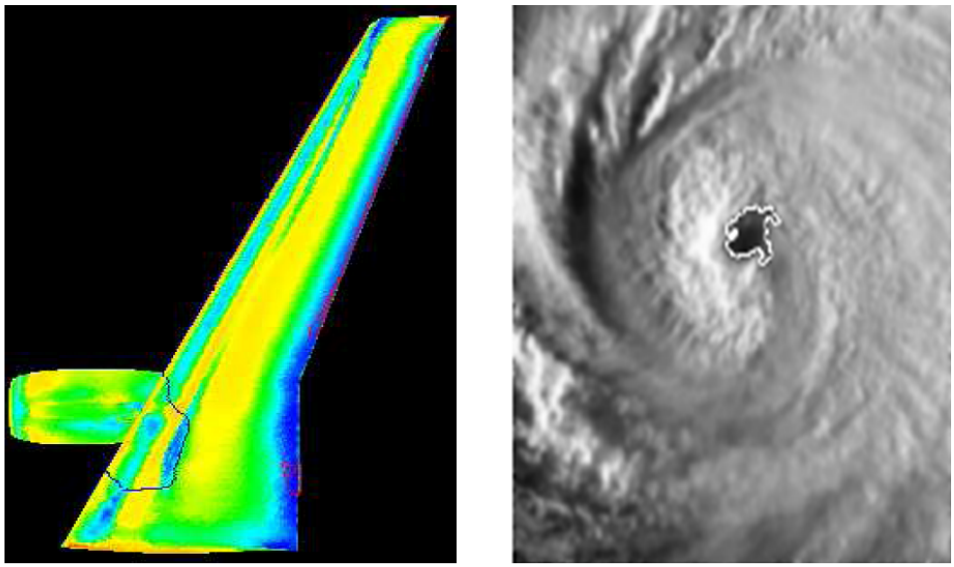

Figure 27: (a) Strength of vortices on wings of the plane; (b) Identification of hurricanes eye.

flow on non flat surfaces. A new framework of HHD on 2-Riemannian manifold will be defined next. Lastly, we will present results on an application of HHD on different kinds of surfaces.

Vector fields on manifolds

We first recall some necessary background about differential geometry. For a more detailed introduction, see [28].

Let $\mathcal{M}$ be a 2-Riemannian manifold representing an imaging support (for example the surface of a planet or the highly circumvoluted brain envelope), parameterized by the local coordinate system $\phi : p \in \mathcal{M} \mapsto (x_1, x_2) \in \mathbb{R}^2$. We introduce a scalar quantity defined in time on a 2-dimensional surface (*e.g.*, weather data or time-evolving estimates of brain activation) as a function

$$I : (p, t) \in \mathcal{M} \times \mathbb{R} \longmapsto \mathbb{R}.$$

As for Euclidean spaces, it is possible to define vectors on manifolds and we

provide the most intuitive approach to this question.

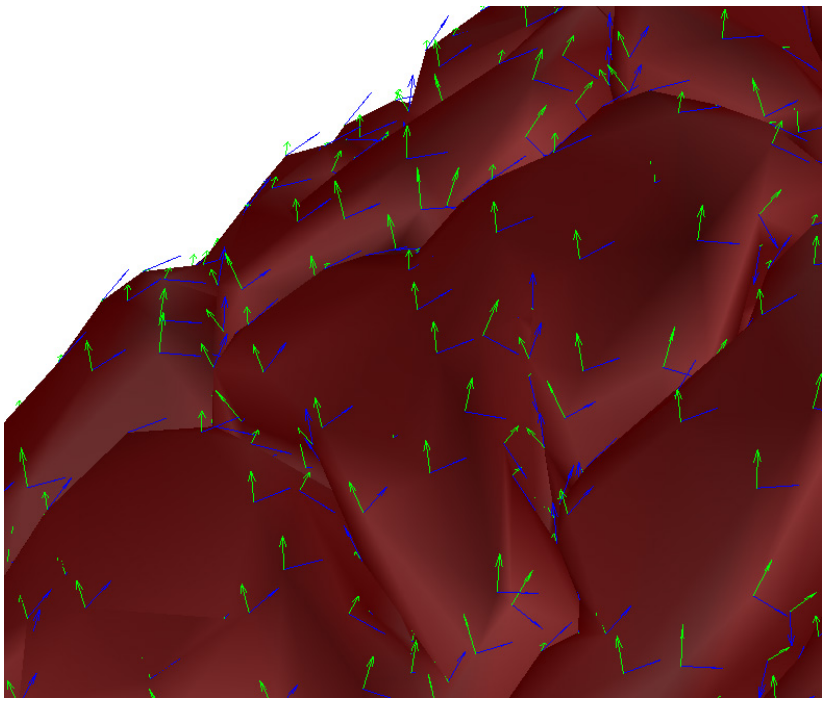

Figure 28: Basis vectors (in blue and green) are defined on locally tangent planes at each node of a triangulation of the cortical surface (in purple).

Considering a curve $\gamma(t)$ defined on $\mathcal{M}$ such as $\gamma(0) = p$, we note that $\gamma'(0)$ does not depend on the local coordinate system. For any curve $\gamma(t)$, the tangent vector $\gamma'(0)$ engenders a tangent space $T_p\mathcal{M}$ at point p. The canonical basis of this vectorial space is

$$\mathbf{e}_\alpha = \gamma'_\alpha(0) := \frac{\partial}{\partial x_\alpha},$$

where $x_\beta\big(\gamma_\alpha(t)\big) = t\delta_{\alpha,\beta}$.

Proceeding identically at any point of the manifold, we define $T\mathcal{M} = \bigcup_p T_p\mathcal{M}$, the tangent bundle of $\mathcal{M}$. Thus a vector field $\mathbf{V}$ is naturally defined as an application

$$\mathbf{V} : \mathcal{M} \longrightarrow T\mathcal{M}.$$

We further proceed by suggesting adaptations to the concepts of angle and distance as defined on a manifold. $\mathcal{M}$ may be equipped with a Riemannian metric.

Hence at each point p of $\mathcal{M}$, there exists a positive-definite form:

$$g_p : T_p\mathcal{M} \times T_p\mathcal{M} \longrightarrow \mathbb{R},$$

which is differentiable with respect to p. Hereafter, we note $(g_p)_{\alpha,\beta} = g_p\big(\mathbf{e}_\alpha, \mathbf{e}_\beta\big)$. A natural choice for g_p is the restriction of the Euclidean metric to $T_p\mathcal{M}$, which we have adopted for subsequent computations. Next, we will only refer to g_p as g.

Integrating on a manifold now becomes possible using a *volume form*, *i.e.*, a differential 2-form:

$$\mathrm{d}\mu_{\mathcal{M}} : T\mathcal{M} \times T\mathcal{M} \longrightarrow \mathbb{R}.$$

The most convenient volume form may be associated to the metric g via: $\sqrt{\det(g_{\alpha,\beta})}\mathrm{d}x_1\mathrm{d}x_2$.

Optical flow on a Riemannian manifold

This section summarizes results from Lefèvre and Baillet on which we have based the HHD extension [59].

As in classical computation approaches to optical flow, we now assume that the activity of a point moving on a curve $p(t)$ in $\mathcal{M}$ is constant along time. The condition

$$\frac{d}{dt}\Big[I\big(p(t),t\big)\Big] = 0$$

yields

$$\partial_t I + D_{p(t)}I(\dot{\mathbf{p}}) = 0, \tag{93}$$

where D_pI is the differential of I at point p, that is, the tangent linear application given by

$$D_pI : T\mathcal{M} \longrightarrow \mathbb{R}.$$

$\dot{\mathbf{p}} = \mathbf{V} = (V^1, V^2)$ stands for the unknown motion field we aim at computing. However, mathematically speaking, the notion of differential is not intuitive when manipulating vector fields. In this regard, we adopt an opposite approach to the one exposed in [10] for Maxwell's equations where differential forms are preferred

to vector fields. We will come back to this point at the discretization step. That is why we express the linear application D_pI as a scalar product and thus introduce $\nabla_{\mathcal{M}}I$, the gradient of I which is defined as the vector field satisfying at each point p the following:

$$\forall \mathbf{V} \in T_p\mathcal{M}, g(\nabla_{\mathcal{M}}I, \mathbf{V}) = D_pI\big(\mathbf{V}\big).$$

(93) can thereby be transformed into an optical-flow type of equation:

$$\partial_t I + g(\mathbf{V}, \nabla_{\mathcal{M}}I) = 0. \tag{94}$$

We note that (94) takes the same form as general conservation laws defined on manifolds in [88]. Here, only the component of the flow $\mathbf{V}$ in the direction of the gradient is accessible to estimation. This corresponds to the well-known *aperture problem* [49], which requires additional constraints on the flow to yield a unique solution.

Regularization

The previous approach classically reduces to minimizing an energy functional such as the one in [49]:

$$\mathcal{E}(\mathbf{V}) = \int_{\mathcal{M}} \left[\frac{\partial I}{\partial t} + g(\mathbf{V}, \nabla_{\mathcal{M}}I)\right]^2 \mathrm{d}\mu_{\mathcal{M}} + \lambda \int_{\mathcal{M}} \mathcal{C}(\mathbf{V})\mathrm{d}\mu_{\mathcal{M}}. \tag{95}$$

The first term is a measure of fit of the optical flow model to the data, while the second one acts as a spatial regularizer of the flow. The scalar parameter λ tunes the respective contribution of these two terms in the net energy cost $\mathcal{E}(\mathbf{V})$. Here we rewrite the smoothness term from [49], which can be expressed as a Frobenius norm:

$$\mathcal{C}(\mathbf{V}) = \mathrm{Tr}({}^t\nabla\mathbf{V} \cdot \nabla\mathbf{V}), \tag{96}$$

where

$$\big(\nabla\mathbf{V}\big)^{\beta}_{\alpha} = \partial_\alpha V^\beta + \sum_\gamma \Gamma^\beta_{\alpha\gamma} V^\gamma$$

is the covariant derivative of $\mathbf{V}$, a generalization of vectorial gradient. $\partial_\alpha V^\beta$ is the classical Euclidian expression of the gradient, and $\sum_\gamma \Gamma^\beta_{\alpha\gamma} V^\gamma$ reflects local

deformations of the tangent space basis since the Christoffel symbols $\Gamma_{\alpha\gamma}^{\beta}$ are the coordinates of $\partial_\beta \mathbf{e}_\alpha$ along $\mathbf{e}_\gamma$. This rather complex expression ensures the tensoriality property of $\mathbf{V}$, *i.e.*, invariance with parametrization changes.

This constraint will tend to generate a regularized vector field with small spatial derivatives, that is a field with weak local variations. Such a regularization scheme may be problematic in situations where spatial discontinuities occur in the image sequences. For example, in the case of a moving object on a static background, the severe velocity discontinuities around the object contours are eventually blurred in the regularized flow field (see [109] for a taxonomy of other possible terms).

Variational formulation

Variational formulation of 2D-optical flow equation has been first proposed by Schnörr in [92]. The advantage of such formulation is twofold. Theoretically, it ensures that the problem is well-posed, that is, there exists a unique solution in a specific and convenient function space, *e.g.*, a Sobolev space [92], or a space of functions with bounded variations [3]. Numerically, it allows to solve the problem on discrete irregular surface tessellations and to yield discrete solutions belonging to the chosen function space. A possible restriction can be done when dealing with non-quadratic regularizing terms where iterative methods must replace matrix inversions. We derive a variational formulation in the case of Horn & Schunk isotropic smoothness priors, but the general framework remains the same for Nagel's anisotropic image-driven regularization approach [77].

Considering $\mathcal{M}$, we need to define a working space of vector fields $\Gamma^1(\mathcal{M})$ on which functional $\mathcal{E}(\mathbf{V})$ will be minimized. Let us first denote the Sobolev space $H^1(\mathcal{M})$ defined in [29] as the completion of $C^1(\mathcal{M})$ (the space of differentiable functions on the manifold) with respect to $\| \cdot \|_{H^1}$ derived from the following scalar product

$$< u, v >_{H^1} = \int_{\mathcal{M}} uv \, \mathrm{d}\mu_{\mathcal{M}} + \int_{\mathcal{M}} g(\nabla u, \nabla v) \, \mathrm{d}\mu_{\mathcal{M}}.$$

We choose a space of vector fields in which the coordinates of each element are located in a classical Sobolev space:

$$\Gamma^1(\mathcal{M}) = \Big\{ \mathbf{V} : \mathcal{M} \to T\mathcal{M} \ / \ \mathbf{V} = \sum_{\alpha=1}^{2} V^\alpha \mathbf{e}_\alpha,\, V^\alpha \in H^1(\mathcal{M}) \Big\}, \tag{97}$$

with the scalar product given by

$$< \mathbf{U}, \mathbf{V} >_{\Gamma^1(\mathcal{M})} = \int_{\mathcal{M}} g(\mathbf{U}, \mathbf{V}) \ \mathrm{d}\mu_{\mathcal{M}} + \int_{\mathcal{M}} \mathrm{Tr}({}^t\nabla\mathbf{U}\nabla\mathbf{V}) \ \mathrm{d}\mu_{\mathcal{M}}.$$

$\mathcal{E}(\mathbf{V})$ can be simplified from (95) as a combination of the following constant, linear and bilinear forms:

$$\begin{aligned}
K(t) &= \int_{\mathcal{M}} \big(\partial_t I\big)^2 \mathrm{d}\mu_{\mathcal{M}} \ , \\
f(\mathbf{U}) &= -\int_{\mathcal{M}} g(\mathbf{U}, \nabla_{\mathcal{M}} I)\partial_t I \ \mathrm{d}\mu_{\mathcal{M}}, \\
a_1(\mathbf{U}, \mathbf{V}) &= \int_{\mathcal{M}} g(\mathbf{U}, \nabla_{\mathcal{M}} I) g(\mathbf{V}, \nabla_{\mathcal{M}} I) \mathrm{d}\mu_{\mathcal{M}} \\
a_2(\mathbf{U}, \mathbf{V}) &= \int_{\mathcal{M}} \mathrm{Tr}({}^t\nabla\mathbf{U}\nabla\mathbf{V}) \ \mathrm{d}\mu_{\mathcal{M}} \\
a(\mathbf{U}, \mathbf{V}) &= a_1(\mathbf{U}, \mathbf{V}) + \lambda a_2(\mathbf{U}, \mathbf{V}).
\end{aligned}$$

Minimizing $\mathcal{E}(\mathbf{V})$ on $\Gamma^1(\mathcal{M})$ is then equivalent to the following problem :

$$\min_{\mathbf{V} \in \Gamma^1(\mathcal{M})} \big(a(\mathbf{V}, \mathbf{V}) - 2f(\mathbf{V}) + K(t) \big). \tag{98}$$

Lax-Milgram theorem ensures uniqueness of the solution with the following assumptions:

1. a and f are continuous forms;
2. $\Gamma^1(\mathcal{M})$ is complete, the bilinear form $a(.,.)$ is symmetric and coercive (elliptic), that is, there exists a constant C such that

$$\forall \ \mathbf{V} \in \Gamma^1(\mathcal{M}), a(\mathbf{V}, \mathbf{V}) \geq C \parallel \mathbf{V} \parallel^2_{\Gamma^1(\mathcal{M})} .$$

Moreover, the solution $\mathbf{V}$ to (98) satisfies:

$$a(\mathbf{V}, \mathbf{U}) = f(\mathbf{U}), \forall \ \mathbf{U} \in \Gamma^1(\mathcal{M}). \tag{99}$$

Continuity of f and a are straightforward. Completeness of $\Gamma^1(\mathcal{M})$ is ensured because any Cauchy sequence has components in $H^1(\mathcal{M})$ which are also Cauchy sequences since $\| \cdot \|_{H^1}$ is bounded by $\| \cdot \|_{\Gamma^1(\mathcal{M})}$.

Proof of coercivity can be adapted – analogously to flat domains [92] – thanks to isothermal coordinates. Indeed, the Korn–Lichtenstein theorem (1914) allows to find a system of coordinates for which the two basis vectors of tangent space are orthogonal. In this basis, calculus are similar to those in Euclidian case by introducing a multiplicative coefficient equal to the norm of the basis vectors.

A big difference with [92] is that the coercivity and therefore well-posedness does not require an assumption about linear independency of the two components of the gradient $\nabla_{\mathcal{M}} I$ (see [59]).

Helmholtz Hodge decomposition on 2-Riemannian manifold

We will now present an extended framework to perform HHD on Riemannian surfaces and show that it can be applied for any vector field defined on a 2-Riemannian manifold $\mathcal{M}$.

Theory

Definitions

In our framework $\mathcal{M}$ is a surface (or manifold) parameterized by local charts (x_1, x_2). Thus, it is possible to get a normal vector at each point

$$\mathbf{n}_p = \frac{\partial}{\partial x_1} \wedge \frac{\partial}{\partial x_2}.$$

It is important to see that the normal does not depend on the choice of the parametrization (x_1, x_2). Then we define the gradient and divergence operators

through duality:

$$\begin{aligned} \mathrm{d}U(\mathbf{V}) &= g(\nabla_{\mathcal{M}} U, \mathbf{V}), \\ \int_{\mathcal{M}} U \mathrm{div}_{\mathcal{M}} \mathbf{H} &= -\int_{\mathcal{M}} g(\mathbf{H}, \nabla_{\mathcal{M}} U). \end{aligned}$$

Scalar and vectorial curl are at last given by

$$\begin{aligned} \mathbf{Curl}_{\mathcal{M}} A &= \nabla_{\mathcal{M}} A \wedge \mathbf{n}, \\ \mathrm{curl}_{\mathcal{M}} \mathbf{H} &= \mathrm{div}_{\mathcal{M}}(\mathbf{H} \wedge \mathbf{n}). \end{aligned}$$

With these formulas we have intrinsic expressions which do not depend on the parametrization of the surface.

Theorem

We start by reformulating results established in [86]. Given $\mathbf{V}$ a vector field in $\Gamma^1(\mathcal{M})$, there exists unique functions U and A in $L^2(\mathcal{M})$ and a vector field $\mathbf{H}$ in $\Gamma^1(\mathcal{M})$ such that

$$\mathbf{V} = \nabla_{\mathcal{M}} U + \mathbf{Curl}_{\mathcal{M}} A + \mathbf{H}, \tag{100}$$

where

$$\begin{aligned} \mathrm{curl}_{\mathcal{M}}(\nabla_{\mathcal{M}} U) &= 0, \\ \mathrm{div}_{\mathcal{M}}(\mathbf{Curl}_{\mathcal{M}} A) &= 0, \\ \mathrm{div}_{\mathcal{M}} \mathbf{H} &= 0, \\ \mathrm{curl}_{\mathcal{M}} \mathbf{H} &= 0. \end{aligned}$$

In practice, few divergence components and a few rotational components are to be found in the field $\mathbf{H}$. To counter this problem, we can further decompose the "harmonic" remainder, $\mathbf{H}$, into three components such that more accurate

results can be obtained. This iterative scheme can be formulated as below:

$$\begin{aligned}
\mathbf{V} &= \nabla_{\mathcal{M}} U_1 + \mathbf{Curl}_{\mathcal{M}} A_1 + \mathbf{H_1}, \\
&= \nabla_{\mathcal{M}} U_1 + \mathbf{Curl}_{\mathcal{M}} A_1 + [\nabla_{\mathcal{M}} U_2 + \mathbf{Curl}_{\mathcal{M}} A_2 + \mathbf{H_2}], \\
&= \nabla_{\mathcal{M}} U_1 + \mathbf{Curl}_{\mathcal{M}} A_1 + \nabla_{\mathcal{M}} U_2 + \mathbf{Curl}_{\mathcal{M}} A_2 \\
&\quad + \ldots + [\nabla_{\mathcal{M}} U_n + \mathbf{Curl}_{\mathcal{M}} A_n + \mathbf{H_n}], \\
&= [\nabla_{\mathcal{M}} U_1 + \nabla_{\mathcal{M}} U_2 + \ldots + \nabla_{\mathcal{M}} U_n] \\
&\quad + [\mathbf{Curl}_{\mathcal{M}} A_1 + \mathbf{Curl}_{\mathcal{M}} A_2 + \ldots + \mathbf{Curl}_{\mathcal{M}} A_n] + \mathbf{H_n}.
\end{aligned}$$

If the number of iterations is large enough, the final curl-free component and the final divergence-free component will be very close to the respective true value. In practice, one iteration is enough to extract useful features of a vector field.

Discretization

In this part we show how to construct the functions U and A starting from theoretical considerations before addressing more practical aspects.

Following classical constructions, U and A will minimize the two functionals:

$$\int_{\mathcal{M}} ||\mathbf{V} - \nabla_{\mathcal{M}} U||^2,$$
$$\int_{\mathcal{M}} ||\mathbf{V} - \mathbf{Curl}_{\mathcal{M}} A||^2,$$

where $||.||$ is the norm associated to the Riemannian metric $g(.,\cdot)$.

These two functionals are convex. Therefore, they carry a minimum on $L^2(\mathcal{M})$ which satisfies:

$$\forall \phi \in L^2(\mathcal{M}), \int_{\mathcal{M}} g(\mathbf{V}, \nabla_{\mathcal{M}} \phi) = \int_{\mathcal{M}} g(\nabla_{\mathcal{M}} U, \nabla_{\mathcal{M}} \phi), \quad (101)$$
$$\forall \phi \in L^2(\mathcal{M}), \int_{\mathcal{M}} g(\mathbf{V}, \mathbf{Curl}_{\mathcal{M}} \phi) = \int_{\mathcal{M}} g(\mathbf{Curl}_{\mathcal{M}} A, \mathbf{Curl}_{\mathcal{M}} \phi). \quad (102)$$

These two equations are very important since they provide the path to numerical computations when the space $L^2(\mathcal{M})$ is approximated by a finite dimension subspace (*e.g.*, continuous linear piecewise functions).

Indeed if we have basis functions $(\phi_1, \ldots, \phi_n)$, then we can write $\mathbf{U} = (U_1, \ldots, U_n)^T$, $\mathbf{A} = (A_1, \ldots, A_n)^T$, and equations (101) and (102) reads in a metrical way:

$$\left[\int_{\mathcal{M}} g(\nabla_{\mathcal{M}}\phi_i, \nabla_{\mathcal{M}}\phi_j)\right]_{i,j} \mathbf{U} = \left[\int_{\mathcal{M}} g(\mathbf{V}, \nabla_{\mathcal{M}}\phi_i)\right]_i \quad (103)$$

$$\left[\int_{\mathcal{M}} g(\mathbf{Curl}_{\mathcal{M}}\phi_i, \mathbf{Curl}_{\mathcal{M}}\phi_j)\right]_{i,j} \mathbf{A} = \left[\int_{\mathcal{M}} g(\mathbf{V}, \mathbf{Curl}_{\mathcal{M}}\phi_i)\right]_i. \quad (104)$$

The harmonic component $\mathbf{H}$ of the vector field $\mathbf{V}$ is obtained simply as

$$\mathbf{H} = \mathbf{V} - \nabla_{\mathcal{M}} U - \mathbf{Curl}_{\mathcal{M}} A. \quad (105)$$

We provide some details about the numerical implementation of (103) and (104), which are defined on a tessellation $\hat{\mathcal{M}}$ approximating the manifold. This tessellation consists of N nodes and T triangles, as shown in Figure 29.

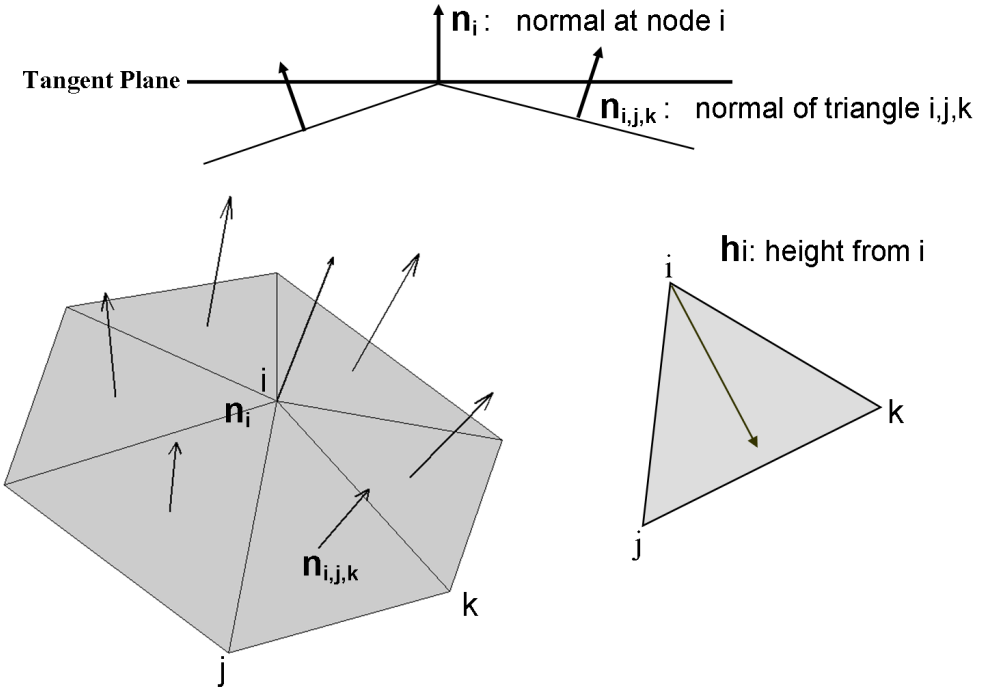

Figure 29: Illustration of local computations and associated definitions from FEM on a triangular surface mesh.

Following the finite element method (FEM), we define N functions, which are continuous piecewise affine, with the property to be equal to 1 at node i and 0 at

all other triangle nodes. They are the basis functions for the approximation. So (103) reads:

$$\left[\sum_{T\ni i,j}\frac{\mathbf{h_i}}{\parallel \mathbf{h_i} \parallel^2}\cdot\frac{\mathbf{h_j}}{\parallel \mathbf{h_j} \parallel^2}\mathcal{A}(T)\right]U=\left[\sum_{T\ni i}\mathcal{A}(T)\mathbf{V}\cdot\frac{\mathbf{h_i}}{\parallel \mathbf{h_i} \parallel^2}\right], \tag{106}$$

where $\mathbf{h_i}$ is the height taken from i in the triangle T, $\mathcal{A}(T)$ is the area of the triangle T.

In the same spirit, (104) is discretized as follows:

$$\left[\sum_{T\ni i,j}\left(\frac{\mathbf{h_i}}{\parallel \mathbf{h_i} \parallel^2}\wedge\mathbf{n}\right)\cdot\left(\frac{\mathbf{h_j}}{\parallel \mathbf{h_j} \parallel^2}\wedge\mathbf{n}\right)\mathcal{A}(T)\right]A=\left[\sum_{T\ni i}\mathcal{A}(T)\mathbf{V}\cdot\left(\frac{\mathbf{h_i}}{\parallel \mathbf{h_i} \parallel^2}\wedge\mathbf{n}\right)\right], \tag{107}$$

where $\mathbf{n}$ is the normal to the triangle T.

Feature detection as critical points of potentials

The critical points of a vector field are often classified depending on the eigenvalues of the Jacobian matrix at a point in a vector field. In our case, however, critical points of the flow can be found as local extrema of the divergence-free potential A (representing rotation) and curl-free potential U (representing divergence). Finding features as critical points on global potential fields is much less sensitive to noise in the data and therefore be less likely to get false positives, in comparison to local Jacobian eigenvalues based methods [68].

A sink corresponds to a local maximum of the potential U, whereas a source corresponds to its local minimum. In Figure 30, a diverging vector field on flat 2D manifold is shown for illustration purposes, it is clearly visible from Figure 30 (b), source and sink of vector fields can easily be detected from the curl free potential U.

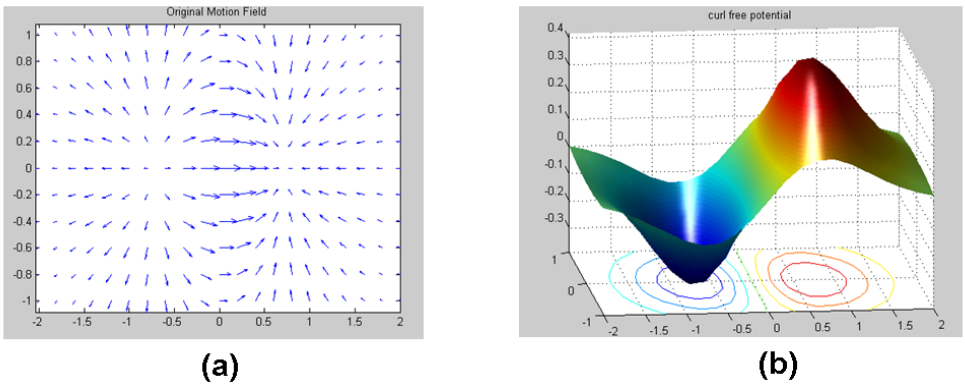

Figure 30: (a) Vector field having source and sink on a flat 2D manifold; (b) Curl-free potential U of vector field.

Figure 31 shows diverging vector field overlap on a spherical manifold (Riemannian manifold), the magnitude of the potential U is shown in color. In Figure 31 (a), a source in the vector field is detected through minima (blue) of U, whereas a sink is identified by maxima (red) in U; see Figure 31 (b).

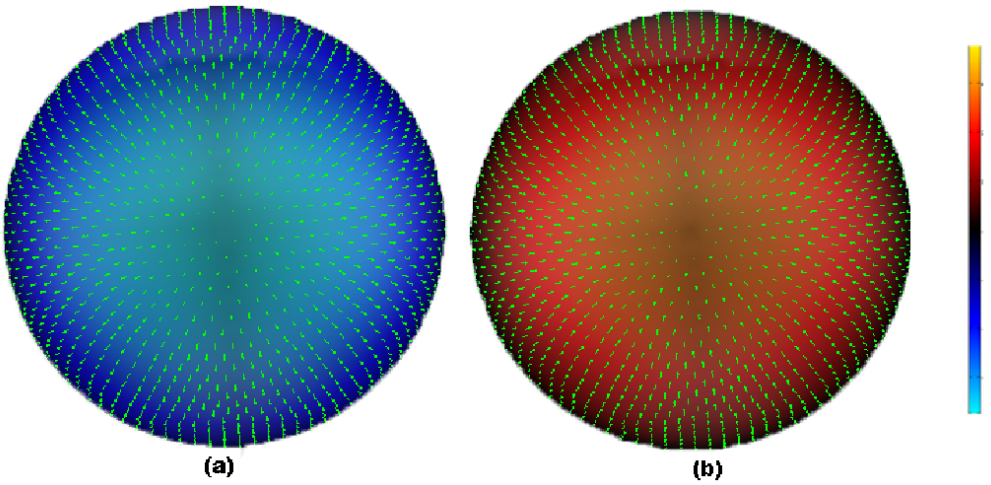

Figure 31: (a) Source vector field overlapped with U on spherical manifold; (b) Sink vector field overlapped with U.

Similarly, counterclockwise and clockwise vortices are represented as local minima and maxima of A, respectively. In Figure 32 (a), a rotating vector field on a flat 2D manifold is shown for illustration purposes. It is clearly visible from Figure 32 (b) that rotating vector field can easily be detected from the divergence free potential A.

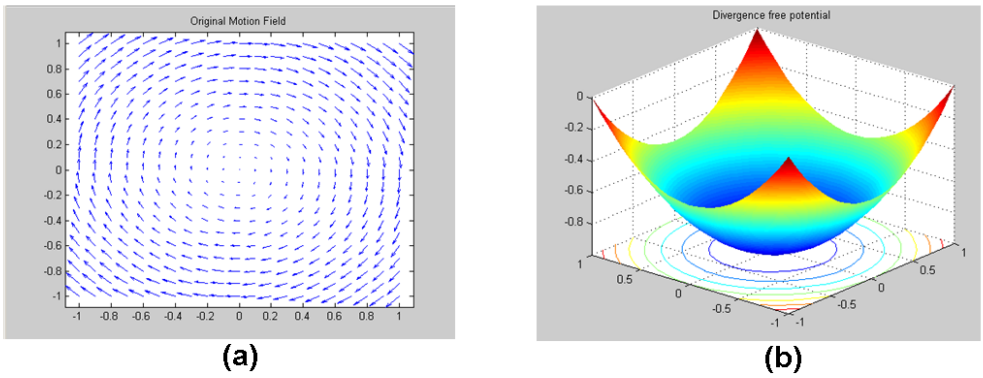

Figure 32: (a) Vector field with vortex on a flat 2D manifold; (b) Divergence-free potential A of a vector field.

Figure 33 shows that a rotating vector field on a spherical manifold, color shows magnitude of the potential A. In Figure 33 (a) counterclockwise vortex

in the vector field is detected by maxima (red) in A, whereas clockwise vortex is identified by minima (blue) in A, Figure 33 (b).

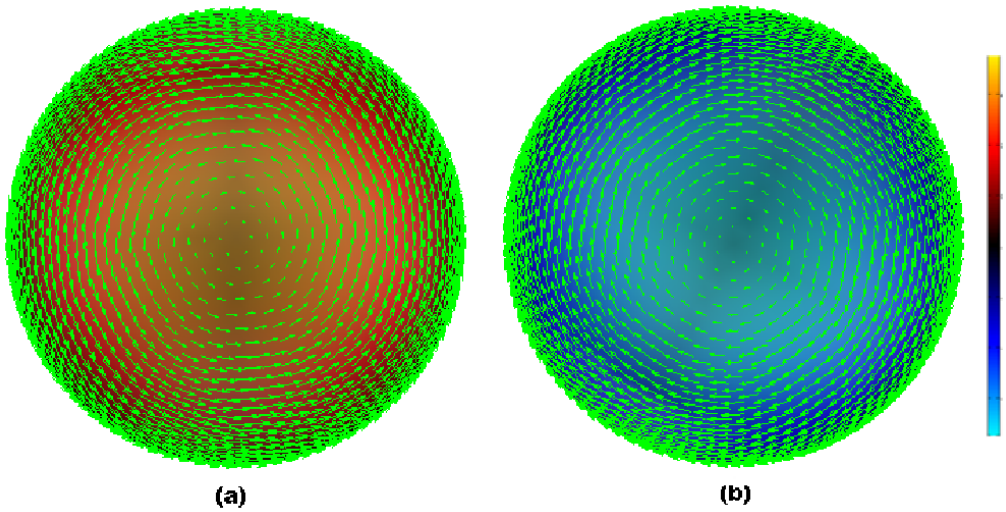

Figure 33: (a) Counterclockwise vortex vector field overlap with A on spherical manifold. (b) Clockwise vortex vector field overlap with A.

To detect traveling object on a Riemannian surface, one has to detect vectors with highest norms in the vector field $\mathbf{H}$ and thus one is able to follow the path of the moving object. This ability of HHD will be demonstrated in Figure 36.

Simulations and results

In order to test the new framework, we evaluate its performance in real and simulated environments on four types of Riemannian manifolds (rabbit, elephant, sphere and human brain).

First, we evaluate this methodology in detecting sources and sinks on the surface of a bunny mesh. In this test bench, first we generate a vector field with sources and sinks which mimic the optical flow of objects of increasing and decreasing in size. Secondly we generate rotating vector fields which mimic the optical flow of a tornado. We then performed HHD on these vector fields.

In Figure 34 (a), A on the surface of the rabbit is represented in color, while arrows in green represent the vector field. It is clearly visible in the figure that our framework identified vortices of the vector field. In Figure 34 (b), U on the surface of the rabbit is represented in color.

Our framework reveals sources and sinks of the vector field, as shown by this figure. The source is represented in blue while sink is in red. In Figure 34 (c) and Figure 34 (d), rotating and diverging vector fields are shown, and their corresponding A and U components are shown in colors on the surface.

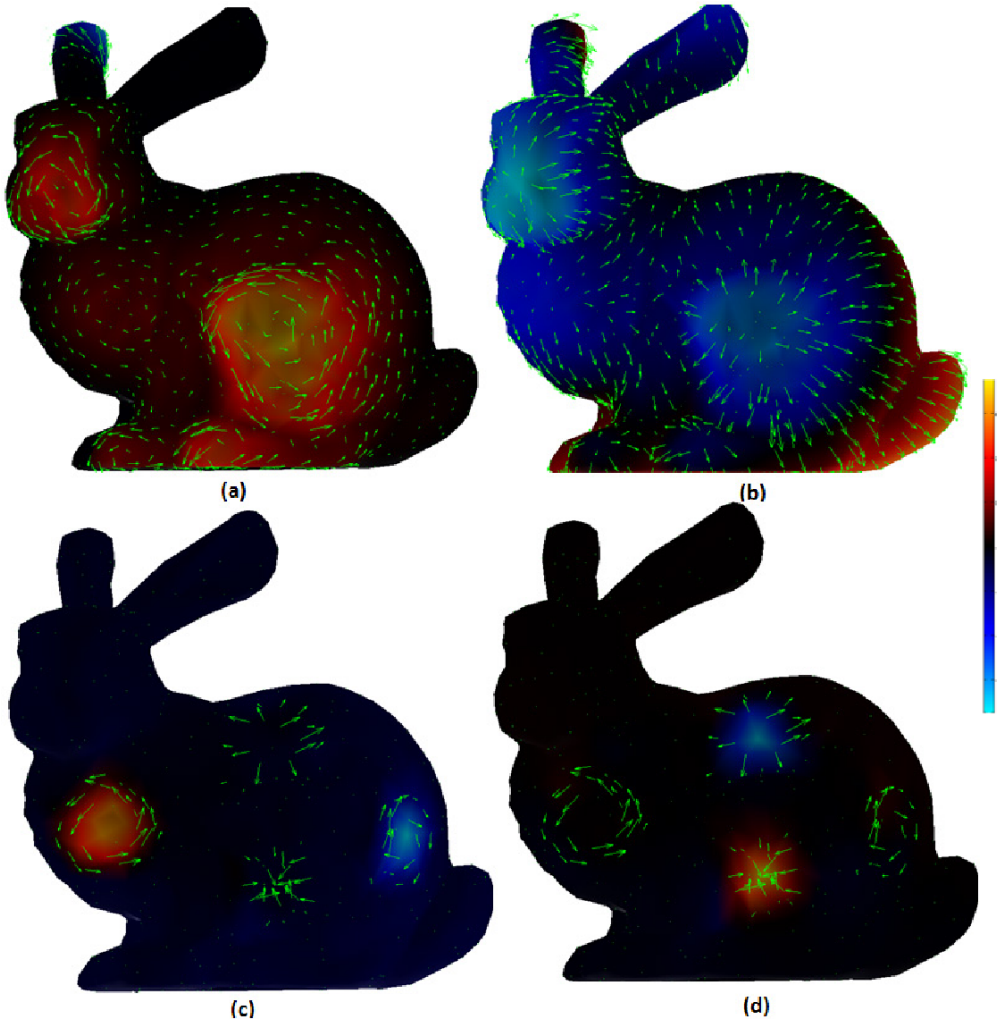

Figure 34: Examples of different types of vector field and their U and A components. (a) Rotating vector field and its A component; (b) Diverging vector field and its U component; (c) Rotating and diverging vector field and its A component; (d) Rotating and diverging vector field and its U component.

HHD decomposition is shown on the surface of an elephant object. In Figure 35, vector fields containing both rotating and diverging components are shown. It is clearly seen in Figure 35 (b) that HHD detects the source (minima of U), sink (maxima of U), clockwise vortex (minima of A) and counter clockwise vortex (maxima of A).

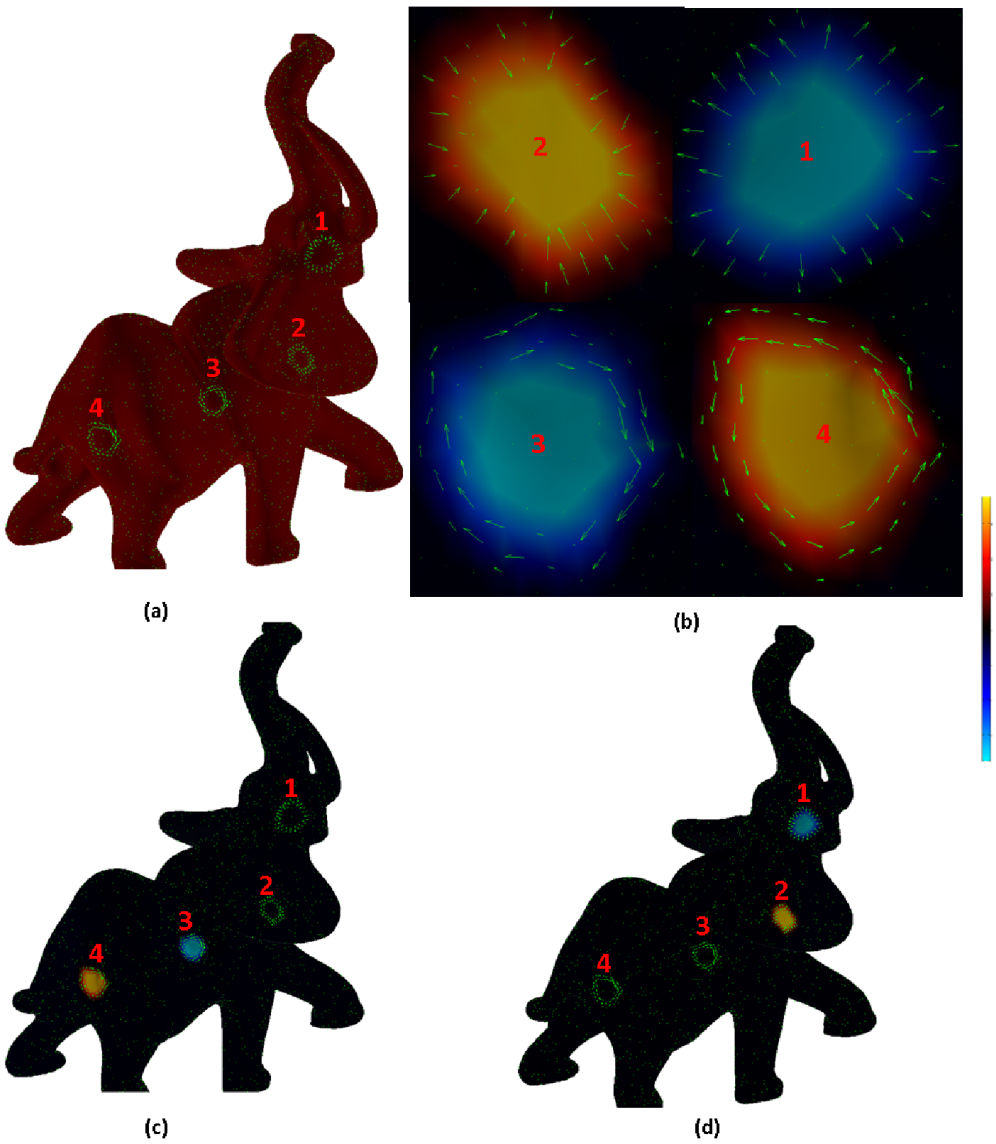

Figure 35: Vector field and its U and A components; (a) Vector field on elephant surface; (b) Close-up view of vector field with U and A superimposed; (c) Rotating vector field detected by A Component; (d) Diverging vector field identified by U.

In a second set of simulations, we first tracked a source and vortex on the surface of a rabbit object by finding critical points of scalar fields U and A, as shown in Figure 36 (a). Secondly, we tracked a constant intensity patch, which is moving according to the advection equation [59] by tracking highest norm vector

in vector field **H**, as shown in Figure 36.

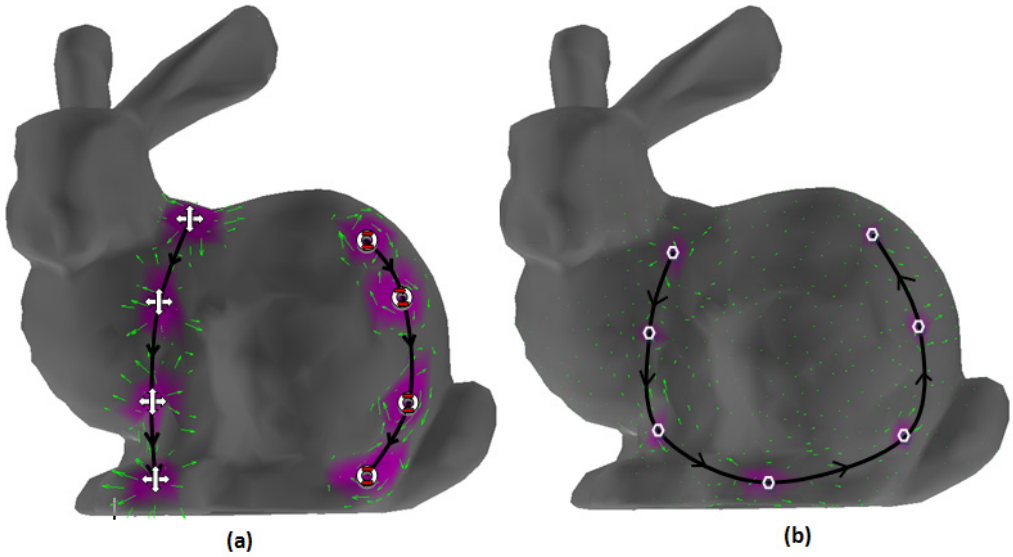

Figure 36: Tracking of Sink, vortex and constant intensity patch on the surface of a rabbit. Symbols have been assigned for source vortex and constant intensity patch while arrows show the track, and snapshots of tracking are superimposed in figures; (a) Tracking of complete paths of a source and a vortex; (b) Tracking of a complete path of constant intensity.

We further tested the HHD in a real scenario using experimental MEG data. We first obtained the optical flow from MEG source images representing motion fields of neural current on the surface of the brain and then applied HHD to detect sources and sinks.

As the majority of the neural electrical activity is predominantly diverging, we present results for the U part only in Figure 37, which shows a diverging source in the primary somatosensory part of the brain, which is clearly related to the somatosensory experiment (brain response to the electrical impulse on the finger) undertaken to get this data.

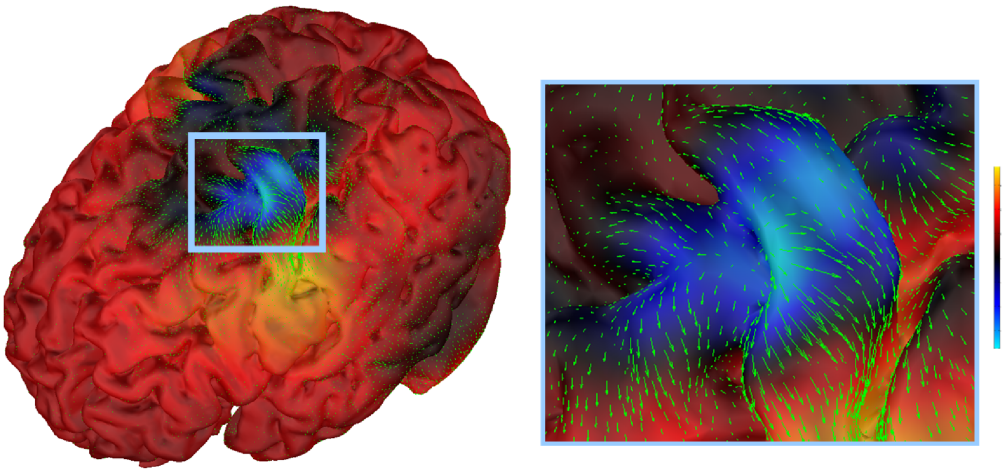

(a) (b)

Figure 37: (a) U component of HHD on the surface of the brain; (b) Zoom view of activation.

Conclusion

In this chapter, we have developed a framework for the decomposition of a vector field on 2-Riemannian manifolds. The computations involved are simple, and took less than 2 seconds to compute all HHD components for 1500 node tessellation on a conventional workstation. Evaluation of this framework under real and stimulated environments were presented.

In the next chapter, applications of HHD in functional and structural brain imaging will be suggested.

Part 4

HHD IN PRACTICE

Applications of HHD

Introduction

In the subsequent sections of this chapter we will present several applications of HHD in structural and functional brain imaging. We start from the decomposition of data from a study in different feature sets. Then we show the ability of HHD in characterizing epileptic activity. We also present how divergence representation is different from normal current density. Lastly, we present two examples of HHD in structural brain imaging: Firstly, we detect growth seeds in the neonate brain and secondly, we characterize brain tumor growth. In the following applications, we will also apply HHD on Electrocorticography(ECoG) data so before proceeding further, we present brief description of ECoG.

ECoG is a method in which electrodes are placed directly on the surface of the dura or of the brain. ECoG signals are composed of mixtures of local field potentials. Electrodes consist of grids or strips. Grid electrodes are arranged in an rectangular array, whereas strip electrodes are arranged along a line. A typical ECoG setup is shown in Figure 38.

In order to run HHD on ECoG grids, we first need to generate a surface representation of the recording grid, which follows the envelope of the cortex. The process of grid generation and co-ordinate alignment are explained in Appendix 1.

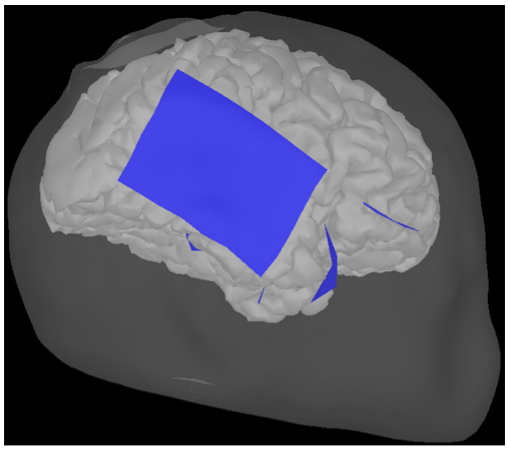

(a)

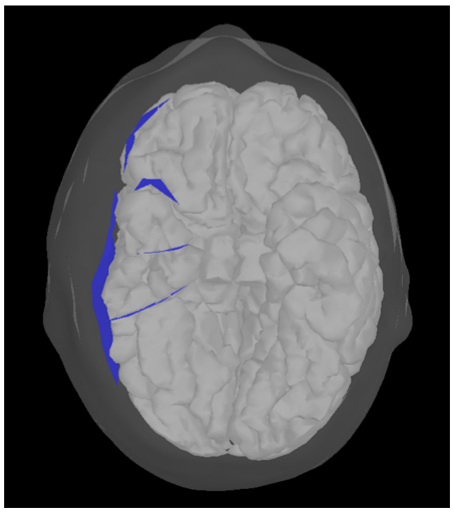

(b)

Figure 38: (a) Left view of grid and strips on a cortex; (b) Bottom view of grid and strips on a cortex.

HDD of MEG experimental data

MEG, EEG and EcOG source imaging reveal spatially-distributed and dense information contents in the temporal dimension. The extraction of patterns of interest from the data has been the expertise of clinicians and investigators but remains problematic when dealing with respect to reproducibility and expert-dependency, especially when considering the complex geometry of the cortex.

A first application of HHD aims at suggesting a principled approach to the automatic extraction of salient dynamical features from cortical activity image series, thereby facilitating the reproducible analysis of the experimental data. To illustrate this application of HHD, we used a dataset from an MEG experiment that consisted in mapping the primary somatosensory response to repeated electrical stimulations of the hand fingers [71]. The trial duration was 300-ms that included a 50-ms prestimulus interval; sampling rate was 1250Hz on all 151 MEG channels (VSM/CTF MedTech).

In order to test this application we first obtained optical flow from the minimum-norm source estimates we used them to calculate optical flow of neural currents on the surface of the brain. HHD of this optical flow was applied to detect sources and sink. As the majority of the neural electrical activity is predominantly diverging, and travelling, we present results for the U and H HHD parts only in Figure 37, which shows diverging sources and travelling objects in the primary somatosensory part of the brain.

In Figure 39, we extracted features of the cortical current activity between 30ms and 45 ms after stimulus delivery for the compact representation of electrophysiological patterns in the data.

The current activity during this period is decomposed in only three features: two sources and one travelling object. Hence we obtain a compact representation of cortical activity during the early somatosensory activity.

The computations involved took less than 5 minutes over the $55,000$ nodes of a cortex mesh using a conventional desktop computer running Matlab.

The results for this application are presented in [58].

Characterizing epileptic activity

In the second set of applications, we will present the automatic characterization of epileptic activity using HHD using ECoG and MEG.

This application of HHD finds its roots from typical flow dynamic problems.

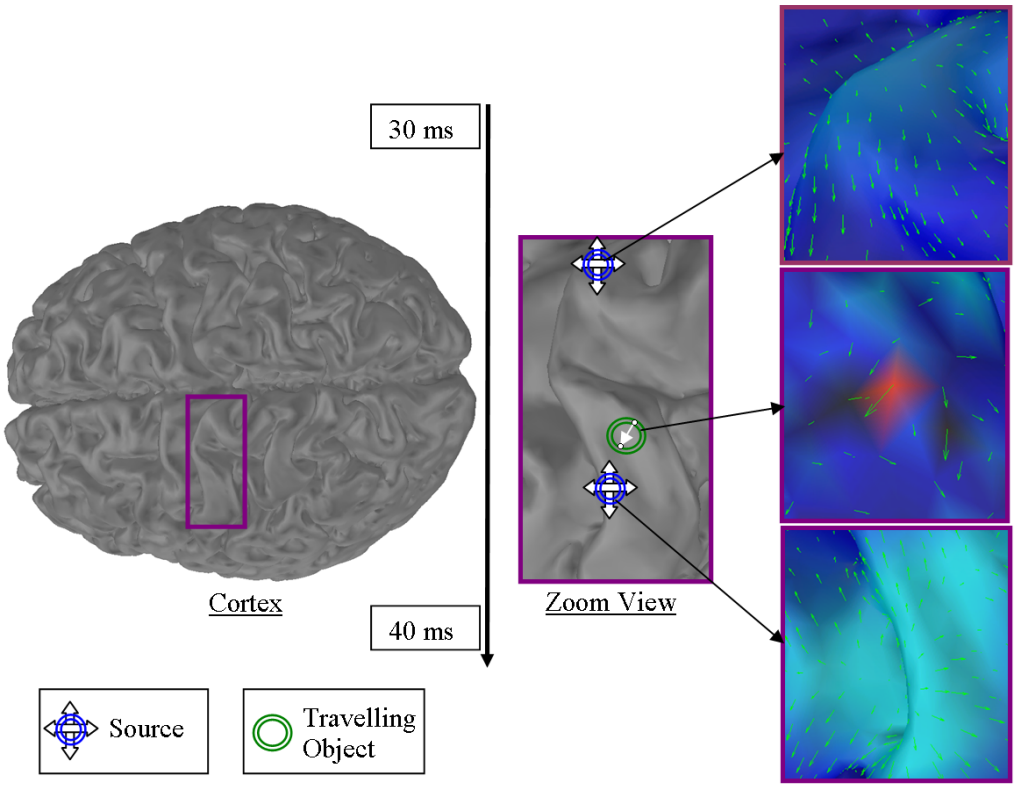

Figure 39: Decomposition of cortical activity in feature sets.

The vast amount of motion flow data has to be processed in such a way that important flow features can be automatically detected. In ECoG/MEG during epilepsy study, we face the same problem and an automatic mechanism is needed to detect important features in epileptic data, *e.g.*: spikes and seizure onsets.

Let us first emphasize how a divergence representation of a current density is different from the original current density. In comparison to current density, its divergent U component yields a more focal and compact representation of the cortical activity due to the fact that U is sensitive only to sources or sinks in the current density.

A focal and compact representation of epileptic activity can be used in identifying and localizing the epileptic foci.

Figure 40 shows comparison between two types of representation. Figure 40(a) shows divergence representation side by side with a normal cortical current

activity. It is clear that divergence representation is very focal and can easily indicate the epileptic foci.

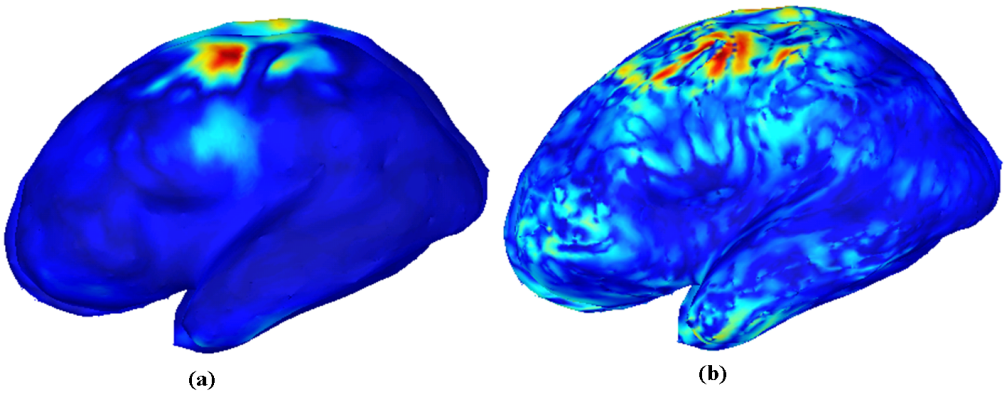

Figure 40: (a) Divergence on a cortex during epileptic spikes; (b) Current density on a cortex during epileptic spikes.

High divergence in the cortical current activity can characterize an epileptic activity since it can easily be represented by sources and sinks.
Another important parameter we use is Kinetic Energy (KE) of a vector field and it is defined as:

$$KE(t) = \int_{\mathcal{M}} \|(V)\|^2 \, d\mathcal{M}. \tag{108}$$

Characterizing of epileptic activity in ECoG

For HHD application on ECoG we used electrode data provided by Dr. M. Raghavan (MCW Neurology). In total, 64 electrodes are placed on the right motor-somatosensory cortex. Sampling rate for was set at 1 KHz. CT scans were acquired to localize the electrodes and were aligned with the post-surgical MRI image volume.

The result of the application of HHD on ECoG is summarized in Figure 41. An epileptic spike is detected in time through maximum in KE of diverging component $V_{div} = \nabla_{\mathcal{M}} U$ of optical flow $\mathbf{V}$. Figure 41(a) shows the kinetic energy. For

spatial localization of the epileptic spike, we seek singularities in diverging U component of HHD at the time instants detected through KE. In Figures 41 (b) and (c), the diverging component U is shown on the surface of the grid. The sources and sink represent points of high divergence in the data and indicate the epileptic network causing epileptic activity. These results for this epileptic network was subsequently confirmed by the neurologist.

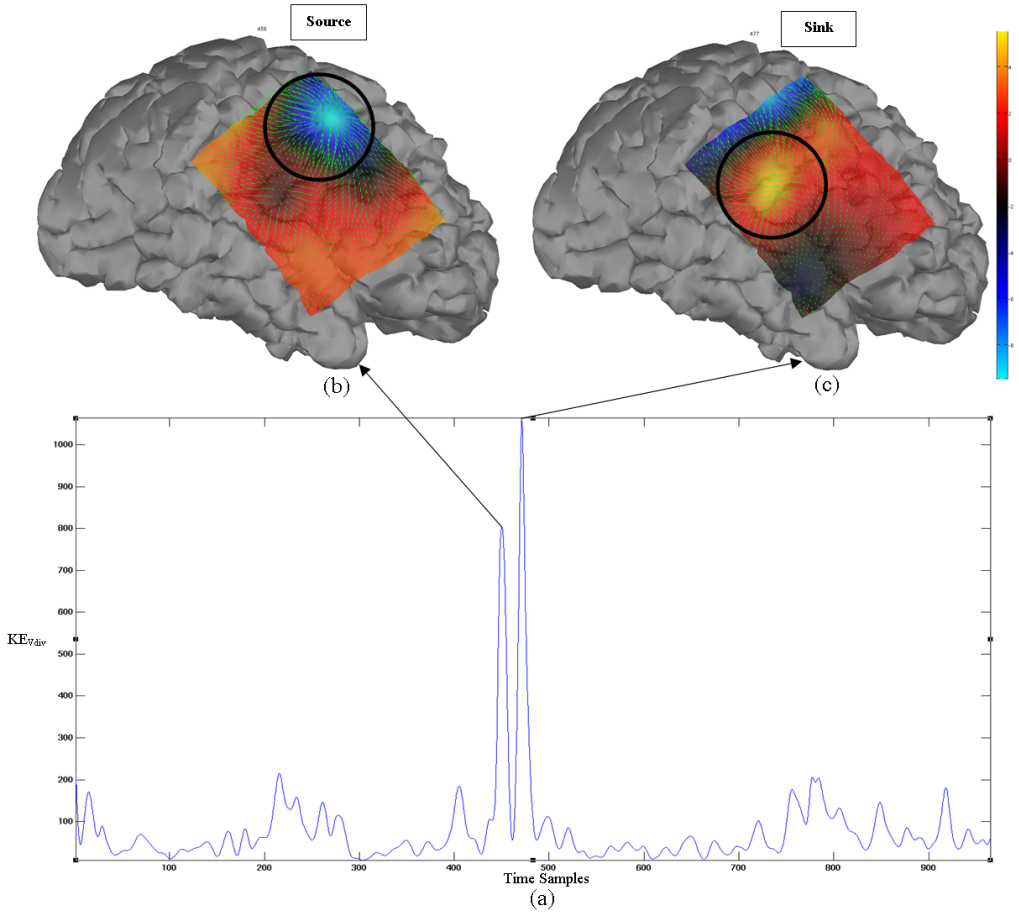

Figure 41: (a) Kinetic energy diverging component of optical flow; (b) HHD source on the ECoG grid; (c) HHD sink on the ECoG grid.

Characterizing epileptic activity with MEG source imaging

We used a dataset containing a rare occurrence of seizure during MEG recording.

We first calculate the Kinetic energy (KE) $V_{div} = \nabla_{\mathcal{M}} U$ on the optical flow vector field of the minimum-norm estimate of cortical currents. The highest peak in KE as shown in Figure 42 (b) correctly points at the start of the epileptic seizure. Figures 42 (a), (d) and (c) show magnetic fields recorded at the left occipital region, telling the story of the seizure. Seizure starts with a high frequency oscillatory (HFO) burst (Figure 42 (d)) and moves later to a continuous buzzing mode, as shown in Figure 42 (c).

To correctly characterize the epileptic network, we focussed the analysis on the start of the seizure. In Figures 41 (e) and (f), the diverging component U is shown in color on the surface of the cortex. Figure 42 (e) shows the source from where the actual epileptic activity started (the source is represented in blue). After 5ms, this source converted into the sink (the sink is represented in red) with a new source nearby (Figure 42 (f)). This pattern of activity, detected through HHD, characterizes the early epileptic network en route to seizure. The results for this application are presented in [58].

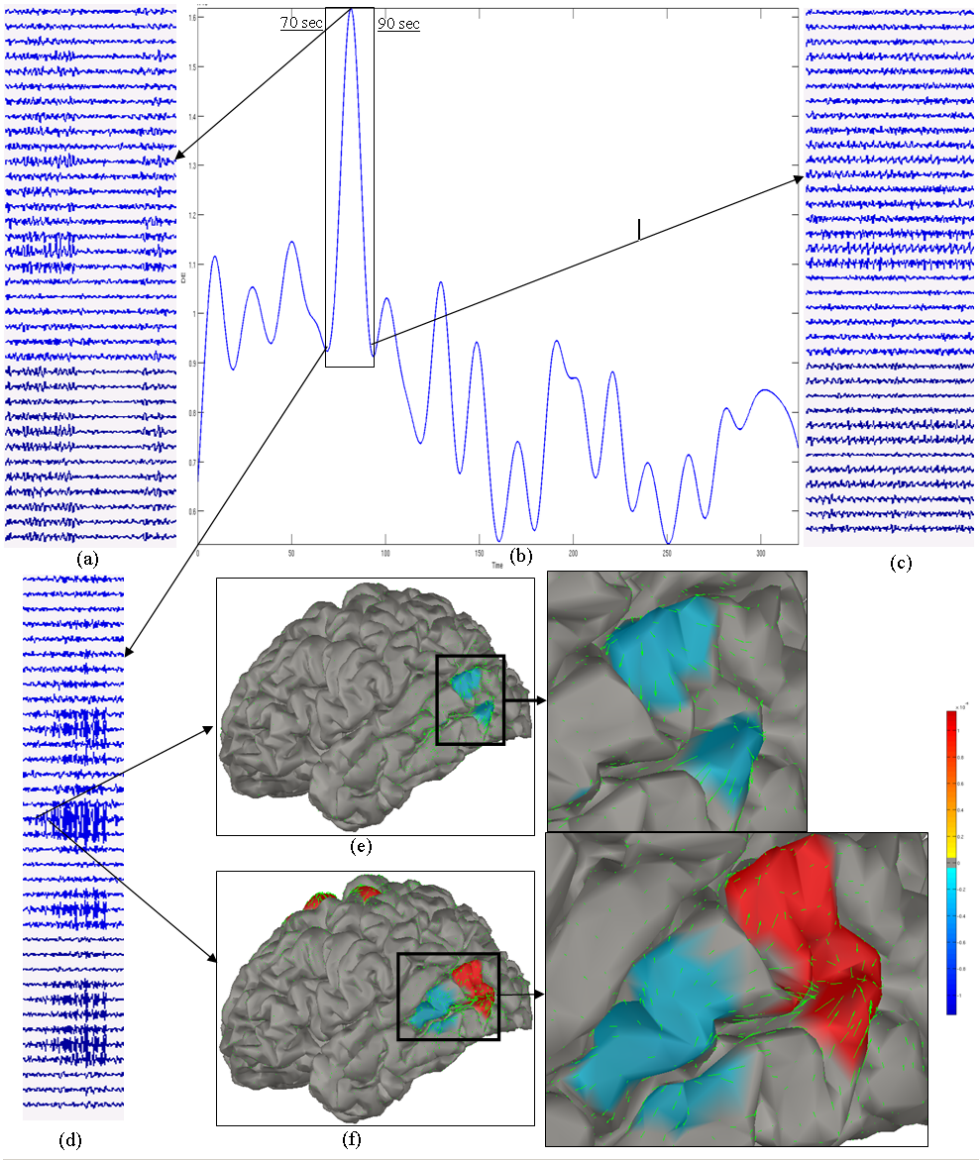

Figure 42: Epileptic seizure as seen by optical flow and HHD; (a) MEG magnetic field at left occipital region in middle of seizure; (b) KE of $V_{div} = \nabla_{\mathcal{M}} U$ during recording; (c) MEG magnetic field at left occipital region at the start of seizure; (e) Epileptic source in blue; (f) Epileptic source (in blue) and sink (in red).

Identification of cortical development in the neonate brain

This is a possible application of HHD to structural brain imaging. Using MRI [30] it is possible to follow precisely the ontogenesis of the cortical folding during early phases of development. Applications are numerous from the detection of potential lesions [30] to the deciphering of sulci formation processes whose physiological origins are yet not well understood [102, 99]. In this application, we report on a new framework to characterize the rapid brain development of newborns.

The set of data consists of 4 healthy newborns with 2 MRI T2 acquisitions for each at birth and around 3 weeks later. The white and gray matters are segmented through a dedicated algorithm to overcome the inhomogeneity of the contrast [63]. Once the cortical surfaces have been extracted we compute their depth maps from a geodesic distance of the surface to a binary mask of the brain.

Then for each subject we registered the less mature cortical surface on the more mature one and interpolate the depth maps by a nearest neighbors method [12]. We obtained therefore two depth maps, in red on Figure 43, projected on the same surface at two different time steps so it is possible to track the evolution of those maps. For this, we computed a displacement field estimated by a surface

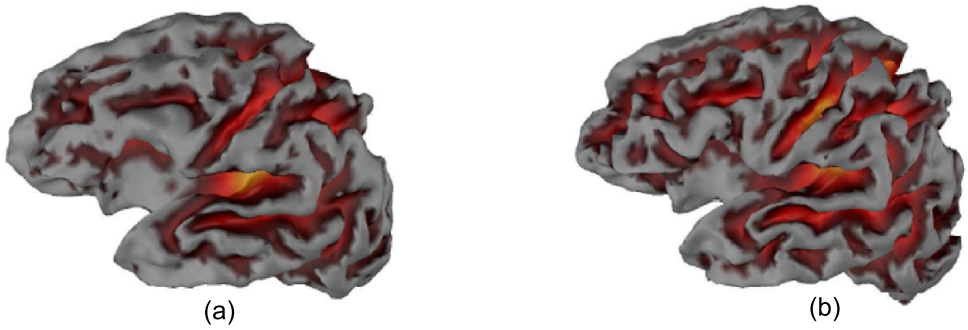

Figure 43: (a) Less mature cortical surface; (b) More mature cortical surface.

optical flow method exposed in part 3 of this thesis. This displacement field, in

green on Figure 44, reflected local evolution of sulci directly on the cortical surface (smoothed out here for a better visualization).

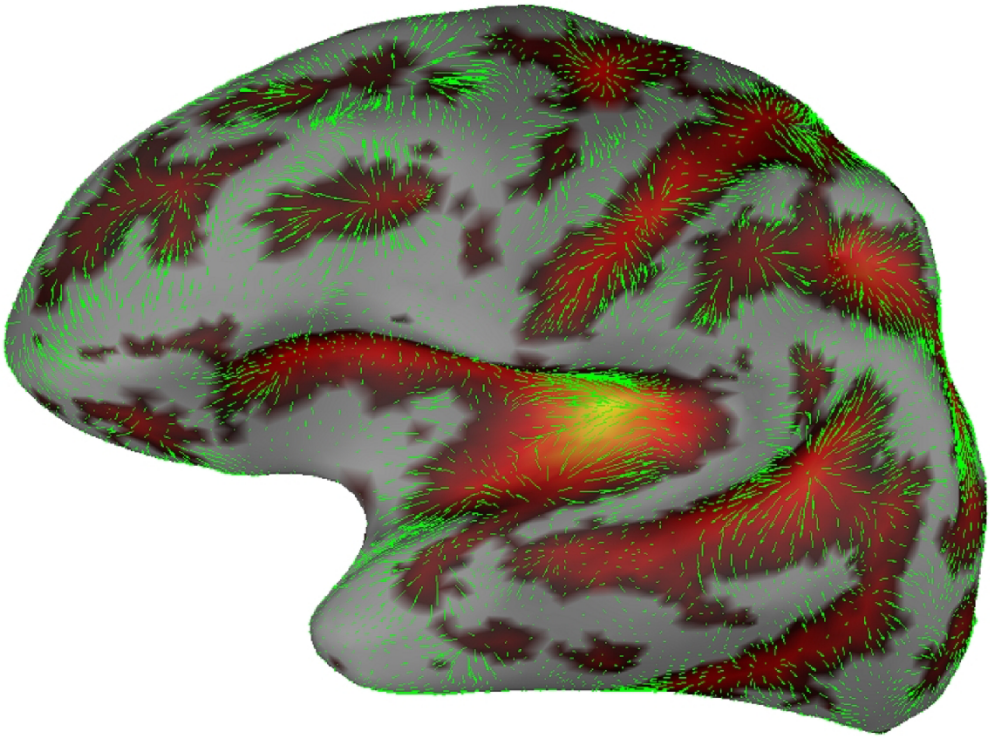

Figure 44: Surface optical flow method accounting for the displacement field between two cortical surfaces.

We further detected the critical points of the displacement field, *i.e.*: locations of points with high divergence using HHD. Minima of scalar divergence U potential, revealed putative sources of fundamental folding during the developmental process. We can see qualitatively on Figure 44 the radial structure of the vector field in green. More quantitatively, Figure 45 reveals sources points in yellow (minima of the U in red/blue) of the displacement field. The sources can be viewed as growth seeds or in other terms points around which the sulcal growth organizes itself. We show the reproducibility of these growth seeds on Figure 46 where the colors of the points correspond to 4 different neonates surfaces, registered on the same template [9]. The numbers can be linked to a sulcal roots taxonomy that we can find in the literature [87].

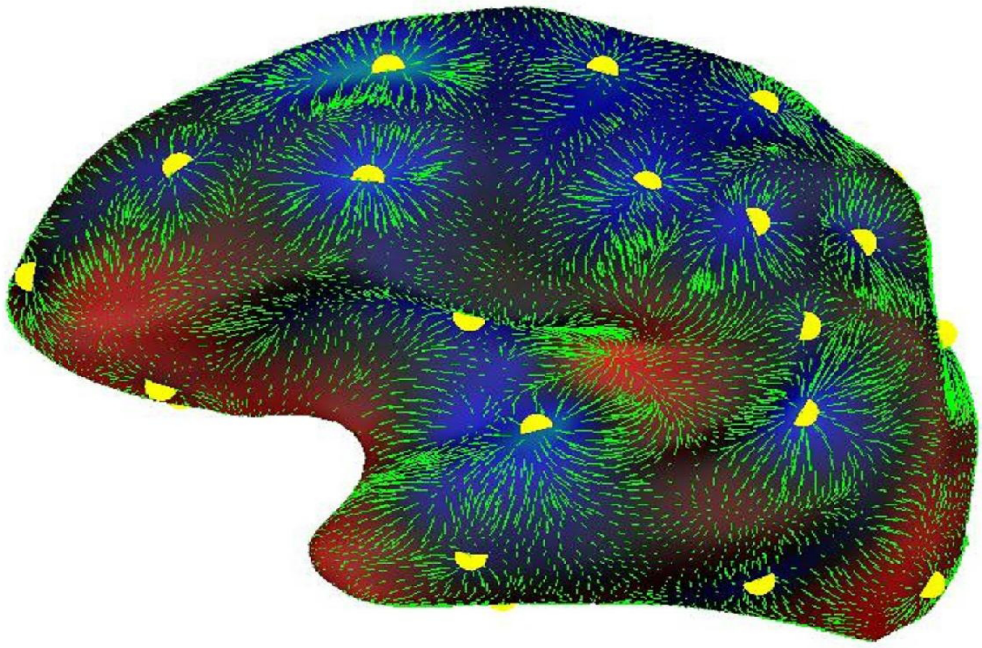

Figure 45: Detection of growth seed through scalar divergence U of HHD.

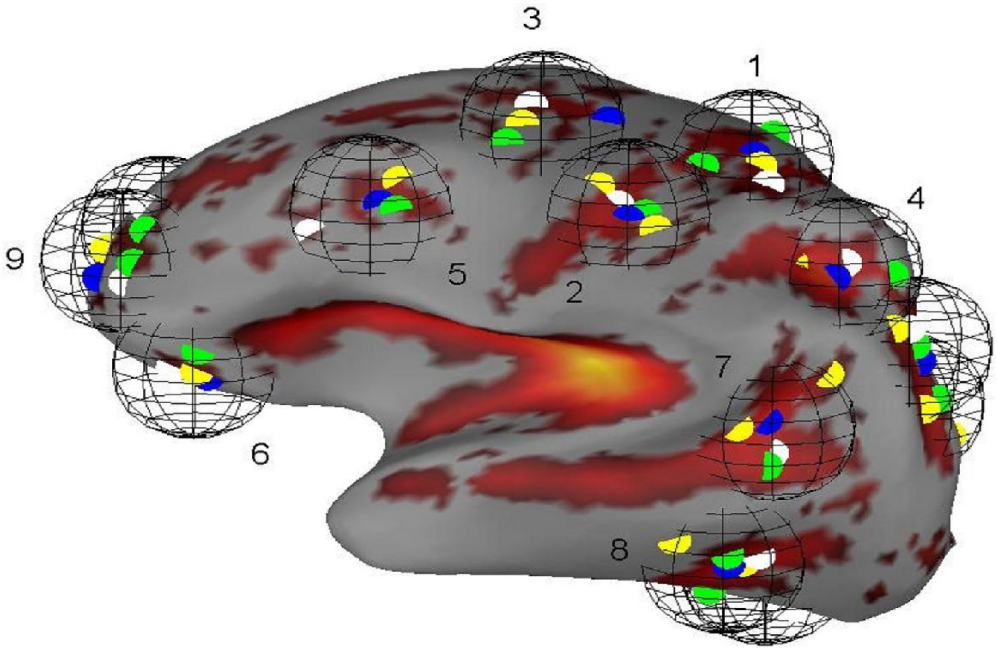

Figure 46: The reproducibility of these growth seeds in four subjects.

The main originality of this application is the use of the Helmholtz decomposition to characterize the brain folding of human newborns. We can note a good reproducibility of these growth centers or growth seeds among 4 neonates. We hypothesize a possible link between this new concept and the "sulcal roots" [87] or sulcal pits [66] proposed to explain the variability of human brain anatomy.

The results for this application were published in [60, 61].

Characterizing tumor growth patterns

Primary brain tumors include any tumor that starts in the brain. Tumors may be confined to a small area, invasive (spread to nearby areas), benign (not cancerous), or malignant (cancerous).

In the last application of HHD, we focus on characterizing growth pattern of invasive brain tumors. Here we used simple two-dimensional version of HHD to show a proof of concept but it can be evolved in full application by extracting tumor surfaces and by using the methods explained in neonate brain application, to characterize tumor growth on Riemannian manifolds.

We used two sets of FLAIR MRI images collected on two different occasions for the same tumor patient, both the MRI sequences were aligned in the same coordinate system using FSL package [94]. We also normalized the contrast of the two sets of images. We selected slice 84 on which tumor growth is most prominent on both slides (Figure 47 (a) and (b)) and computed the optical flow between these two slices (Figure 47 (c)) with arrows showing optical flow. We then computed the HHD on tumor portion of the slice; see Figure 47 (d).

In Figure 47 (e), color shown divergence component U with minima in white dots. The vector field shown here is the diverging component of optical flow $\nabla_{\mathcal{M}} U$.

It is shown that the minima of U correctly identify the growth seeds of tumor, with $\nabla_{\mathcal{M}} U$, revealing their relative spreading directions. Hence, this may be an initial block of a tool that can automatically characterize growth patterns of brain tumors.

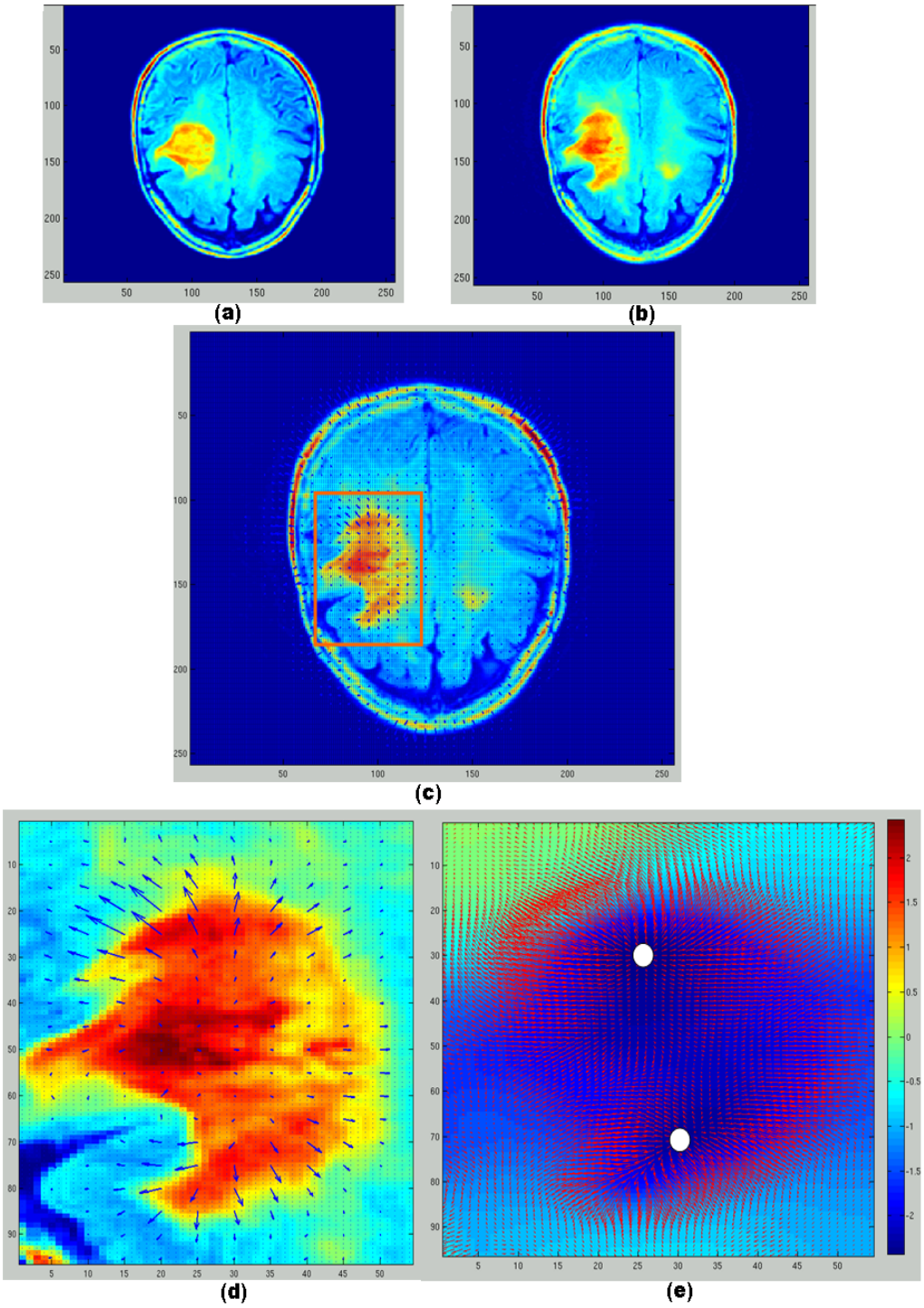

Figure 47: (a) Slice 84 of FLAIR MRI at time instant 1; (b) Slice 84 of FLAIR MRI at time instant 2; (c) Optical flow of two slices; (d) Zoom view of optical flow; (e) HHD on optical flow.

Conclusion

We have presented four applications of HHD in structural and functional brain imaging applications. The results are very encouraging and show promise HHD offers in a wide variety of applications. We believe that HHD has probably many other applications in all kind of spatiotemporal phenomena that occur in the brain.

Part 5

Conclusion & Future Actions

Conclusion and Future Actions

We introduced a new multipole moment based approach to the MEG source characterization in which we have shown that MCR can accurately characterize spatially extended neural current sources by matching current multipole moments. The procedure is based on zero-order Tikhonov regularized image but the method can be initialized using any other imaging based method.

The MCR approach solves the local imaging problem, hence reducing computational load to very large extent. Moreover, in multipole matching, we are matching only 8 moments instead of vectors equal to the dimension of the original data (the number of sensors), which for current MEG system is around 300, hence again reducing computational load. The algorithm is therefore tractable and reasonably fast (about 20sec for a 37723-node cortical tessellation).

Another important factor is the modified Gibbs priors we used for matching. Hence we may incorporate physiological information from other modalities such as PET or fMRI. By doing so, we reduced the non triviality of the electromagnetic inverse problem by restricting possible solutions.

Results from extensive Monte-Carlo simulations show excellent performances in terms of spatial characterization even for very large patches of $30cm^2$. The estimation of the surface area of active regions is very accurate, the average error in area is only $0.2cm^2$ for 2500 patches. The results for two sources show that the method reveals the repeatability of MCR.

Good results for somaesthetic data shows the method works well for real data. Using MCR we can clearly locate the somatotopy of finger responses.

The future upgrade of this method is to use magnetic multipole moments instead of current multipole moments for remapping and to compare their corresponding results. (For a detail description of the current and magnetic multipole moments see [54].)

On the MEG source dynamic characterization front, we have developed a framework for the decomposition of vector field on 2-Riemannian manifolds. The computations involved are simple and it took less than 2 seconds to compute all the HHD components for 1500 node tessellation on a conventional desktop. Evaluation of this framework under real and stimulated environment gives very encouraging results. The applications for this formulation are emerging, with more and more three-dimensional imaging evolving in real world.

Future path for this framework is its modification in discretization to higher-order finite element analysis, and its evaluation in more real world scenarios.

We have presented some applications of HHD in functional and brain imaging but we feel that HHD has more promise in biomedical imaging and more applications need to be discovered in biomedical as well as in other fields. The tumor growth characterization needs to be more mature in a way that the tumor surfaces need to be extracted and HHD is applied on them in the same spirit as in the neonate brain application.

Appendices

Grid Generation

To generate the grid on which HHD can be applied, subjects MRI and CT scan are needed. In a first step CT and MRI of subject are aligned, using FSL package [94]. After alignment we manually extract grid coordinates from the CT scan.

Grid electrodes are very coarse and electrode positions need to be detected to create dense virtual electrode systems before HHD can be applied on it. We used multidimensional scaling to interpolate between electrode positions and VORONOI diagram is then used to generate the interpolated surface which follows the cortical envelope and on which virtual electrodes are located (see figure 48).

To interpolate between potential values for the virtual electrodes system we used an interpolation scheme that is constrained by a minimal norm of the Laplacian (see [81] for details), as shown in Figure 49.

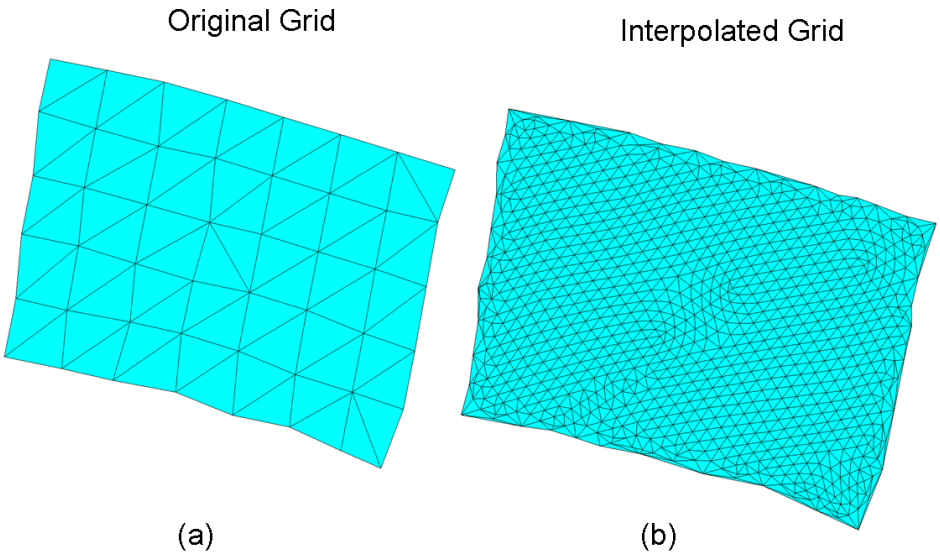

Figure 48: (a) Original grid; (b) Interpolated grid.

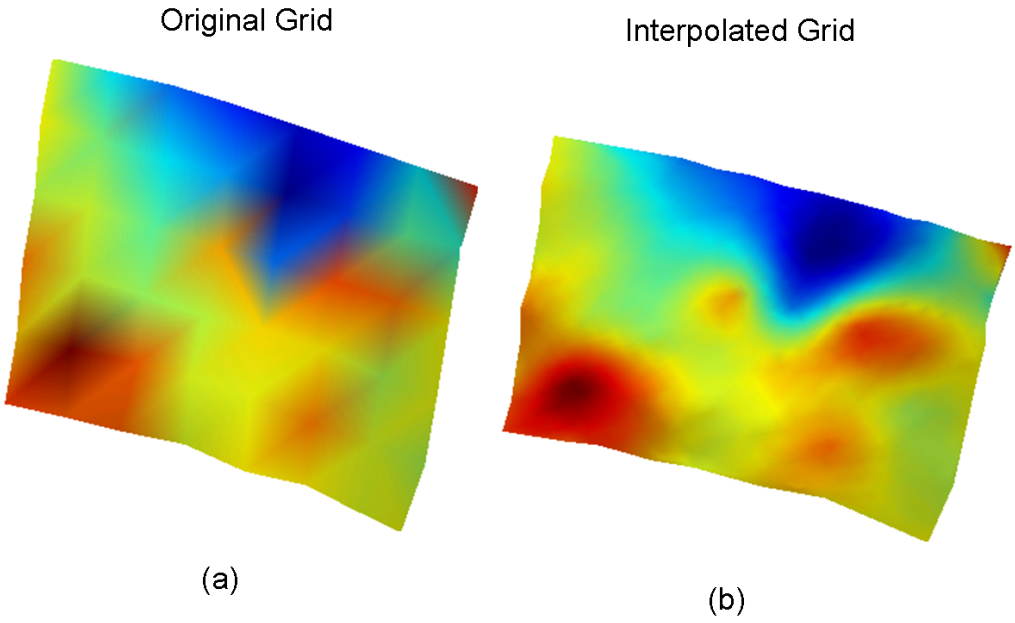

Figure 49: (a) Data on original grid; (b) Interpolated data on interpolated grid.

The cortical surface (the cortical surface is extracted from MRI using freesurfer package [20]) and interpolated grid along with strips electrode are shown in Figure 50.

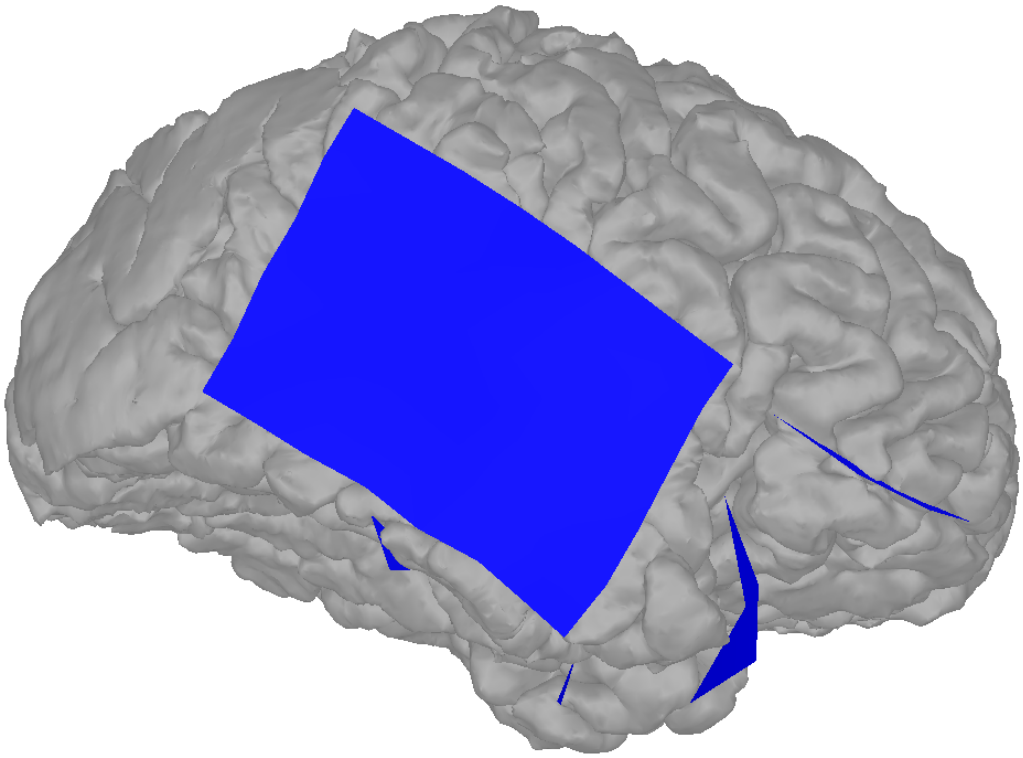

Figure 50: Overlapped interpolated grid and the cortical surface.

MEG-ECoG source localization and dynamics comparison

In this appendix we will compare MEG source localization and dynamics with ECoG.

The MEG data set that has been used for this comparison was recorded on the Elekta Neuromag 306 system at the Medical College of Wisconsin. This data is recorded at 2KHz sampling rate with 204 gradiometers and 102 magnetometers. Single sphere head model was used for forward computation minimumnorm is used for inverse modeling.

ECoG data were also recorded at the Medical College of Wisconsin. In total, 73 electrodes were placed over the frontal, parietal and temporal cortices. Sampling rate for acquisition was 1KHz. CT scans were acquired post-surgery and aligned with a presurgical MRI image volume.

The data set in both methods consisted of an epileptic HFO burst, lasting about 1s. First we will show source localization of HFO using MEG and secondly we will show source dynamics using Granger causality.

Granger causality is a statistical concept of causality that is based on prediction. According to Granger causality, if a signal $X1$ "Granger-causes" (or "G-causes") a signal $X2$, then past values of $X1$ should contain information that helps predict $X2$ above and beyond the information contained in past values of $X2$ alone. Its mathematical formulation is based on linear regression modeling of

stochastic processes [40].

Figure 51 a. shows the epileptic HFO during MEG recording. Figure 51 b. disaplys source localization for this HFO burst, when summed across whole 1s duration. This source localization reveals the bifocal nature of the epilepsy. To investigate further we extract the current density waveforms at the two epileptic foci (see figure 51 c.). We then need to understand which epileptic focus is driving other brain areas, so we estimated Granger causality between these regions, figure 51 d. which clearly reveals focus 1 is driving focus 2.

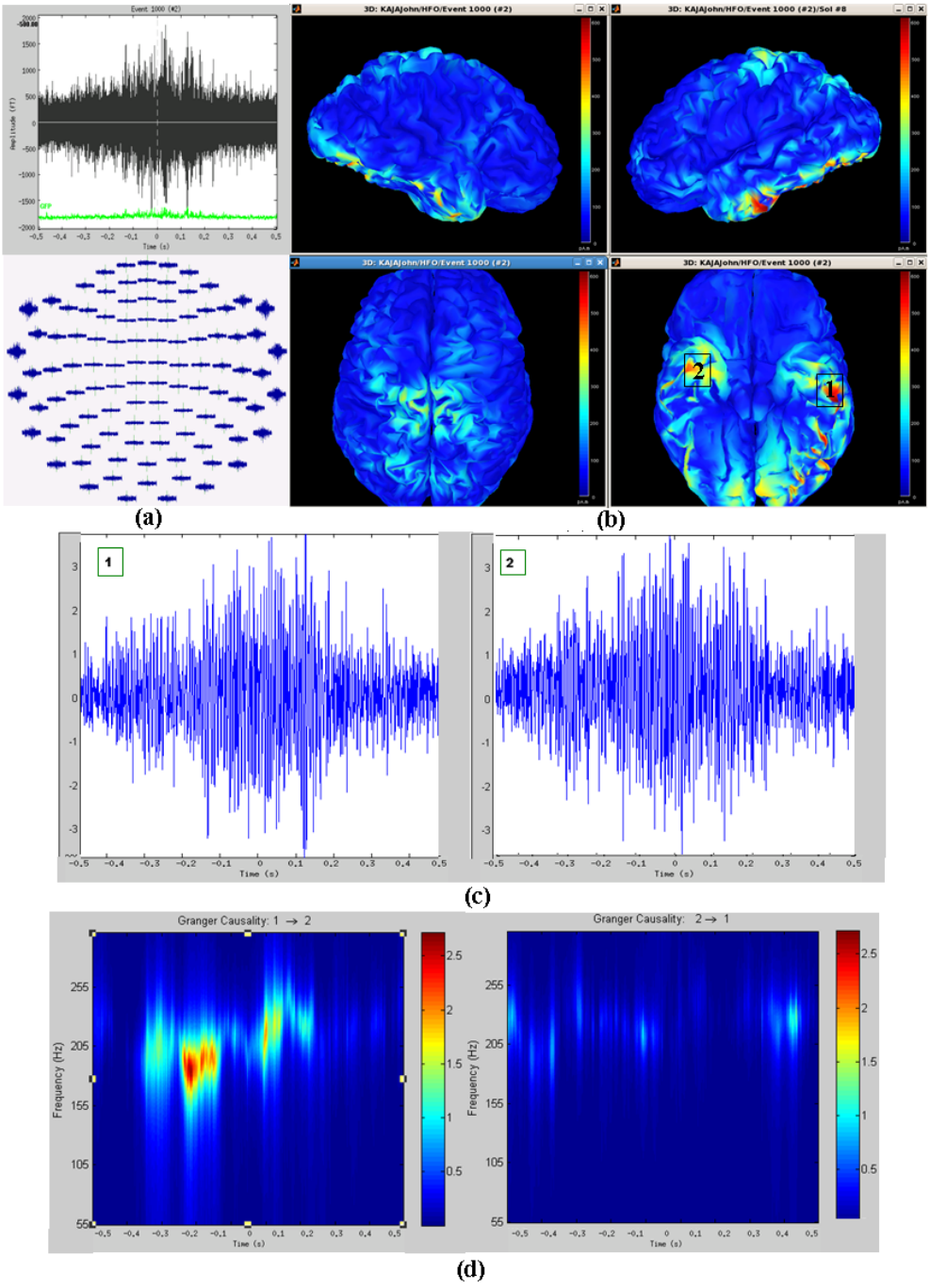

Figure 51: (a) HFO recorded during MEG recording. (b) Source localization for HFO sum across all time. (c) Current density waveform corresponding to two epileptic foci. (d) Granger causality between epileptic foci.

To confirm our MEG finding, we look at the ECoG data recorded independently. HFO burst in ECoG data were found on electrodes 36 and 72. One sample of this burst is shown in figure 52 b. We investigated the localization of these bursting electrodes, after alignment of ECoG with MRI extracted surface using the methods exposed in Appendix 1, we found that they were located above the regions identified by MEG figure 52 a., which confirms MEG as an efficient for clinical investigation of epilepsy.

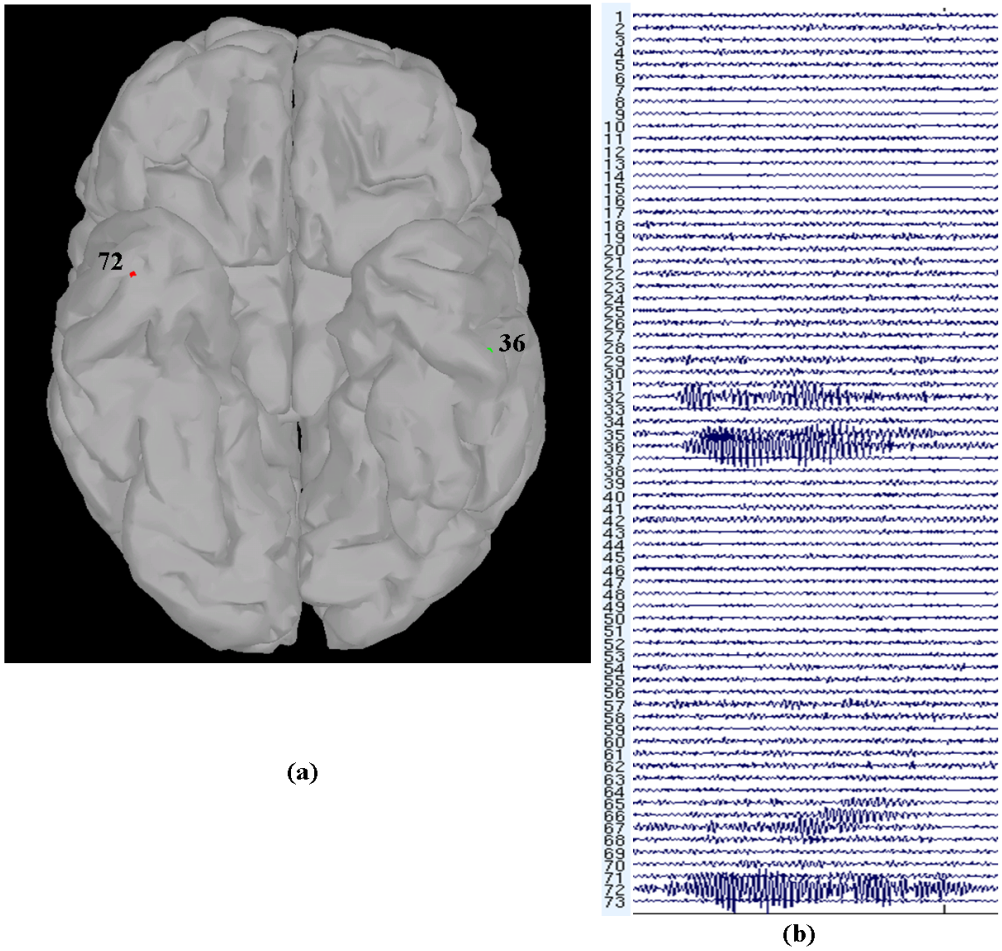

Figure 52: (a) Position of electrode 36 and 72 (b) Electric potential waveforms for ECoG electrode during epileptic HFO burst

We also computed the Granger causality between electrode 36 and 72 and results confirmed the causal relation revealed by MEG figure 53, which confirms that MEG is not only good at localizing epileptic activity but also for reveling dynamics of its activity.

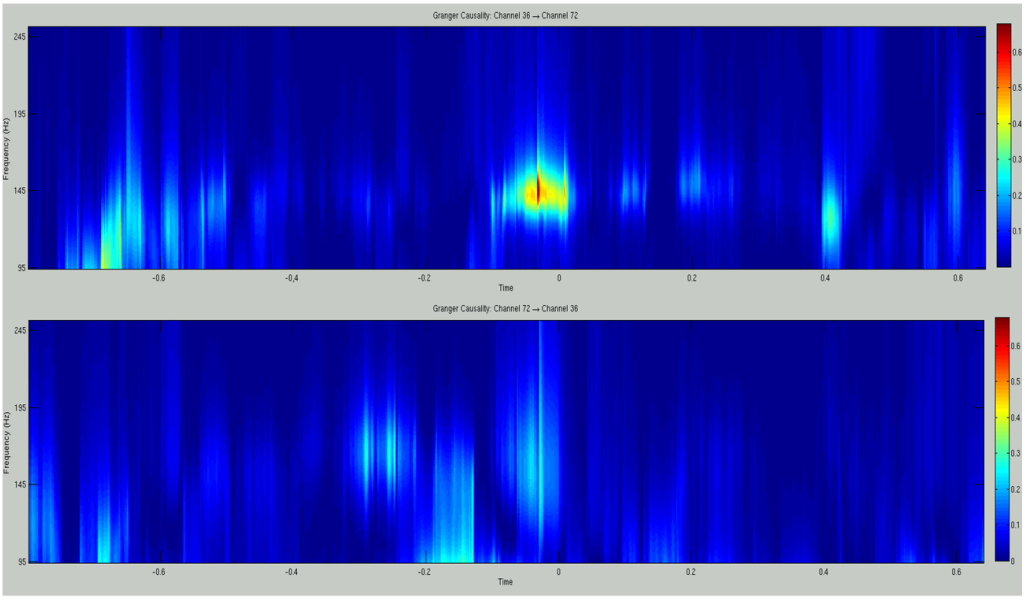

Figure 53: Granger causality between electrodes 36 and 72

Another study we did to confirm findings for this patient, was to look for slow waves under 0.1Hz. These slow waves may precede the epileptic seizure. The data was recorded using 23 channel standard montage used at Medical College of Wisconsin. Sampling rate was 200Hz. We used a 3-shell Sphere (Berg) model for forward model calculation and Brainstorm minimum-norm for inverse calculation.

The results were in agreement with MEG and ECoG. Figure 54 a. shows slow wave components preceding the epileptic seizure. An autoregressive model was used to clean blinking and heartbeat artifacts, and data was low passed at 0.1Hz. A EEG slow wave is shown in figure 54 b. We then performed source localization on this data and results were summed between 5 and 25 secs. Figure 54 c. further confirmed the results obtained from ECoG and MEG.

These slow waves were hardly been investigated in the literature, and these preliminary results may confirm their effectiveness for localizing epileptic foci.

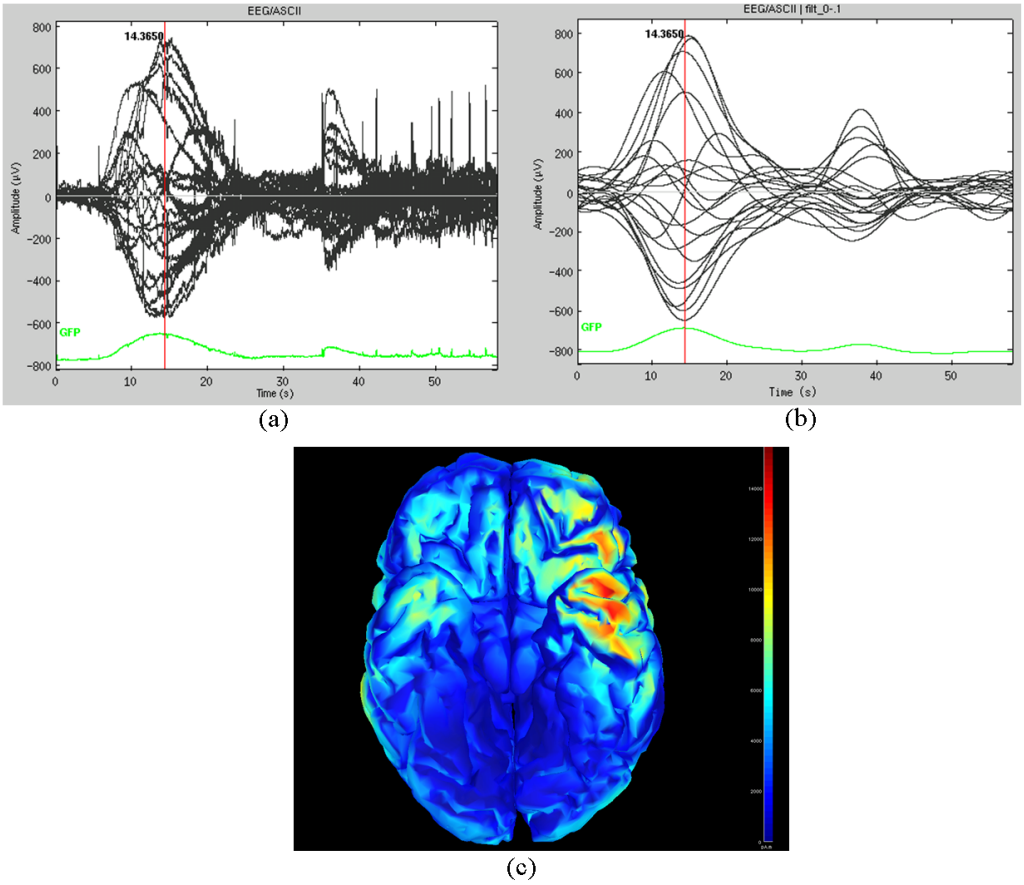

Figure 54: (a) EEG Slow wave with artifacts. (b) Clean EEG slow wave. (c) Source Localization for EEG.

Brainstorm's HHD-Opticalflow plug-in Tutorial

Sheraz KHAN

shkhan@mcw.edu

Medical College of Wisconsin-2009

This tutorial explains GUI of HHD-Opticalflow plug-in developed using Matlab. This plug-in implements the methods introduced in this thesis. HHD-Opticalflow plug-in along with Brainstorm (MEG/EEG data processing software) can be downloaded from:

http://neuroimage.usc.edu/brainstorm

1) From Brainstorm

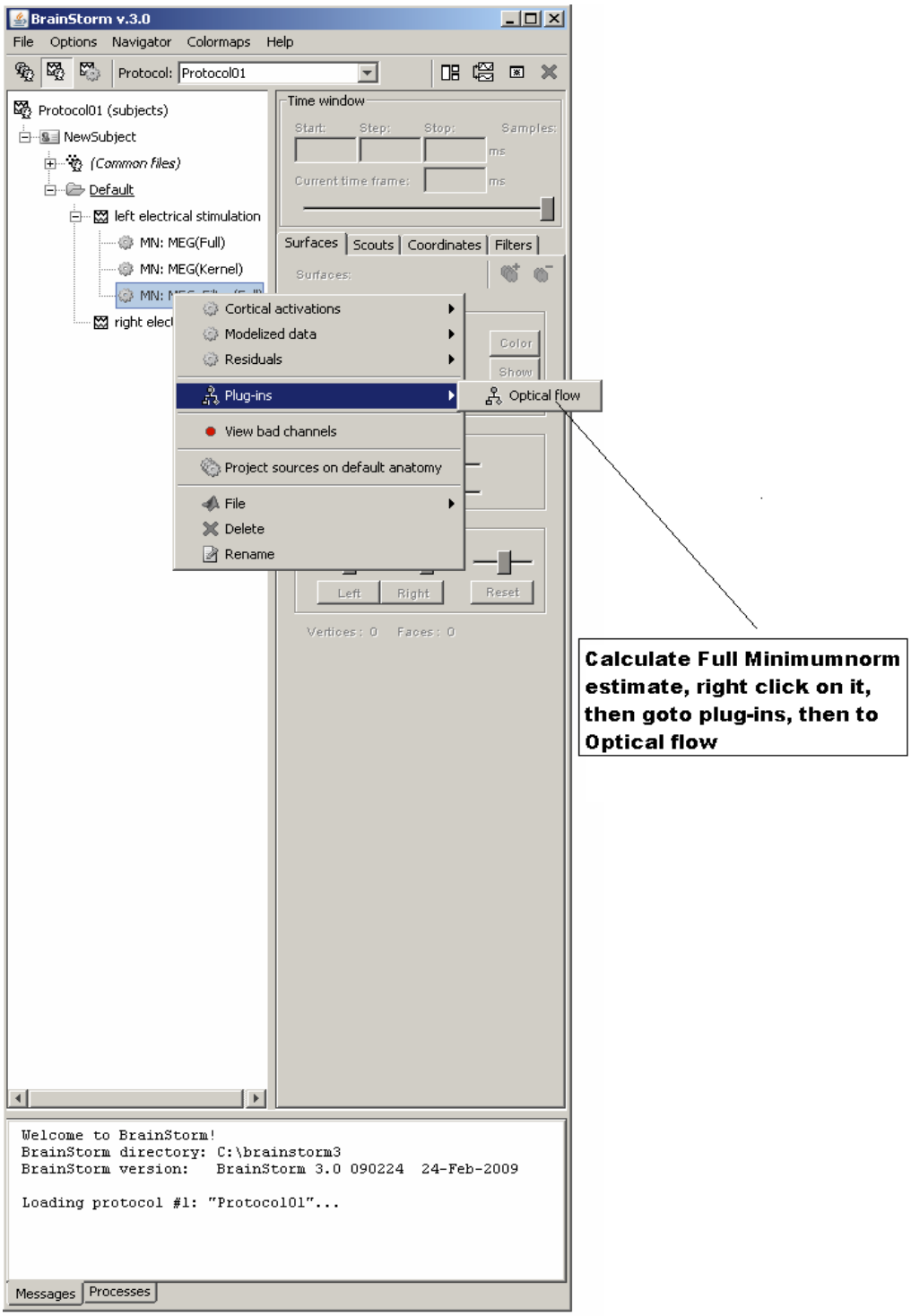

Figure 55: Launching from brainstorm

2) Plug-in GUI

When HHD-Opticalflow plug-in start, following window pops up come having three TABs, Optical Flow, HHD and Visualization, Optical flow needs to be calculated before calculating HHD.

Calculating Optical flow or HHD is memory intensive, so for large data sets, it sometimes gives error "out of memory", to resolve this there are two solutions:

1) Run brainstorm in 64 bit operating system.

2) Use less time points for calculating optical flow or HHD.

Moreover HHD and optical flow are implemented in multi-threaded fashion, so there is no progress bar, but at the end of calculation msgbox indicates end of calculations.

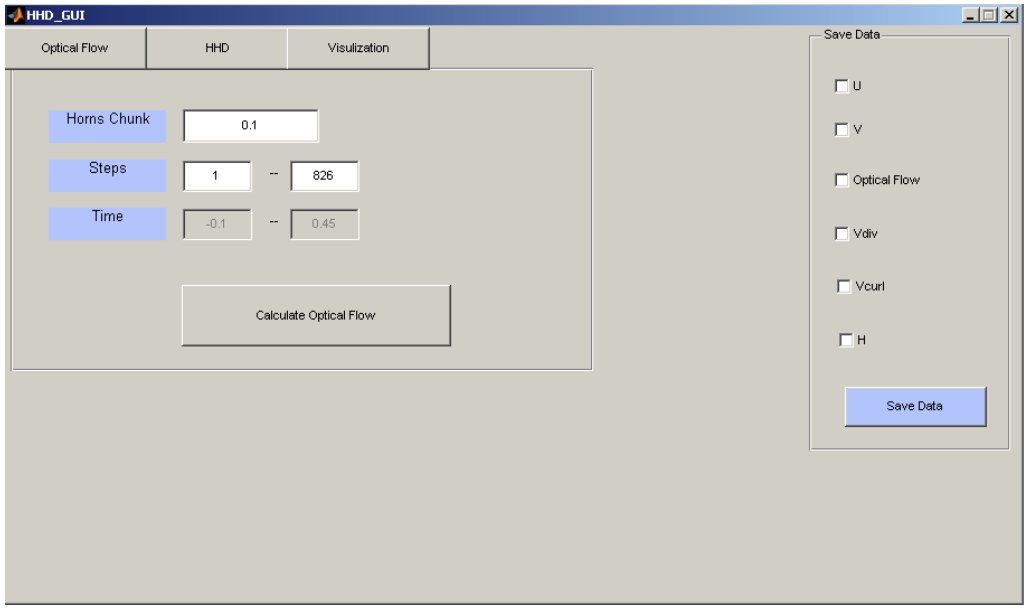

Figure 56: Plug-in GUI

3) Optical Flow Tab

Select time points on which optical flow needs to be calculated and click calculate optical flow. Save data can be used to save calculated optical flow structure.

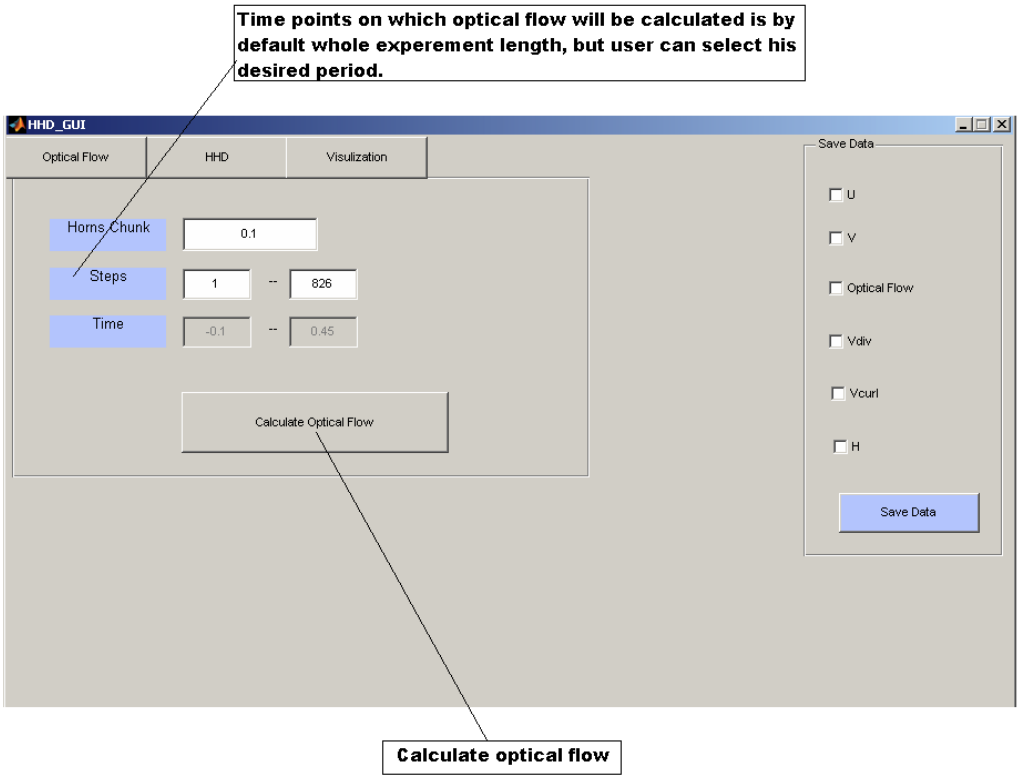

Figure 57: Optical Flow Tab

4) HHD Tab

Select time points on which HHD needs to be calculated, recursion depth sets number of times HHD is repeated, to refine Laplacian vector field (**H**) component of HHD. Save data can be used to save calculated HHD structure.

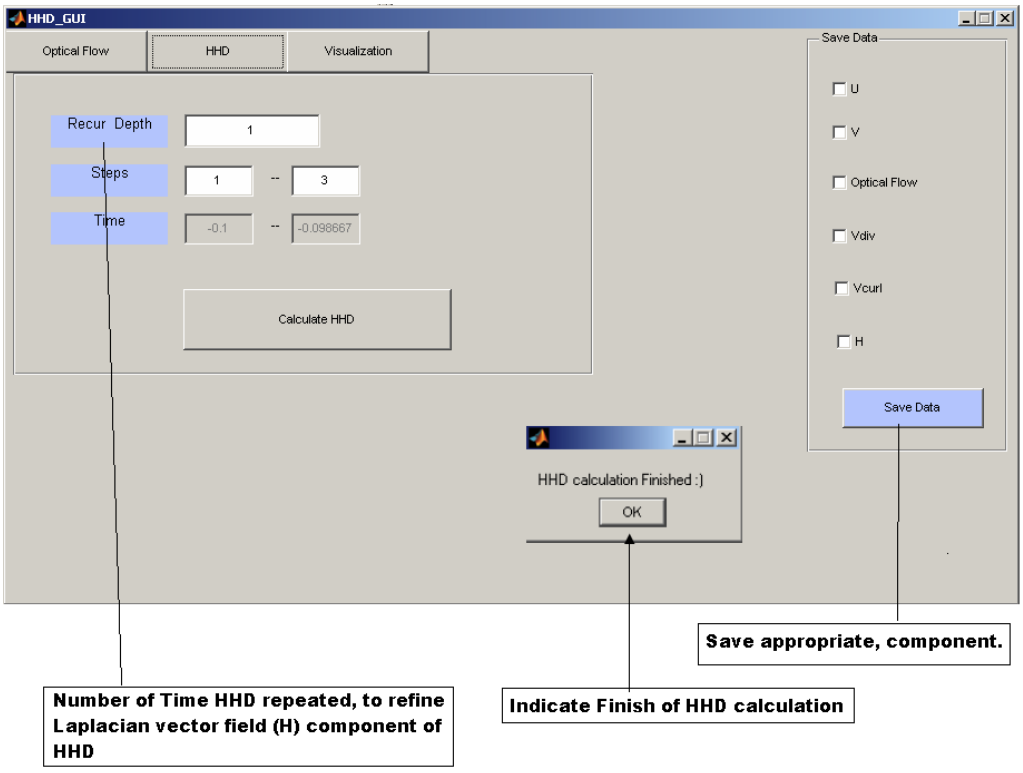

Figure 58: HHD Tab

5) Visualization Tab

Select scalar field and vector field needed to be display, browse through all the time points on which HHD and optical flow is calculated. Figure 59. shows overlapped scalar and vector fields on the cortical manifold at a single time instant.

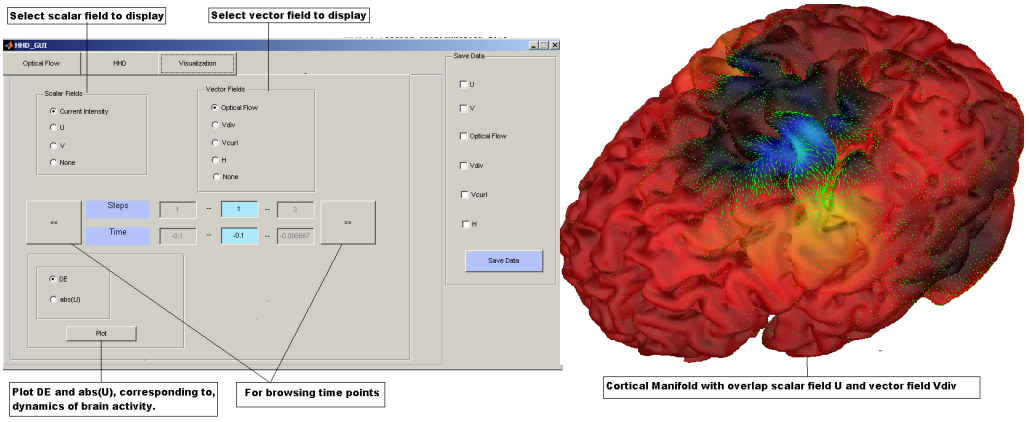

Figure 59: Visualization Tab

Bibliography

[1] I.H. Abbott and A.E. Von Doenhoff. *Theory of Wing Sections*. Dover Publications, 1959. [cited at p. 80]

[2] R. Aster, B. Borchers, and C. Thurber, editors. *Parameter Estimation and Inverse Problems*. Academic Press, 2006. [cited at p. 61]

[3] G. Aubert, R. Deriche, and P. Kornprobst. Computing optical flow via variational techniques. *SIAM Journal of Applied Mathematics*, 60(1):156–182, 1999. [cited at p. 85]

[4] T. Auranen, A. Nummenmaa, M.S. Hämäläinen, I.P. Jääskeläinen, J. Lampinen, A. Vehtari, and M. Sams. Bayesian analysis of the neuromagnetic inverse problem with l(p)-norm priors. *NeuroImage*, 26(3):870–84, 2005. [cited at p. 46]

[5] S. Baillet and L. Garnero. A Bayesian approach to introducing anatomo-functional priors in the EEG/MEG inverse problem. *IEEE Transactions on Biomedical Engineering*, 44(5):374–385, 1997. [cited at p. 33, 47]

[6] S. Baillet, L. Garnero, G. Marin, and J. P. Hugonin. Combined MEG and EEG source imaging by minimization of mutual information. *IEEE Transactions on Biomedical Engineering*, 46(5):522–534, May 1999. [cited at p. 19]

[7] S. Baillet, J.C. Mosher, and R.M. Leahy. Electromagnetic brain mapping. *IEEE Signal Processing Magazine*, 18:14–30, 2001. [cited at p. 23]

[8] H. Berger. Uber das elektrenkephalogramm des menschen. *Arch Psychiatr Nervenkr*, 87:527–570, 1929. [cited at p. 15]

[9] P.J. Besl and H.D. McKay. A method for registration of 3-D shapes. *IEEE Transactions on pattern analysis and machine intelligence*, 14(2):239–256, 1992. [cited at p. 111]

[10] Alain Bossavit. Whitney forms : a class of finite elements for three-dimensional computations in electromagnetism. *IEE Proceedings*, 135, Part A(8):493–500, November 1988. [cited at p. 83]

[11] JB Bronzan. The magnetic scalar potential. *American Journal of Physics*, 39:1357, 1971. [cited at p. 57]

[12] P. Cachier, E. Bardinet, D. Dormont, X. Pennec, and N. Ayache. Iconic feature based nonrigid registration: the PASHA algorithm. *Computer vision and image understanding*, 89(2-3):272–298, 2003. [cited at p. 109]

[13] R. Chellappa and A. Jain. *Markov random fields. Theory and application.* 1993. [cited at p. 42]

[14] CJS Clarke. Probabilistic methods in a biomagnetic inverse problem. *Inverse Problems*, 5:999–1012, 1989. [cited at p. 41]

[15] D. Cohen, E.A. Edelsack, and J.E. Zimmerman. Magnetocardiograms taken inside a shielded room with a superconducting point-contact magnetometer. *Applied Physics Letters*, 16:278, 1970. [cited at p. 15]

[16] Y. Cointepas, JF Mangin, L. Garnero, JB Poline, and H. Benali. BrainVISA: Software platform for visualization and analysis of multi-modality brain data. *Neuroimage*, 13(6):S98, 2001. [cited at p. 29]

[17] T. Corpetti, E. Mémin, and P. Pérez. Extraction of singular points from dense motion fields: an analytic approach. *Journal of Mathematical Imaging and Vision*, 19:175–198, 2003. [cited at p. 80]

[18] B. Cottereau, K. Jerbi, and S. Baillet. A MEG Multiresolution Model Selection Procedure Reveals the Cortical Somatotopy of Hand-Fingers. *Non-invasive Functional Source Imaging of the Brain and Heart and the International Conference on Functional Biomedical Imaging, 2007. NFSI-ICFBI 2007. Joint Meeting of the 6th International Symposium on*, pages 28–31, 2007. [cited at p. 76]

[19] B. Cottereau, K. Jerbi, and S. Baillet. Multiresolution imaging of MEG cortical sources using an explicit piecewise model. *Neuroimage*, 38(3):439–451, 2007. [cited at p. 33]

[20] A.M. Dale, B. Fischl, and M.I. Sereno. Cortical surface-based analysis I. Segmentation and surface reconstruction. *Neuroimage*, 9(2):179–194, 1999. [cited at p. 123]

[21] A.M. Dale, A.K. Liu, B.R. Fischl, R.L. Buckner, J.W. Belliveau, J.D. Lewine, and E. Halgren. Dynamic Statistical Parametric Mapping Combining fMRI and MEG for High-Resolution Imaging of Cortical Activity. *Neuron*, 26(1):55–67, 2000. [cited at p. 46]

[22] A.M. Dale and M.I. Sereno. Improved localizadon of cortical activity by combining eeg and meg with mri cortical surface reconstruction: A linear approach. *Journal of Cognitive Neuroscience*, 5(2):162–176, 1993. [cited at p. 40]

[23] F. Darvas, M. Rautiainen, D. Pantazis, S. Baillet, H. Benali, J. C. Mosher, L. Garnero, and R. M. Leahy. Investigations of dipole localization accuracy in meg using the bootstrap. *Neuroimage*, (25)2:355–368, 2005. [cited at p. 33]

[24] G. Dassios, AS Fokas, and D. Hadjiloizi. On the complementarity of electroencephalography and magnetoencephalography. *Inverse Problems*, 23(6):2541, 2007. [cited at p. 19]

[25] O. David and L. Garnero. Time-coherent expansion of eeg/meg cortical sources. *NeuroImage*, 17:1277–1289, 2002. [cited at p. 33]

[26] G. Demoment. Image reconstruction and restoration: overview of common estimation structures and problems. *IEEE Transactions on Acoustics, Speech, and Signal Processing*, 37(12):2024–2036, Dec. 1989. [cited at p. 44]

[27] T. J. Diciccio and B. Efron. Bootstrap confidence intervals. *Stat. Sci.*, 11(3):189–228, 1996. [cited at p. 72]

[28] M.P. Do Carmo. *Riemannian Geometry*. Birkhäuser, 1993. [cited at p. 81]

[29] O. Druet, E. Hebey, and Frédéric Robert. *Blow-up theory for elliptic PDEs in Riemannian geometry*, chapter Background Material, pages 1–12. Princeton University Press, Princeton, N.J., 2004. [cited at p. 85]

[30] J. Dubois, M. Benders, A. Cachia, F. Lazeyras, R. Ha-Vinh Leuchter, SV Sizonenko, C. Borradori-Tolsa, JF Mangin, and PS Huppi. Mapping the early cortical folding process in the preterm newborn brain. *Cerebral Cortex*, 18(6):1444, 2008. [cited at p. 109]

[31] J.J. Ermer, J.C. Mosher, S. Baillet, and R.M. Leahy. Rapidly recomputable EEG forward models for realistic head shapes. *Physics in Medicine and Biology*, 46(4):1265–1281, 2001. [cited at p. 30]

[32] TC Ferree, KJ Eriksen, DM Tucker, E.G. Inc, and OR Eugene. Regional head tissue conductivity estimation for improved EEG analysis. *IEEE Transactions on Biomedical Engineering*, 47(12):1584–1592, 2000. [cited at p. 30]

[33] AS Fokas. Electro–magneto-encephalography for a three-shell model: distributed current in arbitrary, spherical and ellipsoidal geometries. *Journal of The Royal Society Interface*, 6(34):479, 2009. [cited at p. 29]

[34] M. Fuchs, M. Wagner, and H.A. Wischmann. Linear and nonlinear current density reconstructions. *Journal of Clinical Neurophysiology*, 16(3):267–295, 1999. [cited at p. 46]

[35] S. Geman, D. Geman, K. Abend, TJ Harley, and LN Kanal. Stochastic relaxation, Gibbs distributions and the Bayesian restoration of images. *Journal of Applied Statistics*, 20(5):25–62, 1993. [cited at p. 47]

[36] D. B. Geselowitz. Current multipole expansion to estimate lateral extent of neuronal activity: A theoretical analysis. *IEEE Engineering in Medicine and Biology Magazine*, 12:164–168, 1965. [cited at p. 51]

[37] D. B. Geselowitz. On the magnetic field generated outside an inhomogeneous volume conductor by internal. *IEEE Transactions on Magnetics*, 6:346–347, 1970. [cited at p. 57]

[38] V. Loan G.H. Golub, editor. *Matrix Computation*. Johns Hopkins University Press, 1984. [cited at p. 69]

[39] G.H. Golub and C.F. Van Loan. *Matrix computations*. Johns Hopkins University Press Baltimore, MD, USA, 1996. [cited at p. 35]

[40] CWJ Granger. Investigating causal relations by econometric models and cross-spectral methods. *Econometrica*, 37(3):424–438, 1969. [cited at p. 126]

[41] Q. Guo, M.K. Mandal, and M.Y. Li. Efficient Hodge–Helmholtz decomposition of motion fields. *Pattern Recognition Letters*, 26(4):493–501, 2005. [cited at p. 80]

[42] Q. Guo, M.K. Mandal, G. Liu, and K.M. Kavanagh. Cardiac video analysis using Hodge–Helmholtz field decomposition. *Computers in Biology and Medicine*, 36(1):1–20, 2006. [cited at p. 80]

[43] P. Kielanowski H. Gonzalez, S. R. Juarez and M. Loewe. Multipole expansion in magnetostatics. *American Journal of Physics*, 66:228–231, 1988. [cited at p. 57]

[44] M. Hämäläinen, R. Hari, R. Ilmoniemi, J. Knuutila, and O. Lounasmaa. Magnetoencephalography: Theory, instrumentation and applications to the

noninvasive study of human brain function. *Reviews of Modern Physics.*, 65:413–497, 1993. [cited at p. 21, 22, 23, 33]

[45] P.C. Hansen. The L-curve and its use in the numerical treatment of inverse problems. *Citeseer*, 1999. [cited at p. 42]

[46] Robert M. Haralock and Linda G. Shapiro. *Computer and Robot Vision.* Addison-Wesley Longman Publishing Co., Inc., Boston, MA, USA, 1991. [cited at p. 60, 62]

[47] H. Helmholtz. Ueber einige Gesetze der Vertheilung elektrischer Strome in korperlichen Leitern mit Anwendung auf die thierisch-elektrischen Versuche. *Annalen der Physik und Chemie*, 165(6), 1853. [cited at p. 33]

[48] A.L. Hodgkin. *The conduction of the nervous impulse.* Liverpool University Press, 1971. [cited at p. 20]

[49] B.K.P. Horn and B.G. Schunck. Determining optical flow. *Artificial Intelligence*, 17:185–204, 1981. [cited at p. 84]

[50] M. Huang, CJ Aine, S. Supek, E. Best, D. Ranken, and ER Flynn. Multi-start downhill simplex method for spatio-temporal source localization in magnetoencephalography. *Electroencephalography and Clinical Neurophysiology/Evoked Potentials Section*, 108(1):32–44, 1998. [cited at p. 37]

[51] Numerical Modeling in Electro and Magnetoencephalography. *Oguz Tanzer.* PhD thesis, Helsinki University of Technology, 2006. [cited at p. 19]

[52] J. D. Jackson, editor. *Classical Electrodynamics.* New York: Wiley, 1975. [cited at p. 57]

[53] K. Jerbi, S. Baillet, and J.C. Mosher. Localisation of realistic cortical activity using current multipoles. *NeuroImage*, 22:779–793, 2004. [cited at p. 26, 58]

[54] K. Jerbi, J.C. Mosher, S. Baillet, and R.M. Leahy. On meg forward modelling using multipolar expansions. *Physics in Medicine and Biology*, 47:523–555, 2002. [cited at p. 26, 27, 58, 59, 62, 118]

[55] S. Khan. Comparative Study of Wideband Subspace Direction of Arrival (DOA) estimation methods. *The Journal of the Acoustical Society of America*, 123:3583–3584, 2008. [cited at p. 38]

[56] S. Khan, B. Cottereau, R. Leahy, J.C. Mosher, H. Ammari, and S. Baillet. A Two-step imaging procedure for MEG characterization of cortical currents: location and spatial extent. *Biomedical Imaging: Macro to Nano, 2008. 5th IEEE International Symposium on*, page in press., 2008. [cited at p. 59]

[57] S. Khan, B. Cottereau, R. Leahy, J.C. Mosher, H. Ammari, and S. Baillet. MEG Source Characterization Through Current Multipole Moments. *14th Human Brain Mapping International Conference, Melbourne*, page in press., 2008. [cited at p. 59]

[58] S. Khan, J. Lefèvre, and S. Baillet. Feature Extraction from Time-Resolved Cortical Current Maps using the Helmholtz-Hodge Decomposition. *15th Human Brain Mapping International Conference*, page in press., 2009. [cited at p. 103, 107]

[59] Julien Lefèvre and Sylvain Baillet. Optical flow and advection on 2-riemannian manifolds: a common framework. *IEEE Transactions on Pattern Analysis & Machine Intelligence*, 30(6):1081–92, June 2008. [cited at p. 80, 83, 87, 97]

[60] J. Lefèvre, S. Khan, S. Baillet, and J.F. Mangin. Helmholtz Hodge decomposition and the identification of growth seeds in the neonate brain. *15th Human Brain Mapping International Conference*, page in press., 2009. [cited at p. 112]

[61] J. Lefèvre, S. Khan, S. Baillet, and J.F. Mangin. Identification of growth seeds in the neonate brain through surfacic Helmholtz decomposition. *21st*

International Conference on Information Processing in Medical Imaging, page in press., 2009. [cited at p. 112]

[62] L. Lemieux, K. Krakow, and D.R. Fish. Comparison of spike-triggered functional MRI BOLD activation and EEG dipole model localization. *Neuroimage*, 14(5):1097–1104, 2001. [cited at p. 18]

[63] F. Leroy, J.F. Mangin, F. Rousseau, H. Glasel, L. Hertz-Pannier, J. Dubois, and G. Dehaene-Lambertz. Cortical Surface Segmentation in Infants by Coupled Surfaces Deformation across Feature Field. In *Imaging the Early Developing Brain: Challenges and Potential Impact, Workshop at MICCAI*, 2008. [cited at p. 109]

[64] A.K. Liu, J.W. Belliveau, and A.M. Dale. Spatiotemporal imaging of human brain activity using functional MRI constrained magnetoencephalography data: Monte Carlo simulations. *Proceedings of the National Academy of Sciences*, 95(15):8945–8950, 1998. [cited at p. 46]

[65] N.K. Logothetis and B.A. Wandell. Interpreting the bold signal. *Annu Rev Physiol*, 66:735–769, 2004. [cited at p. 18]

[66] G. Lohmann, D.Y. von Cramon, and A.C.F. Colchester. Deep sulcal landmarks provide an organizing framework for human cortical folding. *Cerebral Cortex*, 2007. [cited at p. 112]

[67] J. Malmivuo and R. Plonsey. *Bioelectromagnetism: principles and applications of bioelectric and biomagnetic fields.* Oxford University Press, USA, 1995. [cited at p. 54]

[68] S. Mann and A. Rockwood. Computing Singularities of 3D Vector Fields with Geometric Algebra. *Proc. IEEE Visualization*, pages 283–289, 2002. [cited at p. 92]

[69] J. Mattout, M. Pélégrini-Issac, L. Garnero, and H. Benali. Multivariate source prelocalization (msp): Use of functionally informed basis functions

for better conditionning the meg inverse problem. *NeuroImage*, 26:356–373, 2005. [cited at p. 46]

[70] J.C. Maxwell. Electricity and magnetism. *Vol*, 1:333–335, 1873. [cited at p. 23]

[71] S. Meunier, L. Garnero, A. Ducorps, S. Mazières, L. Lehéricy, S.T. du Montcel, B. Renault, and M. Vidailhet. Human brain mapping in dystonia reveals both endophenotypic traits and adaptive reorganization. *Annals of Neurology*, 50(4):521–527, 2001. [cited at p. 74, 103]

[72] J. C. Mosher, R. M. Leahy, and P. S. Lewis. EEG and MEG: forward solutions for inverse methods. *IEEE Transactions on Biomedical Engineering*, 46(3):245–259, Mar 1999. [cited at p. 19]

[73] J.C. Mosher and R.M. Leahy. Recursive music: a framework for EEG and MEG source localization. *IEEE Transaction on Biomedical Engineering*, 45(11):1342–54, 1998. [cited at p. 38]

[74] J.C. Mosher, R.M. Leahy, D.W. Shattuck, S. Baillet, et al. MEG source imaging using multipolar expansions. *Proc. 16th Conf. Information Processing in Medical Imaging*, pages 15–28. [cited at p. 26]

[75] J.C. Mosher, P.S. Lewis, and R.M. Leahy. Multiple dipole modeling and localization from spatio-temporal MEG data. *IEEE Transactions on Biomedical Engineering*, 39(6):541–557, 1992. [cited at p. 32, 35, 38]

[76] J.C. Mosher M.X. Huang and R.M. Leahy. A sensor-weighted overlapping-sphere head model and exhaustive head model comparison for meg. *Physics in Medicine and Biology*, 44:423–440, 1999. [cited at p. 19, 58]

[77] H.-H. Nagel. On the estimation of optical flow : relations between different approaches and some new results. *Artificial Intelligence*, 33:299–324, 1987. [cited at p. 85]

[78] G. Nolte and G. Curio. On the calculation of magnetic fields based on multipole modeling of focal biological sources. *Biophysical Journal*, 73:1253–1262, 1997. [cited at p. 51]

[79] G. Nolte and G. Curio. Current multipole expansion to estimate lateral extent of neural activity: A theoretical analysis. *IEEE Transactions on Biomedical Engineering*, 47(10):1347–1355, 2000. [cited at p. 33, 51, 58]

[80] P.L. Nunez and R. Srinivasan. *Electric fields of the brain: the neurophysics of EEG*. Oxford University Press, USA, 2006. [cited at p. 22]

[81] TF Oostendorp, A. Van Oosterom, and G. Huiskamp. Interpolation on a triangulated 3D surface. *Journal of Computational Physics*, 80(2):331–343, 1989. [cited at p. 121]

[82] B. Palit, A. Basu, and M.K. Mandal. Applications of the Discrete Hodge Helmholtz Decomposition to Image and Video Processing. *Lecture notes in computer science*, 3776:497, 2005. [cited at p. 80]

[83] J. Phillips and J.C. Leahy, R.M.and Mosher. Meg-based imaging of focal neuronal current sources. *IEEE Engineering in Medicine and Biology Magazine*, 16(3):338–348, 1997. [cited at p. 33, 47]

[84] J. Phillips, J.C. Leahy, R.M.and Mosher, and B. Timsari. Imaging neural activity using meg and eeg. *IEEE Engineering in Medicine and Biology Magazine*, 16(3):34–42, 1997. [cited at p. 47, 63, 64, 65, 67]

[85] M. Piccolino. Luigi Galvani and animal electricity: two centuries after the foundation of electrophysiology. *Trends in Neurosciences*, 20(10):443–448, 1997. [cited at p. 20]

[86] K. Polthier and E. Preuss. Identifying vector fields singularities using a discrete hodge decomposition. *Visualization and Mathematics*, 3:113–134, 2003. [cited at p. 80, 88]

[87] J. Régis, J.F. Mangin, T. Ochiai, V. Frouin, D. Riviére, A. Cachia, M. Tamura, and Y. Samson. Sulcal Root Generic Model: a Hypothesis to Overcome the Variability of the Human Cortex Folding Patterns. *Neurologia medico-chirurgica*, 45(1):1–17, 2005. [cited at p. 111, 112]

[88] J.A. Rossmanith, D.S. Bale, and R.J. LeVeque. A wave propagation algorithm for hyperbolic systems on curved manifolds. *Journal of Computational Physics*, 199:631–662, 2004. [cited at p. 84]

[89] J. Sarvas. Basic mathematical and electromagnetic concepts of the biomagnetic inverse problem. *Physics in Medicine and Biology*, 32:11–22, 1987. [cited at p. 29, 33]

[90] M. Scherg and D. von Cramon. Two bilateral sources of the late aep as identified by a spatio-temporal dipole model. *Electroencephalography and Clinical Neurophysiology*, 62:32–44, 1985. [cited at p. 34]

[91] G. Scheuermann and X. Tricoche. Topological Methods for Flow Visualization. *The Visualization Handbook*, pages 341–356, 2005. [cited at p. 80]

[92] C. Schnörr. Determining optical flow for irregular domains by minimizing quadratic functionals of a certain class. *International Journal of Computer Vision*, 6(1):25–38, 1991. [cited at p. 85, 87]

[93] D. Sharon, M.S. Hämäläinen, R.B.H. Tootell, E. Halgren, and J.W. Belliveau. The advantage of combining MEG and EEG: Comparison to fMRI in focally stimulated visual cortex. *Neuroimage*, 36(4):1225–1235, 2007. [cited at p. 19]

[94] S.M. Smith, M. Jenkinson, M.W. Woolrich, C.F. Beckmann, T.E.J. Behrens, H. Johansen-Berg, P.R. Bannister, M. De Luca, I. Drobnjak, D.E. Flitney, et al. Advances in functional and structural MR image analysis and implementation as FSL. *Neuroimage*, 23:208–219, 2004. [cited at p. 113, 121]

[95] J.X. Tao, A. Ray, S. Hawes-Ebersole, and J.S. Ebersole. Intracranial eeg substrates of scalp eeg interictal spikes. *Epilepsia*, 46(5):669–676, May 2005. [cited at p. 22]

[96] A. Tarantola. *Inverse Problem Theory and Methods for Model Parameter Estimation*. SIAM Books, Philadelphia, USA, 2004. [cited at p. 19]

[97] A.N. Tikhonov, V.Y. Arsenin, and F. John. *Solutions of ill-posed problems*. VH Winston Washington, DC, 1977. [cited at p. 42, 44, 45]

[98] Y. Tong, S. Lombeyda, A.N. Hirani, and M. Desbrun. Discrete multiscale vector field decomposition. *ACM Transactions on Graphics*, 22(3):445–452, 2003. [cited at p. 80]

[99] R. Toro and Y. Burnod. A morphogenetic model for the development of cortical convolutions. *Cerebral Cortex*, 15(12):1900–1913, 2005. [cited at p. 109]

[100] D.S. Tuch, V.J. Wedeen, A.M. Dale, J.S. George, and J.W. Belliveau. Conductivity mapping of biological tissue using diffusion MRI. *Annals of the New York Academy of Sciences*, 888:314–316, 1999. [cited at p. 31]

[101] K. Uutela, M. Hamalainen, and R. Salmelin. Global optimization in the localization of neuromagnetic sources. *IEEE Transactions on Biomedical Engineering*, 45(6):716–723, 1998. [cited at p. 35]

[102] D.C. Van Essen. A tension-based theory of morphogenesis and compact wiring in the central nervous system. *Nature*, pages 313–318, 1997. [cited at p. 109]

[103] B. D. van Veen and K. M. Buckley. Beamforming: a versatile approach to spatial filtering. *ASSP Magazine, IEEE [see also IEEE Signal Processing Magazine]*, 5:4–24, April 1988. [cited at p. 37]

[104] B.D. Van Veen, W. van Drongelen, M. Yuchtman, and A. Suzuki. Localization of brain electrical activity via linearly constrained minimum variance

spatial filtering. *IEEE Transactions on Biomedical Engineering*, 44(9):867–80, 1997. [cited at p. 39]

[105] F. Varela, J. P. Lachaux, E. Rodriguez, and J. Martinerie. The brainweb: Phase synchronization and large-scale integration. *Nature Reviews Neuroscience*, 2(4):229–239, April 2001. [cited at p. 22]

[106] Michael Wagner, Manfred Fuchs, and Jörn Kastner. Evaluation of sloreta in the presence of noise and multiple sources. *Brain Topography*, 16(4):277–280, 2004. [cited at p. 46]

[107] G. Wahba. *Spline models for observational data.* Society for Industrial Mathematics, 1990. [cited at p. 42]

[108] J.Z. Wang, SJ Williamson, and L. Kaufman. Magnetic source images determined by a lead-field analysis: The unique minimum-norm least-squares estimation. *IEEE Transactions on Biomedical Engineering*, 39(7):665–675, 1992. [cited at p. 45]

[109] J. Weickert and C. Schnörr. A theoretical framework for convex regularizers in pde-based computation of image motion. *International Journal of Computer Vision*, 45(3):245–264, December 2001. [cited at p. 85]

[110] J.P. Wikswo Jr and K.R. Swinney. A comparison of scalar multipole expansions. *Journal of Applied Physics*, 56:3039, 1984. [cited at p. 54]

[111] J.P. Wikswo Jr and K.R. Swinney. Scalar multipole expansions and their dipole equivalents. *Brain Mapping: The Methods*, 57:4301, 1985. [cited at p. 52, 54, 59, 63]

[112] C.C. Wood. Application of dipole localization methods to source identification of human evoked potentials. *Annals of the New York Academy of Sciences*, 388(1 Evoked Potentials):139–155, 1982. [cited at p. 34, 36]

[113] Y. Yukawa, N. Iriguchi, and S. Ueno. Impedance magnetic resonance imaging with external AC field addedto main static field. *IEEE Transactions on Magnetics*, 35(5 Part 2):4121–4123, 1999. [cited at p. 31]

[114] J.E. Zimmerman. SQUID instruments and shielding for low-level magnetic measurements. *Journal of Applied Physics*, 48:702, 1977. [cited at p. 16]

[115] J.M. Zumer, H.T. Attias, K. Sekihara, and S.S. Nagarajan. A probabilistic algorithm integrating source localization and noise suppression for MEG and EEG data. *NeuroImage*, 37:102–115, 2007. [cited at p. 40]

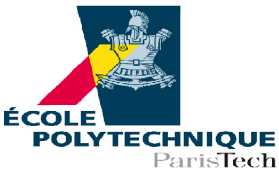

THÈSE

Présentée pour obtenir

LE GRADE DE DOCTEUR EN SCIENCES

DE L'ÉCOLE POLYTECHNIQUE

Spécialité : Mathématiques Appliquées

par

Khan SHERAZ

MEG Source Imaging and Dynamic Characterization

ÉCOLE POLYTECHNIQUE-CENTRE DE MATHÉMATIQUES APPLIQUÉES